Title
Advances in Computational Methods for Water-Wave Problems

Author
Hariri Nokob, Mohamed

Publication Date
2017

Peer reviewed|Thesis/dissertation

Advances in Computational Methods for Water-Wave Problems

by

Mohamed Hariri Nokob

A dissertation submitted in partial satisfaction of the

requirements for the degree of

Doctor of Philosophy

in

Engineering - Mechanical Engineering

in the

Graduate Division

of the

University of California, Berkeley

Committee in charge:

Professor Ronald W. Yeung, Chair
Professor M. Reza Alam
Professor Shawn Shadden
Professor John A. Strain

Fall 2017

Advances in Computational Methods for Water-Wave Problems

Abstract

Advances in Computational Methods for Water-Wave Problems

by

Mohamed Hariri Nokob

Doctor of Philosophy in Engineering - Mechanical Engineering

University of California, Berkeley

Professor Ronald W. Yeung, Chair

We developed three different techniques to enhance the computational methods used for time-harmonic linear water-wave theory. The first makes use of hypersingular boundary integral equations to model thin solid bodies in a wave field. The method developed allows for numerical treatment of the problem in its original hypersingular form using higher-order Overhauser elements without the need for regularization. We then use the method to study the case of a thin bottom-touching barrier in waves with particular interest in the effect of the harbor mouth (opening) over its hydrodynamic characteristics. Our results shed light on the drastic changes that occur in the presence of the opening and its size. We also point to the discovery of particular opening widths that allow for zero total loads on the harbor at particular frequencies.

The second part still deals with hypersingular boundary integral equations but in the context of thin arbitrarily shaped plates. A Galerkin approach is used to treat the high-order singularity and results are used to fill some gaps in the literature of the values of added mass for these plates, particularly those plates with openings or holes.

The third numerical method we present allows for the efficient treatment of general linear water-wave problems with multiple arbitrarily shaped bodies and arbitrarily shaped seabed geometry when the number of unknowns in the problem N is large. The problem domain is divided into an internal region that is modeled using a simple-source boundary integral equation allowing for arbitrarily shaped body and bottom geometry and an outer domain that is assumed free of solid bodies and of uniform water depth. The two domain solutions are then matched to complete the solution. The major contribution in this present topic is introducing the "fast-multipole method" to the solution procedure and therefore changing the complexity of the problem from $O(N^3)$ (or $O(N^2)$ if an iterative solver is used) to $O(N)$ for large values of N. The memory requirements scale linearly with N as well. This methodology is needed when the number of solid bodies is large or when very large floating structures with complex shapes are needed. It is also necessary when the bottom topography for a particular problem varies considerably. We use the computational code developed to study the effects of variable bottom topography over two case examples of multiple floating bodies. The first

case is a set of 4 truncated floating vertical cylinders over a bottom protrusion, for which results indicate that variations in bottom topography cause slight to medium level changes on the wave loads on the floating bodies. The second case is applied to a configuration of 16 floating cylinders (with $N \sim 150,000$) and the effects of the variable ocean floor are again considered. Wave elevation details of this complex geometry is shown for illustration.

To my Mom and Dad. I love you.

Contents

List of Figures

Acknowledgments

I would like to acknowledge the support of the Ocean Technology Fellowship, funded by the American Bureau of Shipping, as well as the John G. Maurer Scholarship Fund of the Graduate Division at UC Berkeley.

I have many people to thank for all the great things that happened to me in life starting with my family, friends, mentors and thesis committee members. I would like to particularly show my sincere appreciation to my advisor Professor Ronald W. Yeung for giving me a chance to come to Berkeley, learn from him, experience education at one of the best institutions in the world and simply have hope for a better future. I may be hard headed at times and cause some trouble now and then, but deep down I feel privileged to be one of your last students.

Chapter 1

Introduction

The analysis of interaction of water waves with floating or fixed bodies is very important in practice. All modern design of maritime structures is driven by the ever more sophisticated analysis of how those structures will act in the oceanic environment and especially what kind of loads are to be expected as the waves act on those structures. It has therefore became more imperative over the years to have better tools to analyze those interactions. The availability of computers played an important role to shift attention towards numerical methods and triggered enthusiasm among the practitioners to test how reliable those new tools at hand can be. In addition, the introduction of new types of ocean structures such as farms of wave energy converters or very large floating structures brought forward some new challenges and required new methods of analysis for which previous experience was insufficient. To that end, the development of numerical and computational methods used in the maritime industry is not only desirable but also a necessity to meet those new challenges. We hope, through this work, to be able to serve the maritime community in advancing the understanding and practice of the design of ocean structures.

In what follows, consider a three dimensional coordinate system xyz with the z-axis pointing upwards (to the free surface for example).

1.1 Water Wave Theory

Water waves are in general nonlinear, slightly viscous and turbulent. These characterizations are particularly important for overturning and breaking waves. They differ from other fluid flows by the presence of a free surface. They represent a special case of two phase flows in which one phase (the air) causes negligible stresses and its pressure is assumed constant in space. The time varying position of the free surface is still part of the solution though. Accordingly, the general motion of ocean waves without turbulence is governed by the Navier-Stokes equations for a homogeneous fluid in addition to no-slip conditions on solid boundaries S_B, and kinematic and stress free conditions on the free surface S_F (see [1] or [2] for a detailed introduction):

$$\frac{\partial \overrightarrow{u}}{\partial t} + \overrightarrow{u}.\nabla \overrightarrow{u} = -\frac{\nabla p}{\rho} + \overrightarrow{g} + \nu \nabla^2 \overrightarrow{u}, \tag{1.1}$$

$$\nabla . \overrightarrow{u} = 0, \tag{1.2}$$

$$-pI + \mu[\nabla \overrightarrow{u} + (\nabla \overrightarrow{u})^T] = -p_{atm} I, \text{ (on } S_F) \tag{1.3}$$

$$\frac{\partial \eta}{\partial t} = \overrightarrow{u}.\nabla(z - \eta), \text{ (on } S_F) \tag{1.4}$$

$$\overrightarrow{u} = \overrightarrow{u_B}, \text{ (on } S_B). \tag{1.5}$$

Here surface tension is ignored as it is not usually important for marine applications. We made use of the definitions $\overrightarrow{u}$ for the fluid velocity vector, t for time, p and p_{atm} for pressure and atmospheric pressure respectively, ρ for density, ν and μ for the kinematic and dynamic viscosity respectively, $\eta(x, y)$ is the free surface height, $\overrightarrow{u_B}$ is any solid body velocity, $\overrightarrow{g} = [0, 0, g]$ is the gravitational acceleration vector and I is the identity matrix. In general, these equations need to be solved for the velocities, fluid pressure and free surface elevation for a complete solution of the water wave flow. This is difficult in practice if the exact equations are to be solved although significant progress has been achieved [3]. The methods used differ mainly in how they track the free surface including the use of fixed [4] and moving [5] grid methods. The additional assumption of an irrotational fluid (justified by Kelvin's circulation theorem [6] which states that an ideal fluid initially irrotational will remain as so in the presence of conservative body forces), leads to a more simplified potential flow model, yet still nonlinear. Very good numerical methods have been developed to solve for this type of model [7].

1.1.1 Linear Water Waves

When the wave amplitude is sufficiently small compared to the wavelength and water depth, the equations that govern the motion of the fluid can be linearized without much loss of accuracy. If we define the velocity potential Φ such that $\overrightarrow{u} = \nabla\Phi$, the governing equations can be reduced to the more practical linear potential flow model:

$$\nabla^2 \Phi = 0, \tag{1.6}$$

$$\frac{\partial \Phi}{\partial t} + g\eta = 0, \text{ (on } S_F) \tag{1.7}$$

$$\frac{\partial \eta}{\partial t} - \frac{\partial \Phi}{\partial z} = 0, \text{ (on } S_F) \tag{1.8}$$

$$\frac{\partial \Phi}{\partial n} = \overrightarrow{u_B}.\overrightarrow{n}, \text{ (on } S_B). \tag{1.9}$$

Now for most practical situations, it is usually sufficient to consider time harmonic waves. This shifts the solution to the simpler frequency domain, drops the time dependency, and can

consequently be used to simulate more complicated scenarios in the time domain. Accordingly, let $\Phi = \phi(x, y, z)e^{-i\omega t}$ and $\overrightarrow{u} = \overrightarrow{U}e^{-i\omega t}$ for some angular frequency ω. This further reduces the problem at hand to:

$$\nabla^2\phi_j = 0, \tag{1.10}$$

$$-\omega^2\phi_j + g\frac{\partial\phi_j}{\partial z} = 0, \text{ (on } S_F) \tag{1.11}$$

$$\eta_j = -\frac{\omega\phi_j}{g}, \ (onS_F) \tag{1.12}$$

$$\frac{\partial\phi_j}{\partial n} = \overrightarrow{U_j}.\overrightarrow{n}, \text{ (on } S_B). \tag{1.13}$$

$$\sqrt{r}\left(\frac{\partial}{r} - i\kappa_0\right)\phi_j = 0. \text{ (on } S_R) \tag{1.14}$$

The last condition 1.14 is needed to insure a unique solution for the time harmonic problem dictating outgoing waves and is taken over the surface S_R defined by $r \to \infty$. $\kappa_0 = 2\pi/\lambda$ is the wavenumber associated with wavelength λ. The subscript j is used to refer to the mode of motion with $j = 1, 2, 3, 4, 5, 6$ referring to surge, sway, heave, roll, pitch and yaw modes, respectively. This decomposition of the general problem to these sub-problems is possible because of linearity.

In the case where solid bodies are static and an incident wave approaches the bodies, it is then more convenient to solve for the potential correction term ϕ_7 defined as $\phi = \phi_0 + \phi_7$ where ϕ is the total potential and ϕ_0 is the incident wave potential. The previous set of equations (1.10-1.14) then apply directly to ϕ_7 with the exception of 1.13 which is modified to:

$$\frac{\partial\phi_7}{\partial n} = -\frac{\partial\phi_0}{\partial n}, \text{ (on } S_B). \tag{1.15}$$

For the case when the water depth h is constant (at least far away from any bodies in the water), the incident wave potential ϕ_0 is given in [8]:

$$\phi_0 = -\frac{\eta_0\omega}{\kappa_0}\frac{\cosh(\kappa_0(z+h))}{\cosh(\kappa_0 h)}e^{i\kappa_0 r\cos(\theta-\alpha)}, \tag{1.16}$$

for some given wave direction α (relative to the x-axis) and wave amplitude η_0.

1.2 The Boundary Integral Equation Solution

Traditionally, the boundary integral formulation has been the favored solution approach to the linear water-wave problem. The fact that the velocity potential in any part of the domain could be represented exactly by values defined over the boundary surface is very appealing in practice as the problem dimension is reduced by one and the number of required solution unknowns is significantly reduced. The boundary element method is the term used for the

numerical procedure used to approximate the solution. Only the boundary is discretized into some form of triangulation and the problem unknowns (usually the potential or its derivatives) are then fitted into some chosen general shape functions. The parameters of the shape functions become the only unknowns of the problem to solve for. The convergence accuracy of the solution then depends on the order of the shape functions and triangulation used with higher order functions providing higher accuracy and added implementation complexity. Finally, either a collocation or Galerkin type schemes are used to form a full system of equations and solve for the unknowns. Since the kernel functions for boundary integral methods are singular and usually difficult to integrate, the collocation scheme is usually preferred in practice as it requires far less computational effort to form the system of equations. This is unlike the more popular finite element methods where Galerkin methods dominate because of their ease of integration and the resulting symmetric systems of equations obtained (see [9] for a review and comparison).

For potential flow problems governed by equations (1.10-1.14), the boundary integral formulation is obtained from Green's second identity:

$$4\pi\phi_j(P) = \int_S \left(\phi_j(Q)\frac{\partial G(P,Q)}{\partial n_Q} - G(P,Q)\frac{\partial \phi_j(Q)}{n_Q}\right) dS_Q. \tag{1.17}$$

Integration is taken over $S = S_B \cap S_F \cap S_R$ the full boundary of the fluid. Here G is the chosen appropriate Green function for the problem and is singular in general. The classical reference for free-surface Green functions is [1].

By the least, G must satisfy the governing equation (1.10) except when P coincides with Q. This equation provides a means to obtain the potential at some point P in the fluid domain from a knowledge of the potential and its derivative at all the boundary points Q. To solve for the potential over the surface, point P is made to approach Q very carefully so that when they coincide, a new equation is obtained:

$$2\pi\phi_j(P) = \int_S \left(\phi_j(Q)\frac{\partial G(P,Q)}{\partial n_Q} - G(P,Q)\frac{\partial \phi_j(Q)}{n_Q}\right) dS_Q. \tag{1.18}$$

This equation is solved for the surface potential which is then used in (1.17).

The most commonly used Green function for the linear water-wave problem is the wave Green function that automatically satisfies the free surface and radiation conditions and, therefore, no integration over the respective boundaries is necessary. In addition, the ocean bottom boundary condition is also satisfied when the water depth is finite constant or infinite. For example, for the case of an ocean floor with constant finite water depth h, the Green function is given by:

$$\begin{aligned} G(P,Q) &= \frac{1}{\sqrt{R^2+(z-\zeta)^2}} + \frac{1}{\sqrt{R^2+(2h+z+\zeta)^2}} \\ &+ 2\int_0^\infty \frac{(k+\kappa_0)\cosh(k(z+h))\cosh(k(\zeta+h))}{k\sinh(kh)-\kappa_0\cosh(kh)} e^{-kh} J_0(kR)dk. \end{aligned} \tag{1.19}$$

This function satisfies the free-surface condition, the finite water depth condition as well as the radiation condition exactly. It follows that the integration in equation (1.17) need to be carried over floating bodies in the problem only as the rest of the integrals over the bottom, free-surface or radiation boundary drop out. Here R is the distance between P and Q in the horizontal plane, and z and ζ are the corresponding vertical coordinates. J_0 is the zeroth-order Bessel function. The direct integration in (1.19) is costly in practice and alternative methods are more suitable. An approximate procedure to find G was given by Newman [10] using interpolation for parts of the space when P is close to Q and using John's equivalent series [11] otherwise.

1.2.1 On Hypersingular Boundary-Integral Equations

Of particular relevance to this work are hypersingular boundary-integral equations which are integral equations that admit hypersingular kernels. These usually appear when one attempts to take the derivative under the integral of a singular kernel typically encountered in the water-wave problem. A one-dimensional two-sided singular integral is of the form:

$$\int_a^b \frac{f(t)}{(t-t_0)^n} dt, \ (t_0 \in]a,b[). \tag{1.20}$$

The integral is considered singular if $n \geq 1$ and hypersingular when $n > 1$. In these cases, a *regularization* of some sort is necessary for the integral to exist. For example, when $n = 1$, the integral is interpreted in the sense of the Cauchy Principle Value, and when $n = 2$, the finite part of the integral is kept (Hadamard Regularization) as follows:

$$\int_a^b \frac{f(t)}{(t-t_0)^2} dt = \lim_{\epsilon \to 0} \left(\int_a^{t_0-\epsilon} \frac{f(t)}{(t-t_0)^2} dt + \int_{t_0+\epsilon}^b \frac{f(t)}{(t-t_0)^2} dt - \frac{2f(t_0)}{\epsilon} \right), \tag{1.21}$$

where the last term represents the unbounded part and is subtracted to obtain the finite part. Note that $f(t) \in C^{0,\alpha}$ and $f(t) \in C^{1,\alpha}$ for $n = 1$ and $n = 2$ respectively, where $C^{m,\alpha}$ referes to the class of Holder continuous functions smooth to the order m and $0 < \alpha \leq 1$ [12]. Regularization is also necessary when $t_0 = a$ or $t_0 = b$. The integral is then interpreted as a one-sided finite part integral regularized as follows:

$$\int_a^{t_0} \frac{f(t)}{t-t_0} dt = \lim_{\epsilon \to 0} \left(\int_a^{t_0-\epsilon} \frac{f(t)}{t-t_0} dt + f(t_0) \ln \epsilon \right), \tag{1.22}$$

$$\int_{t_0}^b \frac{f(t)}{t-t_0} dt = \lim_{\epsilon \to 0} \left(\int_{t_0+\epsilon}^b \frac{f(t)}{t-t_0} dt - f(t_0) \ln \epsilon \right), \tag{1.23}$$

$$\int_a^{t_0} \frac{f(t)}{(t-t_0)^2} dt = \lim_{\epsilon \to 0} \left(\int_a^{t_0-\epsilon} \frac{f(t)}{(t-t_0)^2} dt - \frac{f(t_0)}{\epsilon} \right), \tag{1.24}$$

$$\int_{t_0}^b \frac{f(t)}{(t-t_0)^2} dt = \lim_{\epsilon \to 0} \left(\int_{t_0+\epsilon}^b \frac{f(t)}{(t-t_0)^2} dt - \frac{f(t_0)}{\epsilon} \right). \tag{1.25}$$

Notice that the two-sided integrals can be obtained by adding the corresponding one-sided ones after regularization. This will be an important observation later on when these integrals are carried over individual panels and the result summed up over all panels. It is also essential to note that the integrals (1.22) and (1.23) do not allow for a simple change of variable because of the logarithmic terms used for regularization [13].

Now when the volume of a solid body shrinks so that the body is merely an infinitely thin sheet, the surface integral in equation (1.17) is carried over the opposite sides of the body (S^+ and S^-). These are essentially the same with opposite normal vectors ($n^+ = -n^-$). It follows from equation (1.13) that the second term on the right side of (1.17) drops out. The potential in the other term is replaced by $[\phi_j] \equiv \phi_j^+ - \phi_j^-$ and integration is carried over one side only. The resulting equation (when a free-surface Green function is used) is:

$$4\pi\phi_j(P) = \int_{S^+} \left([\phi_j(Q)] \frac{\partial G(P,Q)}{\partial n_Q} \right) dS_Q. \tag{1.26}$$

Finally, taking the normal derivative and carrying it under the integral sign (this is justified from the work in [13]) results in:

$$4\pi \frac{\partial \phi_j(P)}{\partial n_P} = \int_{S^+} \left([\phi_j(Q)] \frac{\partial^2 G(P,Q)}{\partial n_P \partial n_Q} \right) dS_Q. \tag{1.27}$$

The boundary condition (1.13) is then used on the left side of the equation and the potential jump $[\phi_j]$ is considered the unknown to be solved for. The second derivative in this equation, however, results in a hypersingular kernel for the surface integral.

1.3 On The Fast Multipole Method

A second aspect of this thesis is that we will make use of the Fast Multipole Method (FMM) in order to reduce the computational complexity of the numerical solution for the linear free-surface wave problem to $O(N)$ where N is the number of unknowns to solve for. The method was originally developed to speed up the interactions in the n-body problem (see [14] and [15]). It was later widely accepted as a means to accelerate the matrix vector multiplications required by the iterative solvers for the boundary element method (see [16] for a review) used in the various scientific disciplines. Particular examples relevent to the marine field include [17] for the discrete element method, [18] for ship flows, [19] for ship hulls and [20] for airfoils.

The basic idea behind the FMM and other similar methods is that the interaction effect of far away particles could be grouped together and applied collectively on individual target particles. A hierarchical scheme such as an Octree is used to group close particles together in cells. Interactions between the particles are then replaced by interactions between cells. For the FMM for example, each cell is assigned an interaction list of cells for which the interaction effects are approximated by multipole expansions. Interactions between adjacent

cells, however, are still treated in a regular direct manner. In addition, cells that are determined to be far from a particular target (not in the interaction or adjacent list of cells) need not be accounted for directly as their effects will be carried over from the parent cell of the target cell. This set of rules is what makes the FMM unique and truly $O(N)$ in complexity compared to other methods. We will discuss this in more detail in chapter 3.

The FMM can be applied to a variety of problems that can be solved using the boundary element method. It is relevant to our work as it applies to the numerical solution of (1.18). The choice of Green's function matters in this case to the application of the FMM as it is important to pertain the necessary multipole expansion for a particular Green function. A function such as that in (1.19) has more complicated multipoles than the simple Rankine source and is more computationally expensive to evaluate (see [9]). However, as we discussed earlier, the Rankine source by itself is not sufficient to deal with the complicated boundary conditions in (1.11) and (1.14). That is why we turned to hybrid matching numerical methods to solve this problem. The idea is that the fluid domain is divided into a simple external domain for which the solution is modeled in a general manner (eigenfunction expansions are used here), and an internal domain for which the solution is modeled using a simple source boundary integral equation. Since the only Green function used in this case is the Rankine source, a simpler version of the FMM can be applied leading to a more efficient algorithm.

1.4 Dissertation Outline

This dissertation consists of three main parts. The first, presented in chapter 2, will go into the details of the treatment of the hypersingular representation of the solution to the linear water-wave problem with thin bodies at high orders of approximation. Particular emphasis is then placed over the effect of harbor openings on the hydrodynamic loads over the harbor.

The second part, presented in chapter 3, will extend the treatment of hypersingular integral equation to three dimensional space dealing with flat plates of arbitrary shapes. The methods used here will be very different than the first part.

The third part of the dissertation (chapter 4) will introduce the Fast Multipole treatment of the numerical procedure to the general linear water-wave problem with floating bodies. The efficiency of the proposed method will be quantified and then the method is used to simulate the complex effects of variable bottom topography over a group of floating bodies.

Finally, we will end with a conclusion that will summarize the work presented here as well as discuss possible extensions in the future. Note that each chapter is independent from the rest and is self contained for the most part.

Chapter 2

Diffraction and Radiation Loads on Open Cylinders of Thin and Arbitrary Shapes

The contents of this chapter have been published by the author and are mostly taken from [21] with some additional content from [22]. In order to conform with the conventions used in those references, the coordinate system will be taken such that the y-axis is pointing upwards perpendicular to the free surface.

2.1 Introduction

In his 1970 paper, Garrett [23] presented a solution to the diffraction problem of a bottomless harbor that is circumferentially closed. He argued that any realistic model of a real floating harbor must include the effects of the harbor shape, thickness and opening (harbor mouth), but the shape would not cause any qualitative differences and the thickness had negligible effects. He construed that"The effect of the harbour entrance is less obvious". In this work, we will attempt to shed some light on exactly this last point. We will tackle the problem numerically using a boundary integral approach and try to understand of the results obtained.

The proposal to build a floating harbor or intermediate transport station close to the Brazilian coast [24] as well as the emerging Portunus project, which proposes to construct floating harbors off the US coasts [25], require an understanding of the consequences of having an open-shaped body in the ocean because the harbor will inevitably need to be an open body. Furthermore, the desire to design more cost effective ocean structures motivates engineers to examine unconventional designs of these structures. One instant suggestion is to use open columns to support platforms and other facilities. This requires a thorough understanding of the changes that occur when these columns are opened. Typically, these problems are three dimensional and computationally expensive. The computational effort is significantly reduced by assuming that the bodies have zero thickness.

Hence, the study of a wave field interacting with such thin structures is worthwhile as these often appear in designs. Stiffeners, plates and shells are important examples used in marine design. The numerical treatment of these components by standard means, such as the boundary-integral method, is expected to be troublesome. The usual situation is that the numerical problem becomes ill-conditioned as the thickness of the body decreases. This is because two opposite points of the body surface tend to carry the same information in the limit of vanishing thickness. It is more natural then to consider the potential jump across the body surface instead. This reduces the number of problem unknowns to at least a half, which is a significant reduction for three-dimensional problems.

It follows from the boundary-integral formulation that the potential field over a zero-thickness shell is represented by a double-layer sheet. The application of boundary conditions then leads to a hypersingular integral that needs to be computed carefully [26, 12]. Such a treatment is also a good approximation to bodies of the same shape having a finite but small thickness [27]. This method was originally used in solid mechanics for crack problems in [13] and was later used for water-wave problems to model the scattering [12, 28] and radiation [29, 30] of water waves from flat or curved plates, and disks. These last references used a novel method to deal with the hypersingularity. The potential jump over the body surface was represented in terms of Chebychev basis functions with the proper weights so that the hypersingular integral could be evaluated analytically over flat surfaces. The same method could be used for different geometries if the integrand is written as the sum of singular and regular terms. The integral of the singular part is then treated analytically and the correction terms are integrated numerically. This is the case in [31] in which a surging flap wave energy converter, modeled as a thin vertical plate was considered. This procedure also has the advantage of considering the square-root singular behavior near the body edges explicitly. The problem is that the series expansion of the integrand has to be valid over all the body surface, which may require several terms in the series expansion especially as the body shape becomes more complicated. Integration over the whole surface is also required to compute each influence coefficient of the linear system. Given that calculating these coefficients requires the bulk of the computational effort, it is more desirable to find a more effective method. The procedure we present here depends on a set of compact basis functions and does not require any series expansion over the entire body surface. The method is found to be very stable and well conditioned. Note that the hypersingular integral can be avoided altogether by regularization [26]. This involves the use of Stoke's theorem to reduce the order of the singularity but usually requires some additional work for the evaluation of tangential derivatives of the unknown potential, which presents another numerical challenge that cannot be easily handled in practice.

In this chapter, we treat the singularity directly by Taylor expanding the integrand about the singular point. This is the approach for the case of a truncated circular cylinder in [32]. In this work, the original field equation is transformed into a set of Helmholtz equations in two dimensions after the potential is expanded in terms of the natural vertical modes. This procedure was used in [31] to model a flap-type wave energy converter. This decomposition, which only applies for bottom-mounted cylinders, is very convenient from a computational standpoint as the numerical procedure is simplified and the simulation time is significantly reduced.

Our solution method is applied to model incident-wave flow over vertical cylinders of any cross-sectional shapes. This conveniently allows us to model open shells and study the wave loads on these bodies subject to time-harmonic incident waves or arising because of the motion of the bodies themselves in surge, sway, roll, pitch and yaw directions. We assume that these motions are theoretically possible although the cylinders extend to the ocean floor. That means that proper supports are used at the bottom or the results here are approximations to finite draft bodies whose height is comparable to the water depth. This is a good

approximation in general, especially in deeper water where most activity is confined near the free surface. The authors' previous works on this subject include [22], [33] and [21]. In this last paper, a higher-order method based on the modified Overhauser elements is used to solve the hypersingular problem. The results for an open shell are then analyzed in some detail and presented here as well.

We also note that that the hypersingular integral equation formulation is used to avoid non-uniqueness problems (irregular frequencies) associated with floating solid bodies [34, 35]. The combination of the hypersingular integral equation with the less singular equation is well posed for all frequencies. The open thin shells considered here do not suffer from those problems because no internal potential (inside the thin bodies) exists but the procedure presented here is useful in those situations as well.

The following sections start by presenting the problem formulation and method of solution. Then, radiation and diffraction results for open circular, elliptical and square shaped shells are presented and discussed. The free-surface elevations for some particular geometries are also presented.

2.2 Computational Theory

2.2.1 Problem Formulation

We assume linear water wave potential theory. All potentials Φ are considered harmonic in time with frequency ω such that $\Phi(x,y,z,t) = Re\{\phi(x,y,z)e^{-i\omega t}\}$. These potentials are normalized as $\phi^R = \overline{\phi}^R/a^l U$ and $\phi^S = \overline{\phi}^S/\eta_0\sqrt{ga}$ for any of the radiation and scattering potentials respectively. The terms with an overbar are always dimensional, a is a characteristic length of the body, g is the acceleration of gravity, and η_0 is the incident wave amplitude. The constant U is the amplitude of the translation and rotation forced motions and the integer l is 1 for surge and sway and is 2 for roll, pitch and yaw. These motions will be denoted by the integers $p = 1, 2, 4, 5, 6$ respectively and we use $p = 0, 7$ for the incident and diffracted potentials. The corresponding potential for these different motions is denoted by ϕ^p. In addition, the water depth is finite and given by h.

Let the coordinate system be fixed on the calm free surface with the y axis pointing upwards (see figure 2.1). We use the characteristic length a to nondimensionalize all length parameters and wavenumbers in this work. The problem is then the classical water wave formulation given by:

$$\nabla^2\phi^p = 0, \tag{2.1}$$

$$\frac{\partial\phi^p}{\partial y} - \nu\phi^p = 0, y = 0, \nu = \frac{\omega^2 a}{g}, \tag{2.2}$$

$$\frac{\partial\phi^p}{\partial y} = 0, y = -h. \tag{2.3}$$

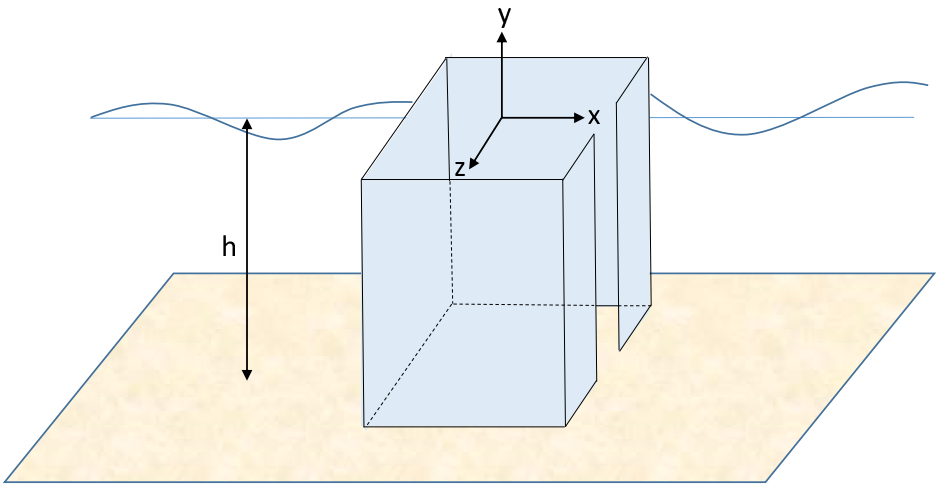

Figure 2.1: Schematic diagram of a square shaped open shell

Let $\overrightarrow{n} = [n_1, 0, n_2]$ be the normal vector pointing out of the body, then the kinematic condition on the body surface applies as:

$$\frac{\partial \phi^p}{\partial n} = \begin{cases} n_p, (p = 1, 2), \\ (y + h)n_{p-3}, (p = 4, 5), \\ zn_1 - xn_2, (p = 6), \\ -\frac{\partial \phi^0}{\partial n}, (p = 7). \end{cases} \tag{2.4}$$

We assumed that the rolling and pitching axes pass through the origin projection on the ocean floor. A radiation condition that dictates outgoing waves is also required. Now we can introduce the decomposition:

$$\phi^p(x, y, z) = \sum_{n=0}^{\infty} \varphi_n^p(x, z) Y_n(y), \tag{2.5}$$

$$Y_n(y) = \frac{\cosh(\kappa_n(y + h))}{M_n}, \qquad M_n = \sqrt{\frac{\sinh(2\kappa_n h)}{4\kappa_n} + \frac{h}{2}} \tag{2.6}$$

where the $M_n's$ are scale factors to make the $Y_n's$ an orthonormal set. The functions φ_n^p are unknown modal potentials in the horizontal plane and κ_n are real ($n = 0$) and imaginary ($n > 0$) wavenumbers that satisfy the usual dispersion relation $\kappa_n \tanh(\kappa_n h) = \nu$. The functions $Y_n(y)$ satisfy the conditions (2.2) and (2.3) effectively removing any depth dependence. The incident potential is given and can be decomposed in the same manner:

$$\begin{aligned} \phi^0(x, y, z) &= \varphi_0^0(x, z) Y_0(y), \\ \varphi_0^0 &= \frac{e^{i\kappa_0(x\cos\beta + z\sin\beta)}}{i\sqrt{\nu} Y_0(0)}, \end{aligned} \tag{2.7}$$

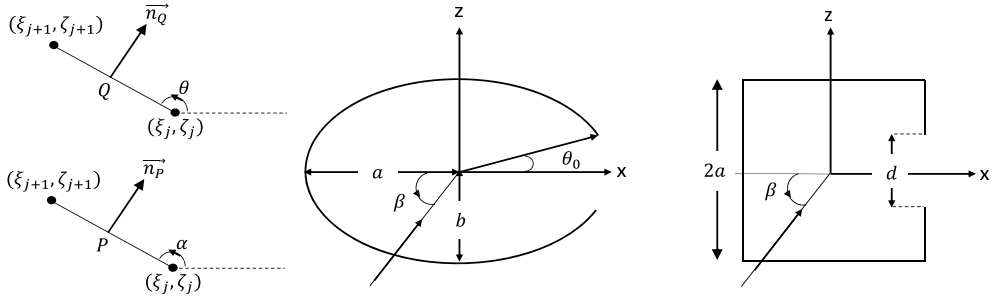

Figure 2.2: Schematic of one panel showing points Q and P and the cross sectional shapes of elliptical- and square-shaped bodies. The incident wave direction, of angle β, is also shown.

where β is the incident wave direction (figure 2.2). The problem thus reduces to:

$$(\nabla^2 + \kappa_n^2)\varphi_n^p = 0, \tag{2.8}$$

$$\frac{\partial \varphi_n^p}{\partial n} = \begin{cases} n_p \frac{\sinh(\kappa_n h)}{\kappa_n M_n}, (p = 1, 2), \\ \frac{n_{p-3}}{\kappa_n^2 M_n}(\kappa_n h \sinh(\kappa_n h) - \cosh(\kappa_n h) + 1), (p = 4, 5), \\ (zn_1 - xn_2)\frac{\sinh(\kappa_n h)}{\kappa_n M_n}, (p = 6), \\ -\frac{\partial \varphi_0^0}{\partial n}\delta_{0n}, (p = 7). \end{cases} \tag{2.9}$$

The equations in (2.9) were derived from (2.4) using the fact that Y_n are orthogonal over the water depth. Equations (2.8, 2.9) will be solved as an integral equation using the boundary element method. The potential φ_n^p is thus represented by a normal dipole sheet and then (2.9) is applied [12]:

$$\frac{\partial \varphi_n^p}{\partial n_P} = \int_C [\varphi_n^p] \frac{\partial^2 G_n}{\partial n_P \partial n_Q}\, ds, \tag{2.10}$$

where $[\varphi_n^p]$ is the potential jump across the body and $P(x, z)$ and $Q(\xi, \zeta)$ are collocation and integration points respectively (e.g. see [9]). C is one side of the body surface and G_n is the fundamental solution of the corresponding Helmholtz equation and is given by [34]:

$$G_n = -\frac{i}{4} H_0(\kappa_n R), \tag{2.11}$$

$$R = |PQ| = \sqrt{(x - \xi)^2 + (z - \zeta)^2}.$$

Here H_0 is the Hankel function of the first kind and order zero. In general, an additional term needs to be added to the left hand side of (2.10) to account for the fact that the kernel is hypersingular (see [36]). However, the additional term is not needed in this case because we will use straight panels with zero curvature to discretize the boundary. More care should be taken for higher order elements.

Using the fact that $\overrightarrow{n_P} = [\sin(\alpha), -\cos(\alpha)]$ and $\overrightarrow{n_Q} = [\sin(\theta), -\cos(\theta)]$, where α and θ are

the slope angles of the body curve in the horizontal plane (defined in figure 2.2), we have:

$$\begin{aligned}\frac{\partial^2 G_n}{\partial n_P \partial n_Q} = &\frac{i\kappa_n}{4R^2}\left(\frac{2H_1(\kappa_n R)}{R} - \kappa_n H_0(\kappa_n R)\right)\\ &\times \big((\xi - x)^2 \sin(\alpha)\sin(\theta) + (\zeta - z)^2 \cos(\alpha)\cos(\theta)\\ &- (\xi - x)(\zeta - z)\sin(\theta + \alpha)\big)\\ &- \frac{i\kappa_n}{4R} H_1(\kappa_n R)\cos(\theta - \alpha). \end{aligned} \tag{2.12}$$

2.2.2 Numerical Integration and Solution Procedure

The body contour is divided into N flat panels $C_j[(\xi_j, \zeta_j), (\xi_{j+1}, \zeta_{j+1})]$ as in (figure 2.2). Collocation inside the panels is easy and does not require higher order interpolating basis functions but that leads to nonconforming elements, which results in a lower accuracy of the formulation as well as a dependency on the position of the collocation points (see [37] for more information). It is more natural then, and desirable to collocate at the edges of the panels. This ensures that the boundary conditions are met at the exact positions of the original problem. Because the kernel of the integral in (2.10) is hypersingular, this requires a density distribution that at least belongs to $C^{1,\alpha}$, the space of functions with Holder continuous first derivatives [13]. However, this requirement can be loosened as indicated in [38]. In fact, we will use the concepts in this last reference as explained in appendix A. Nonetheless, to obtain a high order method, we choose to use the modified cubic Overhauser polynomial elements to represent the potential jump distribution. These elements have a continuous derivative at the edges of the panels and the interesting property of being locally independent of each other. That is, any local errors will not propagate across the mesh as in the case of other functions. They also do not require evaluating derivatives at the edges as continuity of the derivatives is guaranteed by the structure of the elements themselves. This makes them simple to use. Furthermore, several authors have shown the superiority of these elements in certain aspects such as stability. A short review on these elements can be found in [39] and [40]. The authors in this last reference note that the Overhauser elements suffer from errors when the mesh size is nonuniform. They develop a set of modified Overhauser elements that take the varying mesh into account and show their applicability to boundary element methods. We choose to adopt those last elements in this work.

We introduce a parameter t that varies between 0 and 1 over some panel j. Let $[\varphi]_j$ be the value of the density at the starting edge of the panel j. If j wasn't at some end of the shell then the density $[\varphi]$ over that panel is interpolated as:

$$[\varphi] = \sum_{q=j-1}^{j+2} N_q(t)[\varphi]_q, \tag{2.13}$$

$$N_q(t) = \sum_{k=1}^{4} b_{qk} t^{k-1}. \tag{2.14}$$

Here, $N_q(t)$ are the Overhauser elements. These coefficients vary for each panel and are given by:

$$b_{qk} = \begin{bmatrix} 0 & -\frac{(1-w_1)^2}{w_1} & \frac{2(1-w_1)^2}{w_1} & -\frac{(1-w_1)^2}{w_1} \\ 1 & \frac{1-2w_1}{w_1} & \frac{w_1(2-w_2)-2}{w_1} & \frac{w_1(w_2-1)+1)}{w_1} \\ 0 & w_1 & \frac{2(1-w_1)-w_2(1-2w_1)}{1-w_2} & \frac{w_1(1-w_2)-1}{1-w_2} \\ 0 & 0 & -\frac{w_2^2}{1-w_2} & \frac{w_2^2}{1-w_2} \end{bmatrix},$$
$$w_1 \equiv \frac{S_{j-1}}{S_j + S_{j-1}}, w_2 \equiv \frac{S_j}{S_{j+1} + S_j}. \tag{2.15}$$

where S_j is the length of panel j. In case the panel lies on either end of the shell, then quadratic Overhauser polynomials are sufficient to ensure continuity of the derivative at the inner edge of the panel. In that case, the coefficient matrix needs to be changed to:

$$b_{qk} = \begin{bmatrix} 1 & -w-1 & w & 0 \\ 0 & \frac{1}{1-w} & -\frac{w}{1-w} & 0 \\ 0 & -\frac{w^2}{1-w} & \frac{w^2}{1-w} & 0 \\ 0 & 0 & 0 & 0 \end{bmatrix},$$
$$w = \frac{S_j}{S_j + S_{j+1}}, \tag{2.16}$$

for a panel on the starting panel of the sheet and to:

$$b_{qk} = \begin{bmatrix} 0 & 0 & 0 & 0 \\ 0 & -\frac{w^2}{1-w} & \frac{w^2}{1-w} & 0 \\ 1 & \frac{2w-1}{1-w} & -\frac{w}{1-w} & 0 \\ 0 & 1-w & w & 0 \end{bmatrix},$$
$$w = \frac{S_j}{S_j + S_{j-1}}, \tag{2.17}$$

for a panel on the end of a sheet. The same concept is used at corner points where the potential jump is continuous but the derivatives can be unbounded. The two corner panels will be the start and end panels of their respective sheets. The evaluation of the integral in (2.10) then involves integrals of the form:

$$\int_{C_j} t^{k-1} \frac{\partial^2 G_n}{\partial n_P \partial n_Q}\, ds = \frac{1}{S_j^{k-1}} \int_0^{S_j} s^{k-1} \frac{\partial^2 G_n}{\partial n_P \partial n_Q}\, ds. \tag{2.18}$$

These integrals are regular (evaluated by standard numerical quadrature) except when the collocation point lies on one of the edges of the panel. The treatment of this last case requires special care and is detailed in Appendix A.

Once all influence coefficients are evaluated at the collocation points, we obtain a system

of equations that is solved for the potential jumps across the panels at the collocation points. We only collocate at points connecting two panels. We also assume that the normal vector at the collocation point is the mean of the normal vectors of the two panels. The end points of the sheet are assumed to have zero potential jump as the potential (and pressure) go back to being continuous in the body of the fluid. In fact, the jump in potential varies as $\sqrt{t}$ near $t = 0$ for a panel on the starting edge of the sheet and as $\sqrt{1-t}$ near $t = 1$ for a panel on the ending edge [41]. Polynomials cannot adequately represent that type of end behavior in general. However, by using a dense collection of panels near the edges, the effect will be very small, especially for the load computations which are integrated quantities. More precise end behavior could possibly be incorporated in the method in a manner similar to [13].

2.2.3 The Wave Loads and Surface Elevation

The wave loads on the body can be obtained by integrating the dynamic pressure over its surface. We define the dimensionless added inertia and damping coefficients as $\mu_{kp} = M_{kp}/\rho h\overline{A}a^c$ and $\lambda_{kp} = B_{kp}/\rho h\overline{A}a^c\omega$ respectively. Here, ρ is the water density and c is an integer ranging between 0 and 2 chosen to make the expressions dimensionless. $\overline{A}$ is the surface area of the internal region. The excitation force from the diffraction problem is also normalized as $f_k = F_k/\rho\eta_0 g\overline{A}a^{l-1}$ where the integer l was previously defined. The wave loads are then expressed by:

$$\mu_{kp} + i\lambda_{kp} = \frac{1}{Ah}\int_C\int_{-h}^{0}[\phi^p]\frac{\partial\phi^k}{\partial n}\,dyds, \tag{2.19}$$

$$f_k = -\frac{i\sqrt{\nu}}{A}\int_C\int_{-h}^{0}[\phi^7]\frac{\partial\phi^k}{\partial n}\,dyds. \tag{2.20}$$

Here, $A = \overline{A}/a^2$ is the dimensionless area which is $\pi, \pi b$ and 4 for the circlar, elliptical and square shells respectively. The normal gradient of the potential in these expressions was given in (2.4). Note that the incident wave does not contribute to the loads because the body has zero thickness. The integrals in these expressions are evaluated in Appendix B. It is also useful to visualize the free surface elevation over the wave field near the body. The expression for the elevation is obtained from the field potential through the integral equation and is given by:

$$\frac{\eta^S}{\eta_0} = e^{i\kappa_0(x\cos\beta+z\sin\beta)} + i\sqrt{\nu}Y_0(0)\int_C[\varphi_0^7]\frac{\partial G_0}{\partial n_Q}\,ds, \tag{2.21}$$

$$\frac{\eta^p}{U\sqrt{a/g}} = i\sqrt{\nu}\sum_{n=0}^{\infty}Y_n(0)\int_C[\varphi_n^p]\frac{\partial G_n}{\partial n_Q}\,ds, \tag{2.22}$$

$$\frac{\partial G_n}{\partial n_Q} = \frac{i\kappa_n H_1(\kappa_n R)}{4R}(\xi - x)n_\xi + (\zeta - z)n_\zeta. \tag{2.23}$$

The integrals in these expressions are regular and can be evaluated by standard methods.

2.2.4 The Haskind Relation

The well known Haskind relation [1] relates the diffraction forces to the radiation potential. It serves as an additional check to the validity of the results. The relation gives the force in (2.20) by:

$$\begin{aligned}
f_p &= -\frac{i\sqrt{\nu}}{A}\int_C\int_{-h}^{0}\left(\phi^0\frac{\partial[\phi^p]}{\partial n}-[\phi^p]\frac{\partial\phi^0}{\partial n}\right)dyds \\
&= \frac{i\kappa_0}{AY_0(0)}\int_C[\varphi_0^p]e^{i\kappa_0(x\cos\beta+z\sin\beta)}(n_x\cos\beta+n_z\sin\beta)ds \\
&= \frac{i\kappa_0}{AY_0(0)}\sum_{j=1}^{N}S_j((n_1)_j\cos\beta+(n_2)_j\sin\beta)e^{i\kappa_0(x_j\cos\beta+z_j\sin\beta)}\sum_{q=j-1}^{j+2}[\varphi_0^p]_qQ_{jq}(\beta), \qquad (2.24)\\
Q_{jq}(\beta) &= -\frac{b_{m1}P_j^3-b_{m2}P_j^2+2b_{m3}P_j-6b_{m4}}{P_j^4} \\
&+ \frac{(b_{m4}+b_{m3}+b_{m2}+b_{m1})P_j^3-(3b_{m4}+2b_{m3}+b_{m2})P_j^2+(6b_{m4}+2b_{m3})P_j-6b_{m4}}{P_j^4}e^{P_j}, \\
P_j(\beta) &= ik((x_{j+1}-x_j)\cos\beta+(z_{j+1}-z_j)\sin\beta).
\end{aligned}$$

Here, it is understood that for a panel on the left edge of the shell, $q\in[j,j+2]$ and for one on the right edge, $q\in[j-1,j+1]$. $(n_k)_j$ is the normal component of the panel j in direction k. We also used $m=q-j+2$ so that $m\in[1,4]$. Again, m should be modified at the outermost panels to $m=q-j+1$ and $m=q-j+3$ for the left and right panels respectively. The points x_j and z_j are the starting points of panel j.

The Haskind relation was used to verify the results. It also provides a means for a fast calculation of the diffraction loads once the radiation problem is solved.

2.3 Results and Discussion

The method presented above can be used to simulate the wave field over any thin vertical cylinder. Multiple bodies could be handled the same way as well. In this work, we present results for elliptical and square shaped open cylinders as an example of the application of the method and in order to understand the effect of the opening. The cross-sections and definitions of their dimensions are shown in figure 2.2.

Two elliptical shapes are considered. The first is simply a circle with $a=b=1$ and the second is such that $a=1, b=1.5$. Both have an opening $2\theta_0$ as shown in figure 2.2. The third shape has a square cross-section of side length $2a$ and opening d. The openings are oriented along the positive x-axis.

2.3.1 Validation of Results

The results of this method were compared to that in the lower order method in the works in [22, 33]. These last two references were verified separately using results in the literature. The results are also compared to the case of diffraction and radiation from an open circular cylinder, which could be obtained using a matched eigenfunction expansion method similar to [42] but is more involved and will not be shown here although it was found to match the results obtained.

Furthermore, as the frequency approaches zero, the dimensionless added mass results should approach those for the corresponding two dimensional bodies with the same shape. We present here a comparison of our results with those for a two-dimensional closed square cylinder of side length $2a = 2$ in a potential field. This comparison is useful because in the two-dimensional limit, the equation retains its hypersingular nature as well as the difficulty associated with having geometrical corners. The potential jump around a corner is continuous but its derivative is unbounded though integrable. As mentioned earlier, this is taken into account in the present method. The added mass and mass of inertia in surge and yaw motion, respectively, for the external flow were given in [43] to be $\mu^e_{11} = 4.745$ and $\mu^e_{66} = 0.725$. The surge added mass of the internal flow is simply the entrained internal mass which is $\mu^i_{11} = 4.0$ while the yaw mass moment of inertia is more involved. The yaw potential of the internal flow is obtained analytically as an eigenfunction expansion:

$$\begin{aligned} \Phi_i &= \Phi(x,y) - \Phi(y,x), \qquad (2.25)\\ \Phi(x,y) &= \sum_{n=1}^{\infty} a_n \cos\frac{n\pi(1+y)}{2}\left(\cosh\frac{n\pi(1+x)}{2} - \cosh\frac{n\pi(1-x)}{2}\right),\\ a_n &= -\frac{8((-1)^n-1)}{\pi^3 n^3 \sinh n\pi}. \end{aligned}$$

The yaw added mass moment of inertia is then given by:

$$\mu^i_{66} = \sum_{n=1}^{\infty} \frac{16 a_n}{n\pi}\left(\sinh n\pi + \frac{3-(-1)^n}{n\pi}(1-\cosh n\pi)\right). \qquad (2.26)$$

This trurns out to be $\mu^i_{66} = 0.417$. The total added mass is the sum of the internal and external contributions so that $\mu^t_{11} = 8.745$ and $\mu^t_{66} = 1.142$. The error of the numerical method is then defined as:

$$E_j = \frac{|\mu_{jj} - \mu^t_{jj}|}{\mu^t_{jj}}. \qquad (2.27)$$

Figure 2.3 is a plot of the natural logarithm of the error versus that of the step size δ for the closed square case (κ_0 is taken as 0.01 in the numerical method). A uniform mesh is used with 60-140 panels. From the slopes of the curves, we can see that $E_1 \sim \delta^{1.91}$ and $E_6 \sim \delta^{1.45}$ which is less than the second-order accuracy expected but better than first order accurate. These convergence rates are typical of this method for other geometries as well.

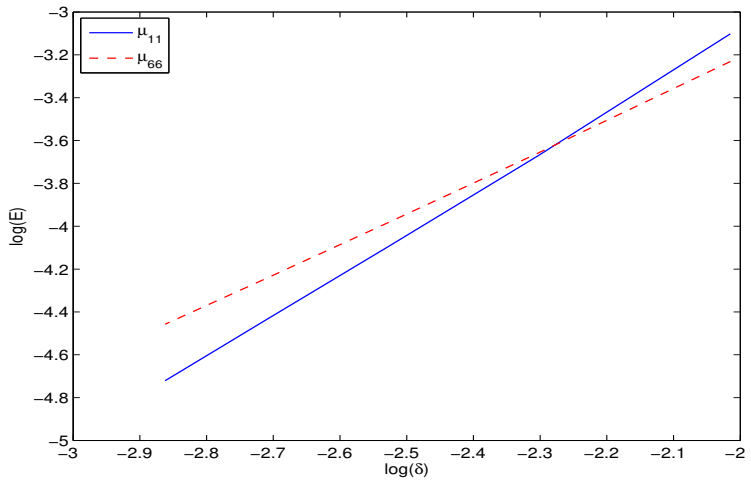

Figure 2.3: Plot of $log(E_j)$ vs $log(\delta)$ for the closed square case at $\kappa_0 = 0.01$ and $h = 3$. The slopes of the lines are 1.91 and 1.45 respectively

A simulation with 130 panels using a cosine distribution leads to an error less than 0.5% for all loads.

All results presented in this work are for a water depth $h = 3$. We used 75 and 100 panels for the circle and ellipse respectively and 112, 120 and 128 panels for the three square-shaped shells varying with the decreasing opening size. This is sufficient for graphical accuracy. The grid points are concentrated near the edges and the corners according to a cosine distribution for better accuracy. The Overhauser elements are known to perform well near corner points. For the radiation results, 4 modal terms were found sufficient for our purpose.

2.3.2 Diffraction Results

To understand the effect of opening the cylinder, it is useful to compare the amplitude of the free surface elevation around the open and closed bodies. Figure 2.4 shows the amplitude of the wave field over a circular cylinder for a wave approaching along the positive x-axis ($\beta = 0$). These plots are useful because they indicate the position and amplitude of the highest waves. This is usually at the first point of contact with the obstacle. At low frequencies ($\kappa_0 < 0.1$), the amplitude inside the body is comparable to the highest value outside because the wave does not "see" the body so well. This visibility of the body becomes stronger as the frequency increases and the opening size decreases. The surface elevation is also representative of the pressure field over a certain region. Having a difference in the elevation on opposite sides of the cylinder creates a force acting in the normal direction. Because the field is symmetric about the x-axis in this case, the net force f_1 will be a result of the difference between the regions in the back and front sides of the body. We expect a higher load on an open body than the closed one, provided the difference in surface elevation is comparable in both cases, because the opening area does not contribute to any force on

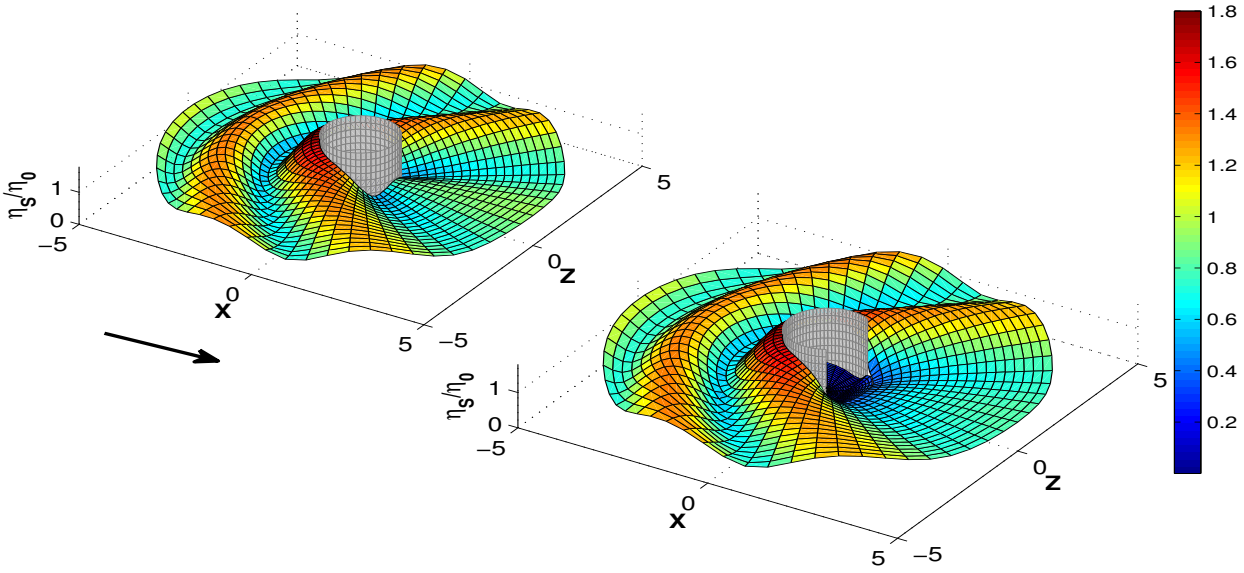

Figure 2.4: Surface amplitude of the diffraction field over a closed (left) and open (right, $\theta_0 = \pi/3$) circular shell at a wave direction $\beta = 0$ (indicated by arrow) and $\kappa_0 = 1.5$ (The colors indicate surface amplitude)

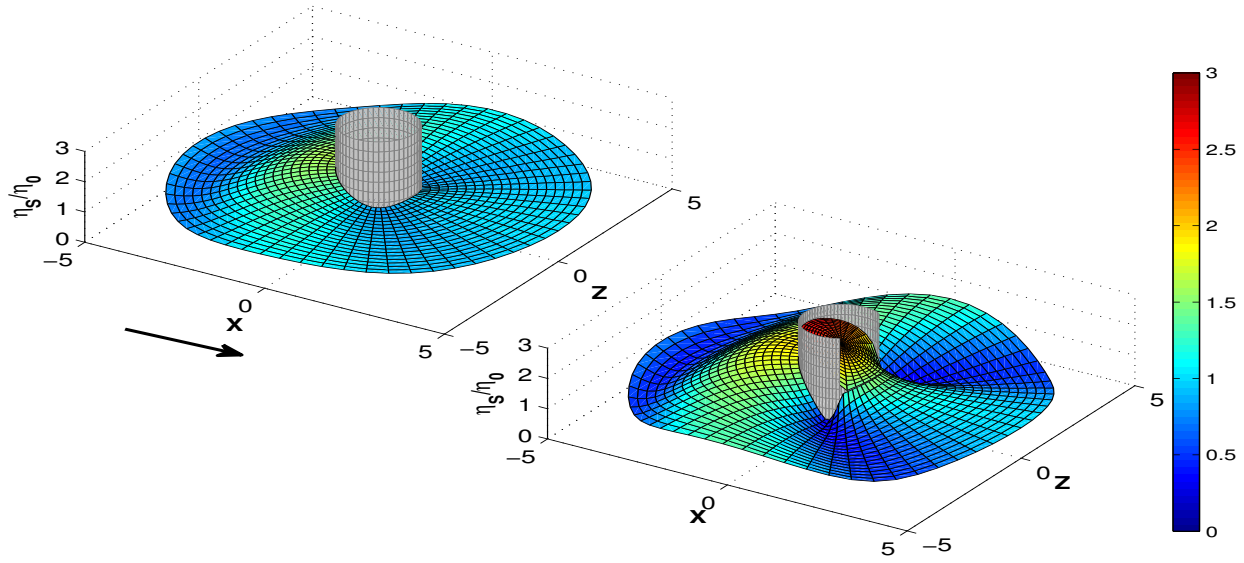

Figure 2.5: Surface amplitude of the diffraction field over a closed (left) and open (right, $\theta_0 = \pi/3$) circular shell at a wave direction $\beta = 0$ (indicated by arrow) at the Helmholtz mode where $\kappa_0 = 0.65$ (The colors indicate surface amplitude)

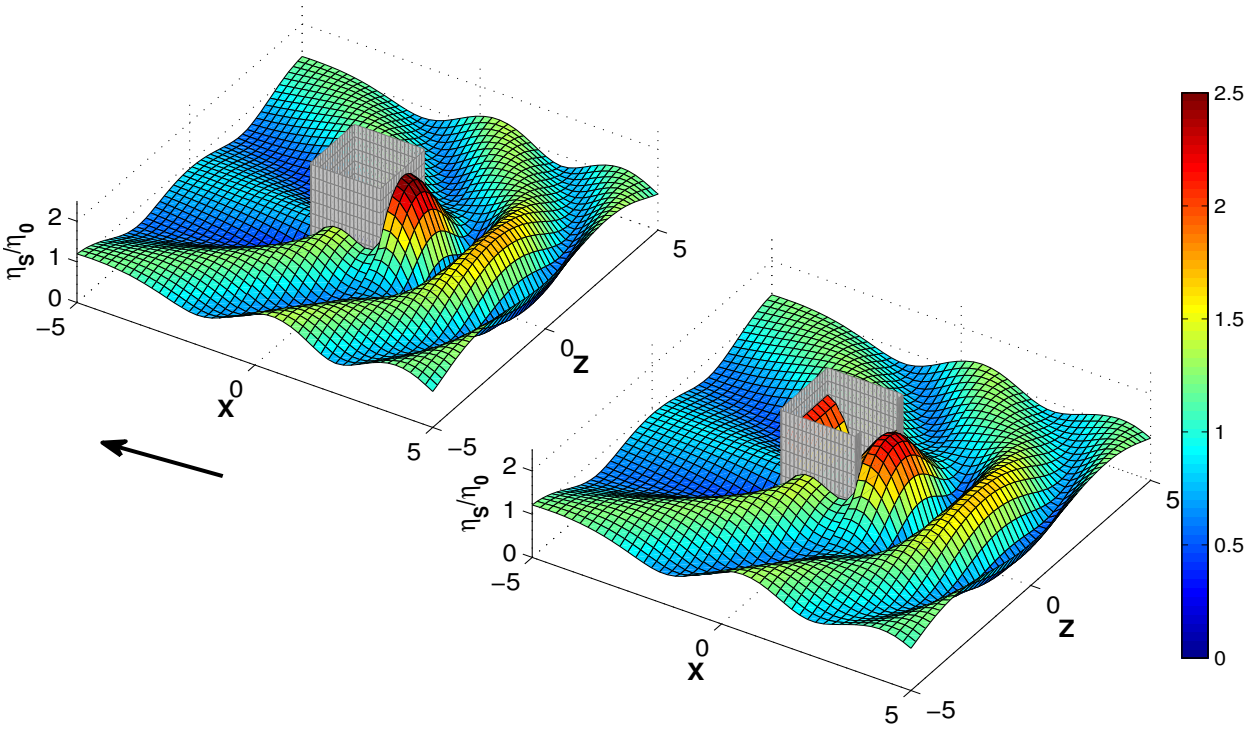

Figure 2.6: Surface amplitude of the diffraction field over a closed (left) and open (right, $d = 1.5$) square shell at a wave direction $\beta = \pi$ (indicated by arrow) and $\kappa_0 = 1.5$ (The colors indicate surface amplitude)

the body that would balance the pressure on the back side.

Figure 2.5 shows the diffracted wave field amplitude over the circular shell as in the previous case but at the Helmholtz mode. The wave amplitude inside the shell rises to very high levels (according to the theory considered here) and more so as the shell opening size decreases. This leads to high loads on the body. The wave amplitude outside the shell is also greater when the body is open.

The last surface plot in this section is for an incident wave propagating in the negative x-direction and diffracting from a square shaped shell (figure 2.6). Because of the opening present, the force f_1 in this case will be different than the one for a wave along $\beta = 0$. The former case also shows a higher surface amplitude inside the body when compared to the latter case. The higher amplitude inside occurs on the opposite side of the opening as expected.

The rest of the results in this section are plots of the amplitudes of the loads acting on the shell because of the diffracted wave field. We note that the incident wave potential does not contribute to the loads because the body has zero thickness. The loads are the result of the

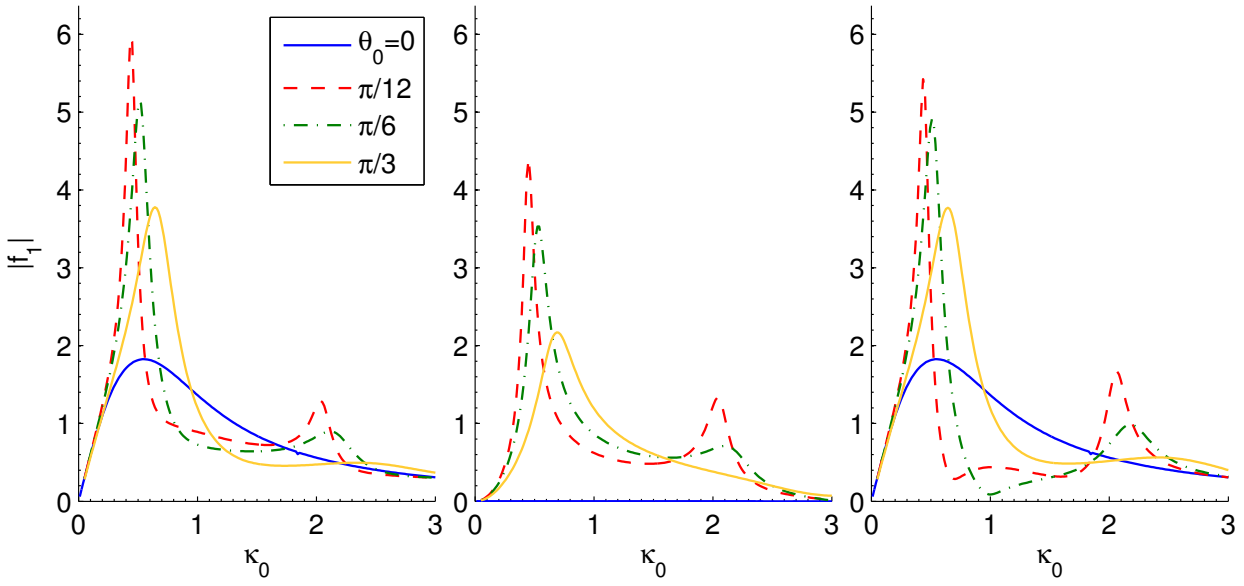

Figure 2.7: Diffraction forces f_1 on the circular shell in 3 wave directions: $\beta = 0$ (left), $\beta = \pi/2$ (middle) and $\beta = \pi$ (right)

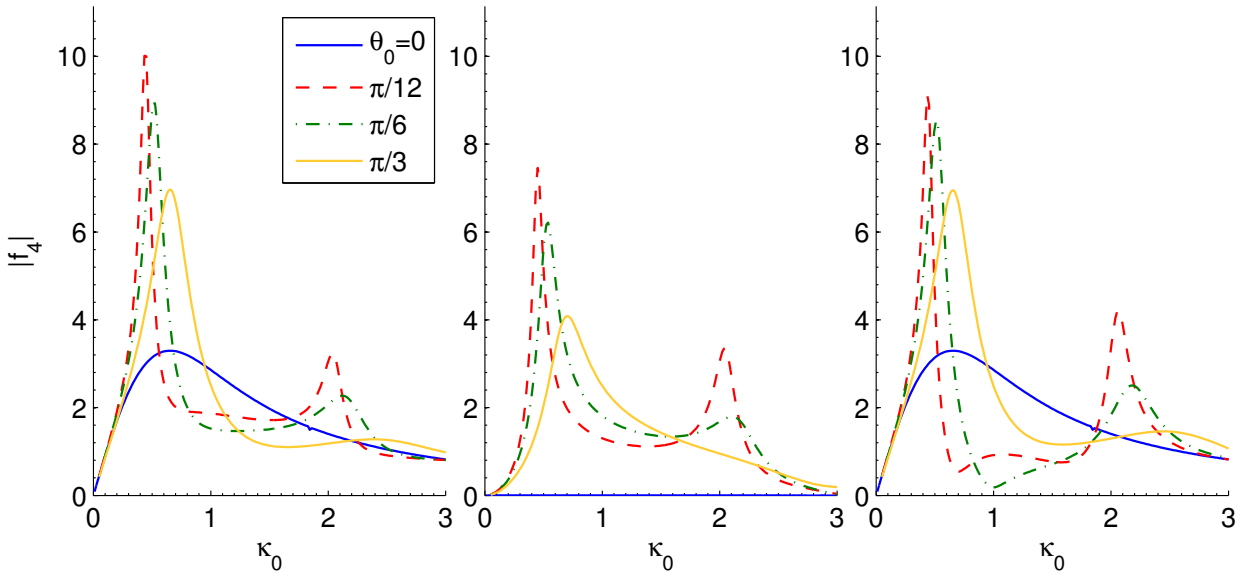

Figure 2.8: Diffraction moments f_4 on the circular shell in 3 wave directions: $\beta = 0$ (left), $\beta = \pi/2$ (middle) and $\beta = \pi$ (right)

correction potential only.

The results in figures 2.7 & 2.8 show the force and moment in the x-direction for different incident wave directions. The moment results are very similar to the force ones and are of the order of the force results multiplied by a factor $h/2$. This is to be expected as the moment is a result of that force. In fact, this similarity extends to all forces and corresponding moments (in the same direction) in this work and we will therefore restrict ourselves to forces for brevity. The results in the first plot of figure 2.7 indicate that a very large force results at lower frequency when the body is opened. Although the force on the closed body peaks in this range as well, the open body force is observed to be much sharper and larger, especially as the opening gets smaller. This is the "Harbour Paradox" [2, Ch5]. This force then decreases well below the closed body case to peak again above the Helmholtz mode of the closed inner region. Note that in reality, the forces would not be so large because of the effects of friction at the entrance and nonlinearities which we have neglected here. An approximate theory for long waves that takes friction into account [2, Ch6] shows that the peak at the Helmholtz mode completely disappears when there is sufficient friction at the opening. The theory presented here will become a better approximation as the opening size increases. Nonlinearity can also play a role by moving the energy from the lower to the higher harmonics. This should be particularly important around the Helmholtz mode as the amplitude of the surface becomes larger. As indicated in [44, Ch12], nonlinearity effects are expected to dominate (even over friction) as the harbor length increases along the direction of wave propagation compared to the width.

The elevation inside the closed shell is always zero. The load, which is related to the difference in elevation on opposite sides of the shell, results from the high amplitude waves on the outer side of the wall just upstream of the shell. This is balanced, to a certain extent by the difference downstream. In the case of an open shell, this balancing effect disappears and larger forces are observed. At the Helmholtz (pumping) mode, the elevation inside the shell is almost uniform except near the opening [45]. The same thing is also observed for a moonpool with a bottom gap [46]. The body is essentially acting as a Helmholtz resonator in this long wave limit. As the body is opened, it becomes possible to excite the internal region which leads to the larger loads. In between the two peaks, the elevation inside the shell is close to that outside. In fact, most of the pressure difference occurs close to the edges at the opening where wave heights are small. The resulting loads are significantly lower than those on the closed body.

When the incident wave approaches at $\beta = \pi$, even lower loads result in that frequency range when compared to the closed shell. In fact, we can see near zero loads in that case (figure 2.7). This hints that by properly choosing the opening size, it is possible to achieve zero loads on the body. The zero load frequencies could be tuned to be close to the peak of the wave field spectrum in an irregular wavefield. The results are also seen to be somewhat insensitive to changes in frequency so the possibility of designing the opening to reduce loads on the structure may be viable. The results in the middle plot of the same figure are also important because these loads only arise when the body is open. This is because of the asymmetry that is introduced by having an opening. These loads can be seen to be of the

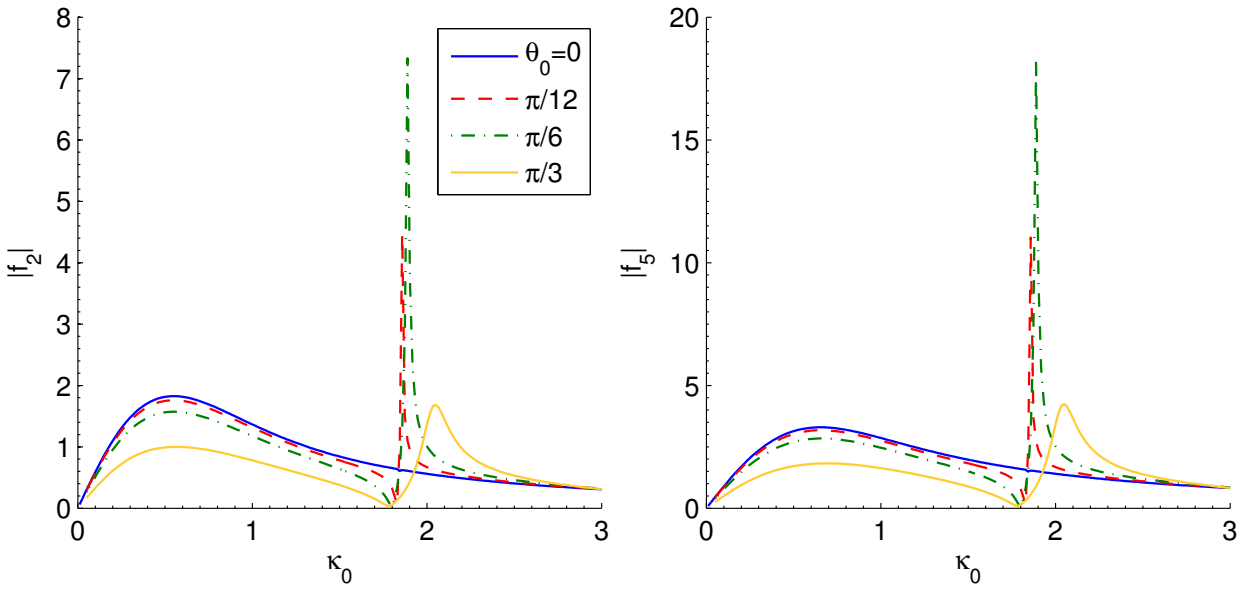

Figure 2.9: Diffraction loads f_2 (left) and f_5 (right) on the circular shell in wave direction $\beta = \pi/2$

same order of magnitude as the loads when the wave is directed along the opening direction.

Figure 2.9 shows the force and moment on the circular shell in the z-direction when the incident wave approaches in that same direction. The interesting result here is the possibility of having a zero force and moment on the body for a certain frequency and for all openings as long as the body is open.

The results in figure 2.10 are for an elliptical shell and are analogous to those in figure 2.7. The loads appear similar to those of the circular shell and the general behavior can be described in a similar manner. This indicates that the shape of the harbor has little effect on the physical behavior. The normalized loads on the elliptical shell are found to be slightly lower than those on the circular one when the body is open in contrast to the closed case. The dimensional loads will be greater though because the elliptical shell is larger in size.

Because of symmetry, the force and moment in the z-direction and the yaw moment are only nonzero when the incident wave approaches at a direction $\beta = \pi/2$ even when the body is open. We present those cases in figure 2.11. Again, the force and moment in the z-direction are similar. We notice that the loads decrease from the closed body case when the opening increases. This has to do with higher wave elevations inside the shell and therefore less differences with the outside. High elevations inside are not observed except close to the resonance frequency. Again, it is possible to have points of zero loads at certain frequencies when the body is opened. The yaw moment in the right plot of figure 2.11 is also of interest because it only appears for an open body. The behavior is a bit more complicated for this moment than the rest of the loads because it depends on forces in both horizontal directions.

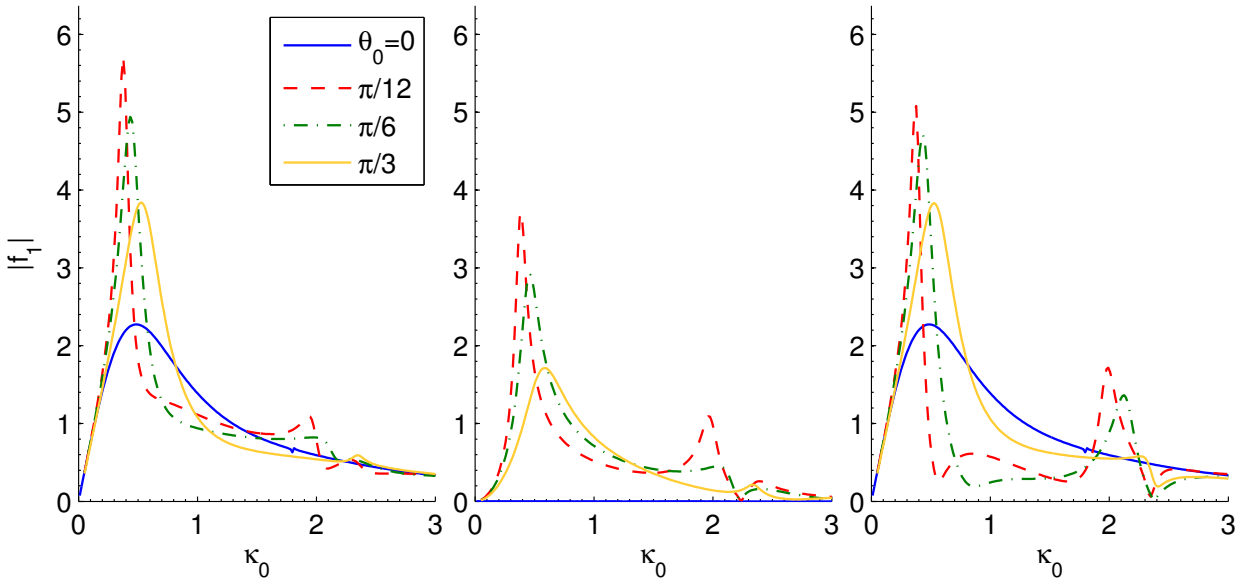

Figure 2.10: Diffraction forces f_1 on the elliptical shell in 3 wave directions: $\beta = 0$ (left), $\beta = \pi/2$ (middle) and $\beta = \pi$ (right)

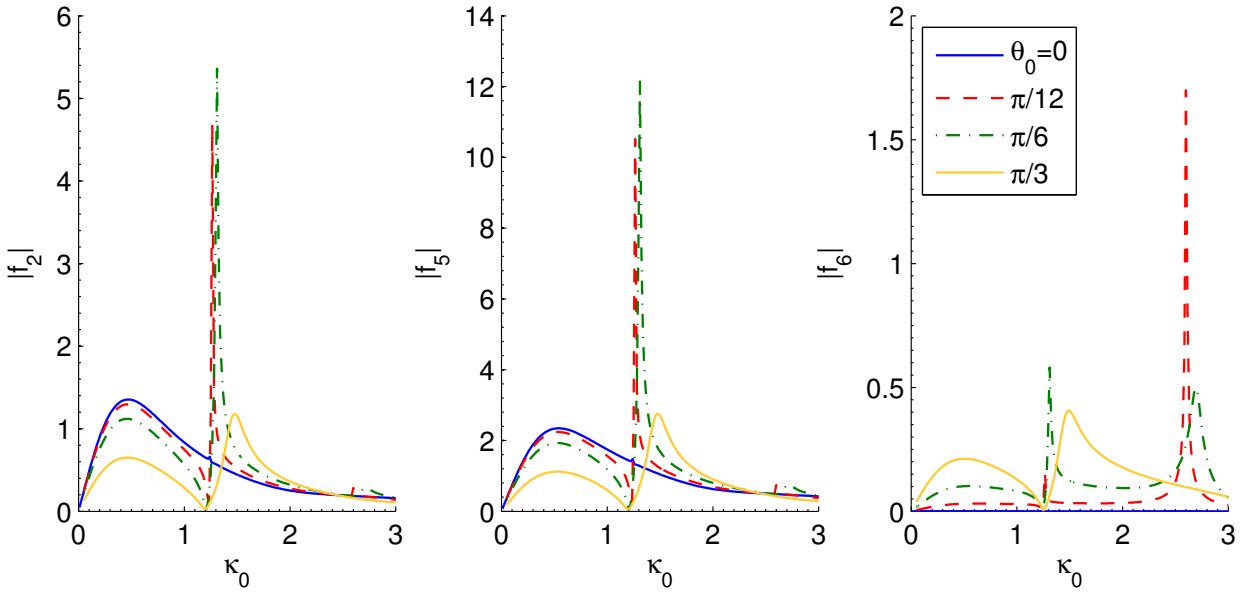

Figure 2.11: Diffraction loads f_2 (left), f_5 (middle) and f_6 (right) on the elliptical shell in wave direction $\beta = \pi/2$

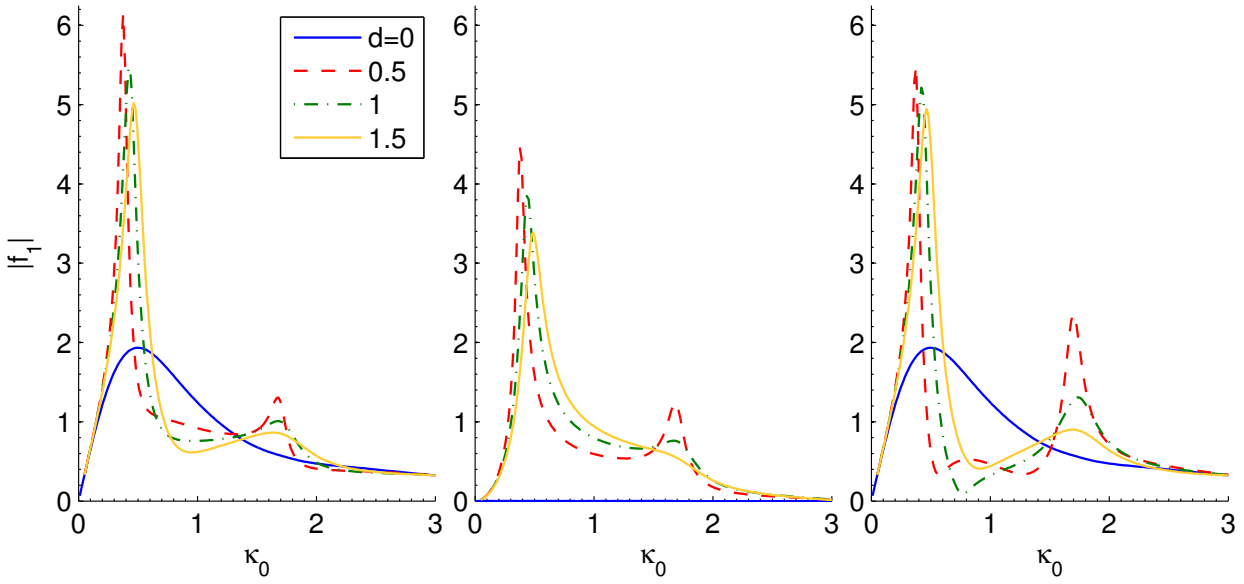

Figure 2.12: Diffraction forces f_1 on the square shell in 3 wave directions: $\beta = 0$ (left), $\beta = \pi/2$ (middle) and $\beta = \pi$ (right)

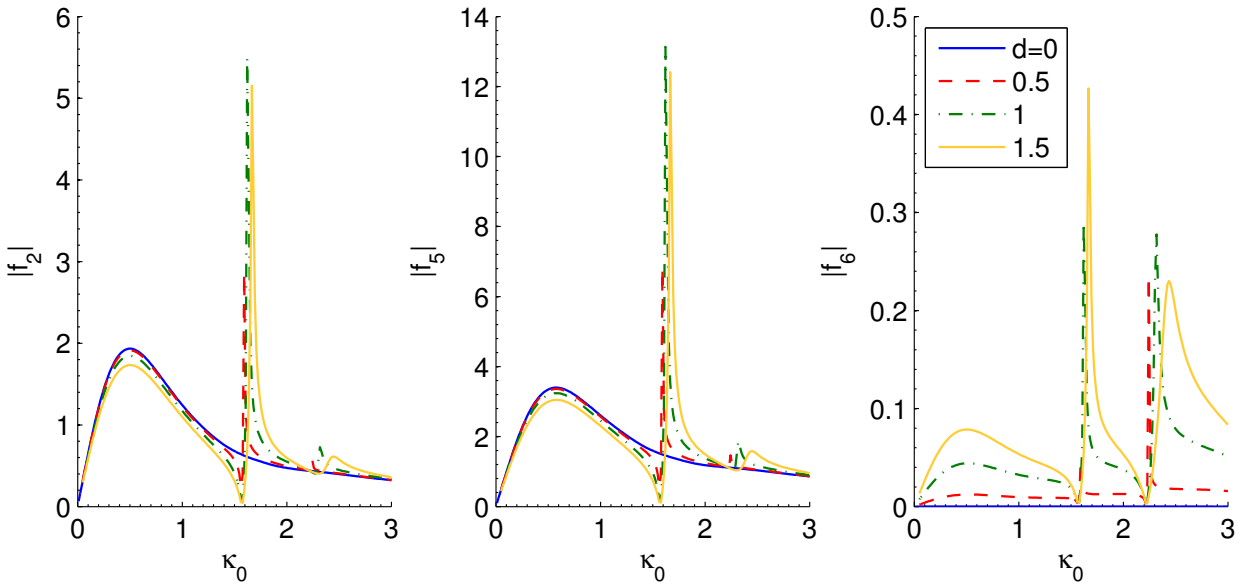

Figure 2.13: Diffraction loads f_2 (left), f_5 (middle) and f_6 (right) on the square shell in wave direction $\beta = \pi/2$

The forces do not balance because of the asymmetry created by the opening inside the body and in the wake and the net effect is a moment about the y-axis.

The case of the square shell is similar to the circle and ellipse. Figure 2.12 shows the wave force in the x-direction for 3 incident wave directions while figure 2.13 shows the wave loads in the z-direction and the yaw moment when the incident wave approaches from the side in a manner analogous to figure 2.11. For loads resulting from beam waves, points of zero force are clearly possible for all opening sizes as long as the shell is open.

The first resonant wavenumbers for the open circular and square bodies in figures 2.7 & 2.12 can be compared to those of the corresponding closed bodies. Those latter ones are $\kappa_0 = \pi/2$ for a square and $\kappa_0 = 1.8412$ for a circle moving in surge. This last value is the root of $\partial J_1(\kappa_0 r)/\partial r$ at $r = 1$ for the Bessel function of first kind and first order, which is well known. An important question here is why do we observe resonance at low frequencies for the open shell although these are far from the first natural frequencies of the closed shell. A simple analogy can be made with the problems of wave propagation over a string or in a gas tube. It is well known that the resonant behavior of a string connected to a wall is different from that with a free end. The same can be said about a gas tube with a closed or open ends. For a closed-opened tube (analogous to the open case), the first resonant wavenumber ($\kappa a = \pi/4$) in a gas tube of length $2a$ becomes half of its value for the closed-closed tube ($\kappa a = \pi/2$). The second resonant wavenumber ($\kappa a = 3\pi/4$) for the closed-open tube is triple the first one [47]. This is similar to what we observe for the open harbor where the first resonance is dramatically shifted to lower frequencies as the shell is opened. The second resonance also occurs somewhere on the order of triple the first resonance. An equivalent statement is to say that damped systems (radiating open bodies) are known to have lower resonant frequencies. Naturally, our problem is more involved than the case of a string or gas tube because of the more complex geometries, the three dimensional effects and the presence of an outer domain.

It was observed that at certain opening size and frequency values, the load along the x-axis approaches zero. This behavior is observed for an incident wave approaching at $\beta = \pi$ but not for the case when $\beta = 0$. This leads to the surprising observation that directing an open structure towards the incident waves leads to lower loads than directing it the opposite way around. We found that the values $\theta_0 = [0.1441\pi, 0.1265\pi], d = 0.89$ at wavenumbers $k = [0.916, 0.704, 0.726]$ are representative of the zero load conditions (numerically $|f_1| < 0.007$) for the circular, elliptical and square bodies considered in this work.

2.3.3 Radiation Results

Although the cylinder is bottom mounted, it is still useful to know its radiation properties because it could still be connected to the bottom using a suitable joint that allows its motion or it could represent a reasonable model for truncated cylinders with a long enough draft. This approximation is expected to work better for the open shell because the fluid could escape through the opening easier than through the bottom gap and the effect of this gap will be less important.

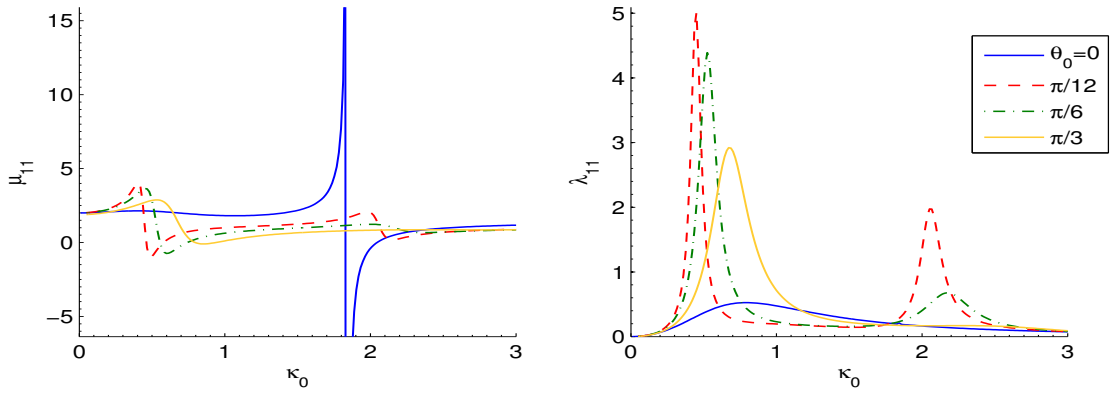

Figure 2.14: Radiation surge added mass μ_{11} (left) and damping λ_{11} (right) coefficients for the circular shell

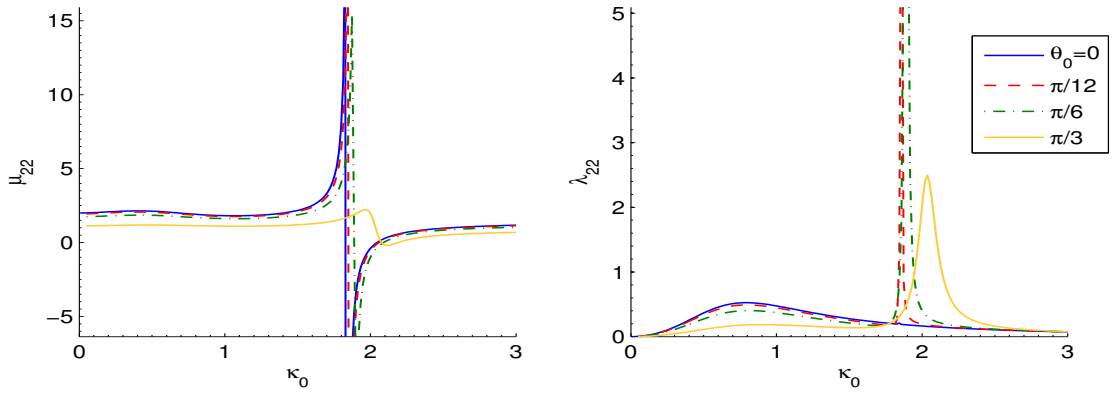

Figure 2.15: Radiation sway added mass μ_{22} (left) and damping λ_{22} (right) coefficients for the circular shell

Figure 2.14 shows the added mass and damping coefficients of a surging circular shell. The closed shell added mass shows resonant behavior as expected. Opening the shell slightly increases the resonant frequency and drastically reduces the added mass at resonance. This is because the fluid can now escape the inner region. Another peak in added mass appears at lower frequencies as was the case for diffraction forces. The damping coefficients also peak at these points. This range of frequencies is characterized by an increase in the free surface elevation to very high levels, which causes high pressure differences across the wall. Again, as for the diffraction problem, the absence of a balancing force where the opening is located leads to a high net force on the shell.

Figure 2.15 shows the coefficients for the swaying circular shell. The results indicate a slight decrease in both coefficients and a slight shift of resonance towards higher frequency as the opening size increases. Close to resonance, the added mass changes to finite extrema while the radiation damping significantly increases as waves from inside escape to the outer

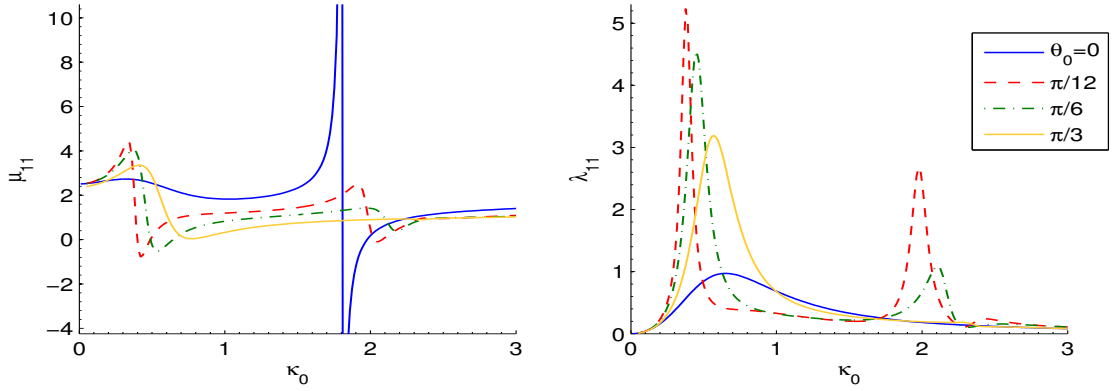

Figure 2.16: Radiation surge added mass μ_{11} (left) and damping λ_{11} (right) coefficients for the elliptical shell

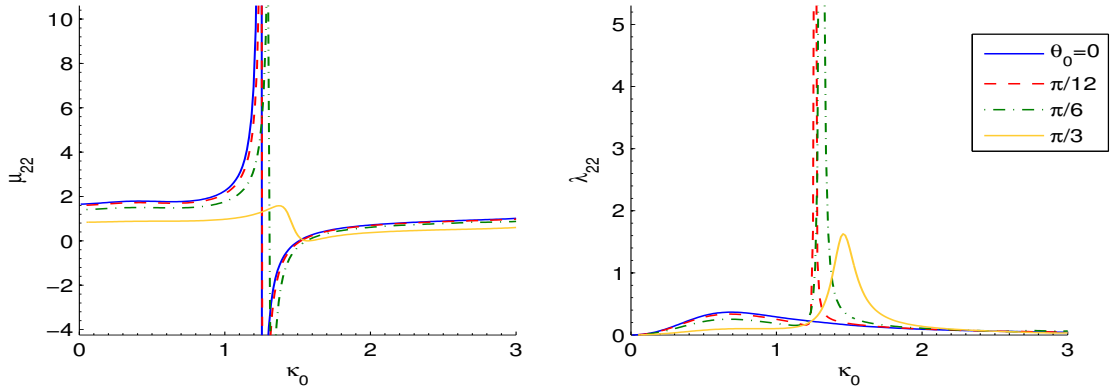

Figure 2.17: Radiation sway added mass μ_{22} (left) and damping λ_{22} (right) coefficients for the elliptical shell

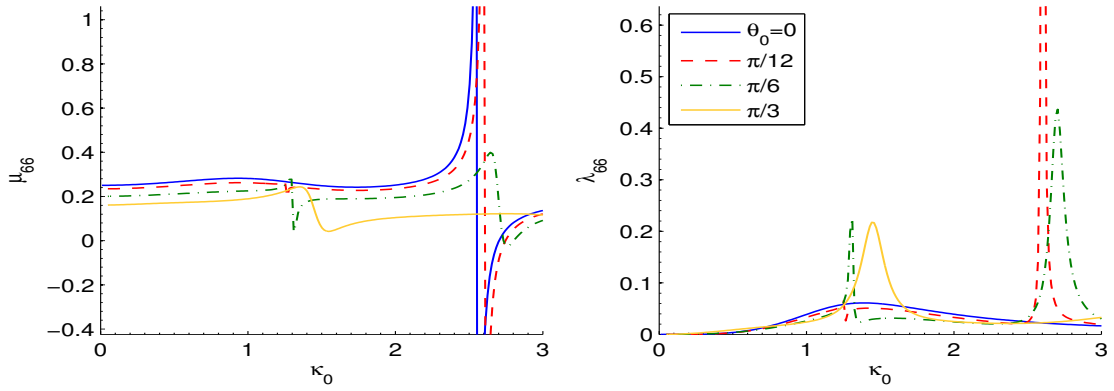

Figure 2.18: Radiation yaw added inertia μ_{66} (left) and damping λ_{66} (right) coefficients for the elliptical shell

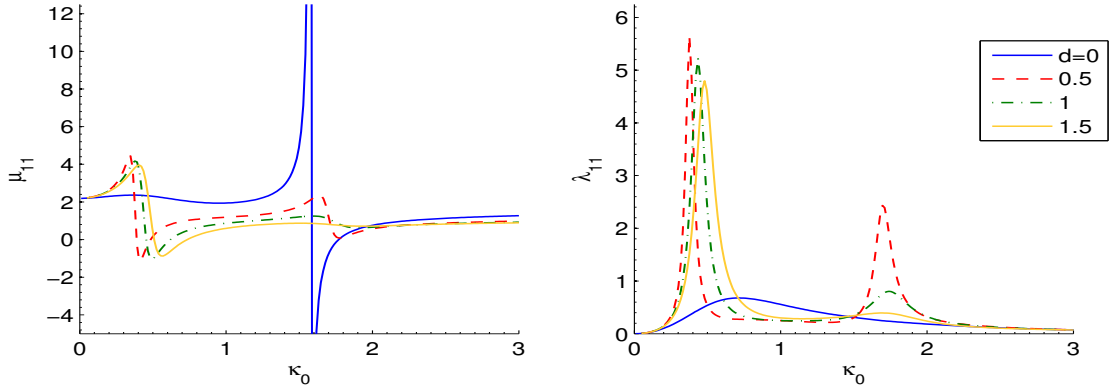

Figure 2.19: Radiation surge added mass μ_{11} (left) and damping λ_{11} (right) coefficients for the square shell

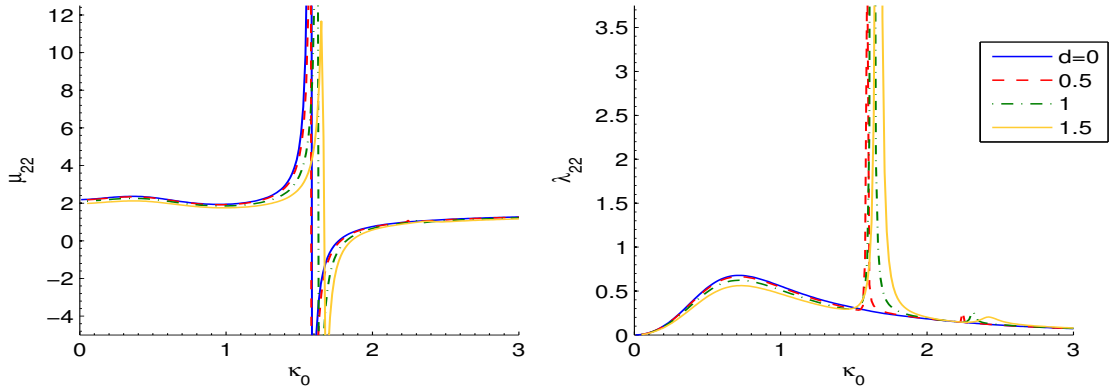

Figure 2.20: Radiation sway added mass μ_{22} (left) and damping λ_{22} (right) coefficients for the square shell

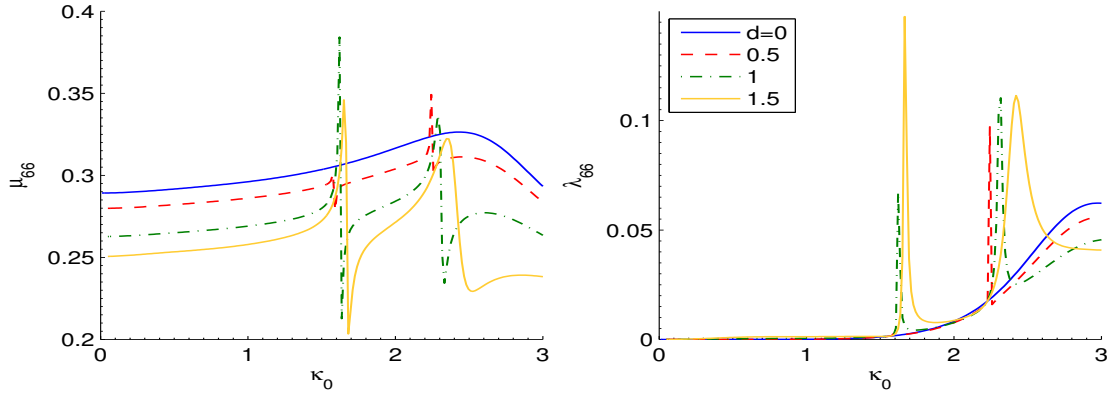

Figure 2.21: Radiation yaw added inertia μ_{66} (left) and damping λ_{66} (right) coefficients for the square shell

field. This case could be used as a wavemaker that generates a single desired frequency. The effect of resonance is reduced as the opening size increases.

Figures 2.16 & 2.17 present the radiation coefficients for the elliptical shell moving in surge and sway respectively. The results are qualitatively very similar to those of the circular cylinder. The magnitudes are slightly higher though. It is interesting to note that the resonance frequency is the same as that of the circular shell in the surge motion and lower in the sway motion. This is because the resonance in the sway direction is mostly governed by the length b rather than a.

Figure 2.18 shows the yaw added inertia and damping coefficients for the elliptical shell. These coefficients are zero for the circular cylinder. The distinctive feature of these coefficients is the dominance of higher frequencies when compared to the other motions. Opening the shell leads to a large increase in the radiation damping close to the resonant frequency as in the previous cases. The fact that this occurs at a higher frequency requires further attention to this motion if open floating bodies are to be considered for ocean applications.

Figures 2.19, 2.20 and 2.21 show the radiation coefficients on the square shaped shell in the surge, sway and yaw directions. The results for surge and sway are similar to those of the circle and ellipse. The shape of the body does not come in significantly for these coefficients. One might expect that this would be different for the yaw motion because the force is completely a result of the body shape and this is indeed the case. The yaw coefficients are seen to be quite different from those of the elliptical shell.

It is interesting to draw similarities of the radiation results with the case of a cylinder in a channel. This latter case was presented in [48] as well as [49]. First note that the added mass and damping in figures (2.14-2.21) appear to have their peak values over similar wavenumber positions. Furthermore, the magnitude of the damping at the peak (either peak) and the extent of the corresponding added mass jump behavior are somewhat equal. This is not unlike the case presented in [49] in which the authors gave a heuristic argument of why the extent of the spikes in added mass and damping are nearly the same. The same argument can be used in this case if a simple pole in the complex load $(\lambda + i\mu)$ behavior exists below the real axis. The similarity also extends to the case of a cylinder that is eccentric (not centered) along the channel width and swaying below the first cutoff frequency. In this case, propagating modes are possible in addition to the trapped mode and the behavior resembles our open cylinder case. When there is no eccentricity, only the trapped mode is present and the radiation damping vanishes. This resembles what happens in the internal region of the closed body case. One could not help but notice then the similarity in the radiation loads as presented in this last reference and our results. In particular, the peaks in the added mass and damping are shifted to higher wavenumbers as the opening size (analogous to eccentricity) increases. Recently, reference [50] reported a similar observation for the case of two flap-type energy converters facing each other when compared to a single converter facing the coast.

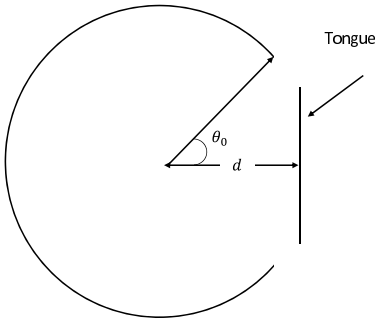

Figure 2.22: Schematic for the harbor and breakwater model

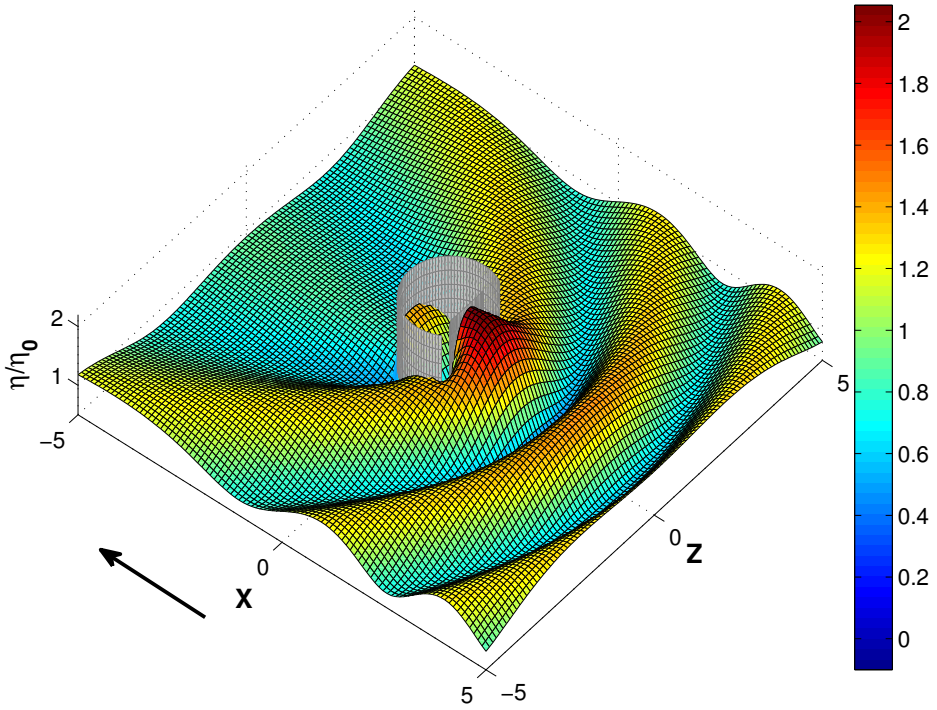

Figure 2.23: Diffraction over the circular shell with the tongue present at a wave direction $\beta = \pi$ and $\kappa_0 = 1.5$ (The colors indicate surface amplitude)

2.3.4 Harbor With a "Tongue"

Finally, it would be interesting to see what is the effect of having a breakwater (tongue) at the mouth of the harbor, an idea suggested by the proposal to build floating harbors off the US coasts (the Portunus Project). We will only present the most important case, which is when an incident wave approaches at $\beta = \pi$ and hits the breakwater. A simple harbor

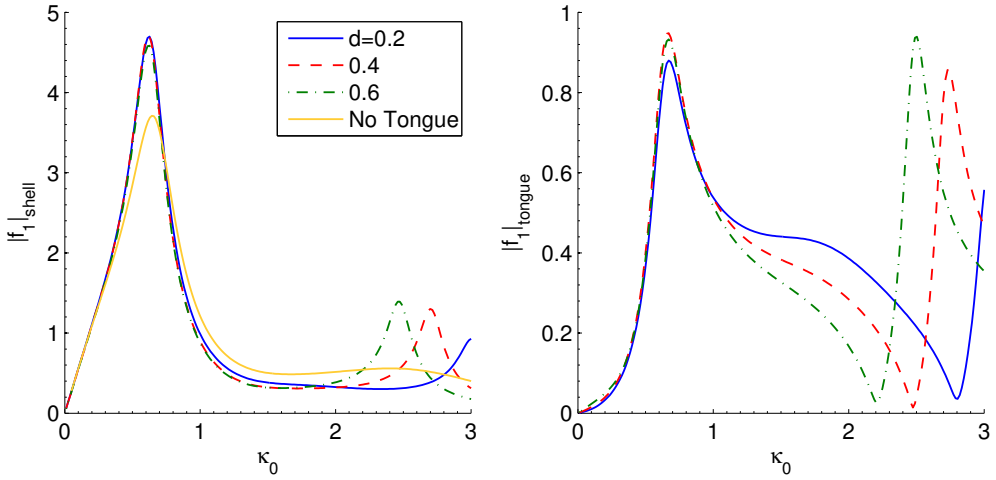

Figure 2.24: Diffraction force amplitude $|f_1|$ on the shell (left) and on the tongue (right)

model consists of a circular shell and a straight tongue oriented along the z-axis (figure 2.22). This should capture most of the desired physical effects. The computer program described in this work has been modified to accommodate multiple bodies and the shell and tongue are considered as separate elements. We consider the effect of the distance d of the tongue from the center of the shell. The length of the tongue in this example is equal to one shell radius and the mouth size is taken to be $\theta_0 = \pi/3$ with the same definition as before. Figure 2.23 shows the amplitude of the free surface as a head wave hits the tongue.

Figure 2.24 shows the amplitude of the force in the x-direction on both the shell and the tongue and comparison is made in the first case with the shell without a tongue. The force is defined as in (2.20) and the area of the harbor is used for normalization. We used 100 panels on the circular shell and 67 on the tongue concentrated near the edges to obtain these results.

The results indicate that the force on the shell is actually significantly higher near the first resonant frequency when the tongue is present. Again, this is similar to the Harbor Paradox described earlier and the limitations discussed earlier apply here as well. In particular, the high amplitude of the force is expected to be lower in reality, especially when the effective opening size becomes smaller. The position of the tongue does not seem to be significant in the frequency range considered though. The force on the tongue itself peaks in this range as well, although the total force is less than that on the shell. As the frequency of the incident wave increases, the breakwater comes into play and causes a reduction in the loads on the shell. The position of the tongue is significant in determining the second resonant frequency and the force amplitude at that peak. As the breakwater is moved farther away from the center of the shell, both the second resonant frequency and force amplitude move to lower values. Solution for harbor shapes other than a circular rim can be obtained with little difficulties, though not pursued here.

Chapter 3

The Added Mass of Thin Plates of Arbitrary Shapes

3.1 Introduction

In chapter 2, we presented a method to find a numerical solution to the water-wave problem with an infinitely thin body. We showed that when the depth variation is factored out, the problem can be formulated as a hypersingular integral equation for the two dimensional Helmholtz equation. The solution requires the treatment of one dimensional hypersingular integrals which we performed using a higher order method.

In this chapter, we look at a similar problem in a general sense but very different implementation-wise. Here we consider the added mass values for infinitely thin plates of general shapes. This still requires handling the hypersingular kernels we faced in the previous chapter but the problem is now fully three dimensional and the solution to the boundary integral method requires discretization over a two dimensional surface. For simplicity, we neglect the presence of any free surface and the domain is considered to be infinite. This work has been submitted for publication at the time of writing this thesis [51].

The added mass of flat plates is useful in practice as it appears in many engineering disciplines that have to deal with fluid flows. A triangular flat plate for example, can be used to model an aircraft as it moves perpendicular to the flat surface. A similar problem is that of modeling the motion of butterfly wings using flat plates. Finding the difference in added mass of different shapes might shed some light on why wings are shaped the way they are. For marine structures, flat plates appear as structural stiffeners or as motion dampers. The oars traditionally used to drive the motion of smaller boats can be modeled as flat plates as well. We will be particularly interested in plates with holes as those frequently appear in applications but seem to be missing from the literature. Example references for added masses of some general shapes are [52] and [53].

In what follows, we will first present the formulation of the problem and our approach, and then will show results for common shapes that are not available in the literature. The goal here is to make these results readily available for anyone who needs them and had to previously rely on approximations.

3.2 Problem Formulation

Consider a coordinate system xyz with the z-axis pointing upwards (perpendicular to the plates we consider here). Then the flow over the plate can be represented using a velocity potential. We consider three modes of motion (heave, roll and pitch) for the plate with

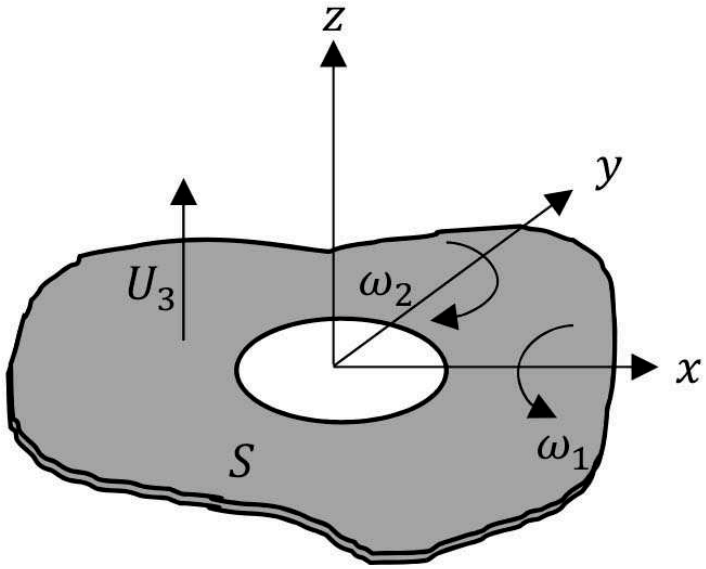

Figure 3.1: Schematic of a thin plate with a hole and the three possible modes of motion

translation and angular velocities $U_3(t), \omega_1(t), \omega_2(t)$ respectively (Figure 3.1). The three resulting potentials $\overline{\phi}_i$, where $i \in \{3, 4, 5\}$ for the three respective modes, can then be normalized as:

$$\phi_3 = \frac{\overline{\phi}_3}{U_3 a}, \tag{3.1}$$

$$\phi_4 = \frac{\overline{\phi}_4}{\omega_1 a^2}, \tag{3.2}$$

$$\phi_5 = \frac{\overline{\phi}_5}{\omega_2 a^2}, \tag{3.3}$$

for some plate characteristic length a. These will be governed by Laplace's equation:

$$\nabla^2 \phi_i = 0. \tag{3.4}$$

Since the domain is infinite and we do not consider any free surface, the potential must also diminish to zero at infinity so that the problem can be formulated as a boundary integral equation as explained in the thesis introduction (equation (1.27)):

$$4\pi \frac{\partial \phi_i(P)}{\partial n_P} = \int_S \left([\phi_i(Q)] \frac{\partial^2 G(P,Q)}{\partial n_P \partial n_Q} \right) dS_Q. \tag{3.5}$$

Here S is the surface of one side of the thin plate considered to lie in the horizontal plane (as in figure 3.1), $[\phi_i]$ is the potential drop across the plate surface and the Green function

for this problem is the simple Rankine source:

$$G = \frac{1}{R_{PQ}}, \tag{3.6}$$

where again R_{PQ} is the distance between points P and Q. The normal vectors point in the z direction. The kernel function can be written explicitly as:

$$\frac{\partial^2 G}{\partial z \partial \zeta} = -\frac{1}{R^3} + 3\frac{(z-\zeta)^2}{R^5}. \tag{3.7}$$

Now since integration is only in the horizontal plane, $z = \zeta = 0$ and the kernel simplifies to:

$$\frac{\partial^2 G}{\partial z \partial \zeta} = -\frac{1}{R^3}, \tag{3.8}$$

and the equation to solve for is:

$$4\pi \frac{\partial \phi_i(P)}{\partial n_P} = -\int_S \left([\phi_i(Q)] \frac{1}{R_{PQ}^3} \right) dS_Q. \tag{3.9}$$

The left side of the equation is determined by the type of problem being solved:

$$\frac{\partial \phi_i(P)}{\partial n_P} = \begin{cases} n_3 = 1, (i = 3) \\ n_4 = y - y_0, (i = 4) \\ n_5 = x - x_0, (i = 5) \end{cases} \tag{3.10}$$

Here x_0 and y_0 are the centers of rotation for pitch and roll respectively. The other modes of motion are irrelevant for flat plates.

3.3 The Numerical Procedure

The problem formulation above seems to allude to the simplicity of this problem, but in practice, performing the integrals required in (3.9) is a daunting task that requires a careful treatment of the hypersingular part (see [54] for example). It is possible to solve the problem in the usual manner using a collocation scheme. However, we found that many triangular panels were required to obtain accurate results using that approach when a first order scheme is used.

In this work, we adopt a Galerkin approach as that was found to be more accurate and yet maintains its simplicity. The integrals required by both approaches are similar and can be used interchangeably. The Galerkin approach requires an additional integral which would make computing the influence coefficients more demanding but it does present some advantages. For instance, the size of the resulting system of equations is much smaller as we will see and the system will be symmetric. An efficient method to deal with hypersingular

kernels using a Galerkin approach in three dimensions has been given in [55]. The reference also presents a good summary of the different approaches to this problem.

We prefer a simpler approach. To solve this problem, we first approximate the potential jump $[\phi_i]$ using Chebychev polynomials of the first kind:

$$[\phi_i] = \sum_{n=0}^{\infty} \sum_{m=0}^{\infty} A^i_{mn} T_m(x) T_n(y), \tag{3.11}$$

where the Chebychev polynomials cross-product $F_{mn}(x, y) = T_m(x)T_n(y)$ is defined by:

$$F_{mn}(x, y) = \cos(m \cos^{-1}(x)) \cos(n \cos^{-1}(y)). \tag{3.12}$$

A Galerkin approach to the integral equation then results in:

$$4\pi \int_S \frac{\partial \phi_i}{\partial n} F_{mn}(x, y) = - \sum_{p=0,q=0}^{\infty} A^i_{mn} \int_S \int_S \left(F_{mn}(x, y) F_{pq}(\xi, \eta) \frac{1}{R^3_{PQ}} \right) dS_Q dS_P. \tag{3.13}$$

This is a system of equations for the unknown coefficients A_{mn}. When this equation is repeated for every m and n, the system will be complete. Now, not only is this a tedious computation that requires a double integration over an arbitrary area of the plate, it also involves a hypersingular kernel as discussed earlier. The good news is that the number of equations is going to be small as a small number of Chebychev polynomials are enough to represent the smooth solution expected from potential flow for most bodies of interest.

Our approach to obtaining those integrals is simple. First, the surface of the plate is discretized into triangular elements. The potential representation proposed in equation (3.11) can then be substituted by its Taylor series expansion over the center of each triangle. This will make it possible to perform analytic integration over each triangle. The details are given in appendix E. Finally, Gaussian quadrature is used to perform the second integration. Note that Chebychev polynomials are only defined within the interval [-1,1] so any plate shape of interest must be scaled to fit that frame.

3.4 Symmetry and the Added Inertia Over Different Axes

It is common for plate shapes of interest to be symmetric about one or two axes. The heave potential jump across the plate will then be symmetric across that axis while the pitch or roll potential jump will be antisymmetric. It is therefore desired to take that into consideration to reduce the computational effort of the problem and obtain more accurate results.

The implementation of that is straight forward. If the potential was symmetric over some axis, all the asymmetric modes over that axis in equation (3.11) should be dropped out. Those are the odd modes. If the potential was asymmetric, the even modes are dropped.

Finally, the added mass $\overline{\mu}_{ij}$ for $i, j \in \{3, 4, 5\}$ can be computed by integrating the pressure over the side of the plate. Written in dimensionless form $\mu_{ij} = \frac{\overline{\mu_{ij}}}{\rho a^s}$ where ρ is the fluid density and $s = 3, 4$ or 5 for $ij \in \{33\}, \{34, 35, 43, 53\}$ or $\{44, 45, 54, 55\}$ respectively, it is given by:

$$\mu_{ij} = -\int_S [\phi_i] n_j dS. \tag{3.14}$$

Here, the length metrics are taken to be dimensionless (using a) as well.

Now the results presented here for the pitch and roll motion are taken about a particular axis of the plate. It might be the case that the results for a different axis are desired. A simple transformation derived here will allow using the current results for any axis. Suppose a new roll potential is solved for a new roll axis y_1. The new potential ϕ_4^s satisfies the Laplace equation as well as the boundary condition:

$$\frac{\partial \phi_4^s}{\partial n} = y - y_1 = (y - y_0) - d, \tag{3.15}$$

where $d = y_1 - y_0$ is the distance between axes. By superposition, we can then say that $\phi_4^s = \phi_4 - d\phi_3$. Furthermore, the new added mass is given by:

$$\mu_{44}^s = -\int_S [\phi_4^s](y - y_1) dS = -\int_S [\phi_4 - d\phi_3](y - y_0 - d) dS = \mu_{44} - d\mu_{43} - d\mu_{34} + d^2\mu_{33}. \tag{3.16}$$

Similarly, we can write:

$$\mu_{43}^s = \mu_{43} - d\mu_{33}, \tag{3.17}$$

$$\mu_{45}^s = -\int_S [\phi_4 - d\phi_3](x - x_0) dS = \mu_{45} - d\mu_{35}. \tag{3.18}$$

3.5 Added Mass of Some Common Plate Shapes

With regards to mesh generation for all the shapes presented here, we used the code provided by Professor Per-Olof Pearson which is described in [56]. The code itself is available online under the name "DistMesh". The code allows for a nonuniform distribution of the triangular elements and we used that to add more panels near the edges and hole edges of the plates.

To test the procedure presented here, we compared our results to those in the literature for a circular and square shaped plates. The results for the circle of radius 1 were given in [52] as $\mu_{33} = 8/3$ and $\mu_{44} = 16/45$. These results were obtained by solving for the potential due to the motion of an ellipsoid and taking the limiting case where one dimension is zero. It is therefore possible to obtain closed form solutions in this particular case. Our numerical results were correct to 0.05% and 0.068% respectively using 2240 triangular panels and 14 even modes. Note that the result given for μ_{44} in page 393 of [52] has an additional π added by mistake as can be verified by rederiving the value of the added inertia using the potential given in the same reference. For the square-shaped plate, we used the result obtained

computationally (using Chebychev polynomials as basis functions) in [57], $\mu_{33} = 0.4547$, to which we had an error of 0.095% using 2196 triangular panels and 14 even modes. Note that the errors for other plates are expected to be higher especially when no symmetry exists and with more irregular shapes.

Figure 3.2 shows the plate shapes considered in this work with the parameter definitions. The parameter a is always used for normalization as before. Now for each shape, we used two meshes. For the circular plate without any holes, the first had 591 elements and the second 2240 and a similar ratio for the plates with increasing hole sizes. Note that these are only for the one quarter of the circle needed for the computation with symmetry around two axes. Figure 3.3 shows the percentage difference between results from the two meshes as the number of modes $n = m$ is increased. The results show that the error between meshes is less than one percent when more than 10 modes are used. This is true for all cases considered with different hole sizes. All results presented in this work used a largest mode $m = n = 26$ and a mesh size between 2000 and 3200 panels for the part of the geometry where compuation is performed afer taking symmetry into account.

In what follows, we present the computational results obtained for the added mass of the plates in figure 3.2.

3.5.1 Added Mass of a Circular Plate With a Center Hole

The first shape we present is the circular plate with a concentric hole. Figures 3.4 and 3.5 show the potential drop across the plate in heave and roll respectively. Notice how the potential drop decreases to zero around the edges so that the potential becomes continuous again outside the plate. This is a common characteristic of all the shapes we will show here.

Figures 3.6 and 3.7 show the added mass and inertia in heave and roll respectively as a function of hole radius to circle radius ratio. This is labeled as the numerical solution. The figures also show the result obtained if we simply subtract the added mass or inertia of the inner circle from the outer one as an approximation. Clearly the difference between the numerical solution and this algebraic one is substantial. In addition and as expected, the added load decreases as the hole size increases as there is less structure to push the fluid. The results for roll are taken about the x-axis but any other axis can be considered by using the transformation introduced in section 3.4. The other added loads are zero for this symmetric shape.

3.5.2 Added Mass of a Square Plate With a Center Hole

The second shape we present is the square plate with a concentric hole. Figures 3.8 and 3.9 show the potential drop across the plate in heave and roll respectively. Figures 3.10 and 3.11 show the added mass and inertia in heave and roll respectively as a function of hole radius to square side ratio. The algebraic solution is also shown for this case confirming our previous observation that this approximation returns poor results. Although the added load decreases as the hole size increases, it is interesting to see how different shapes of the

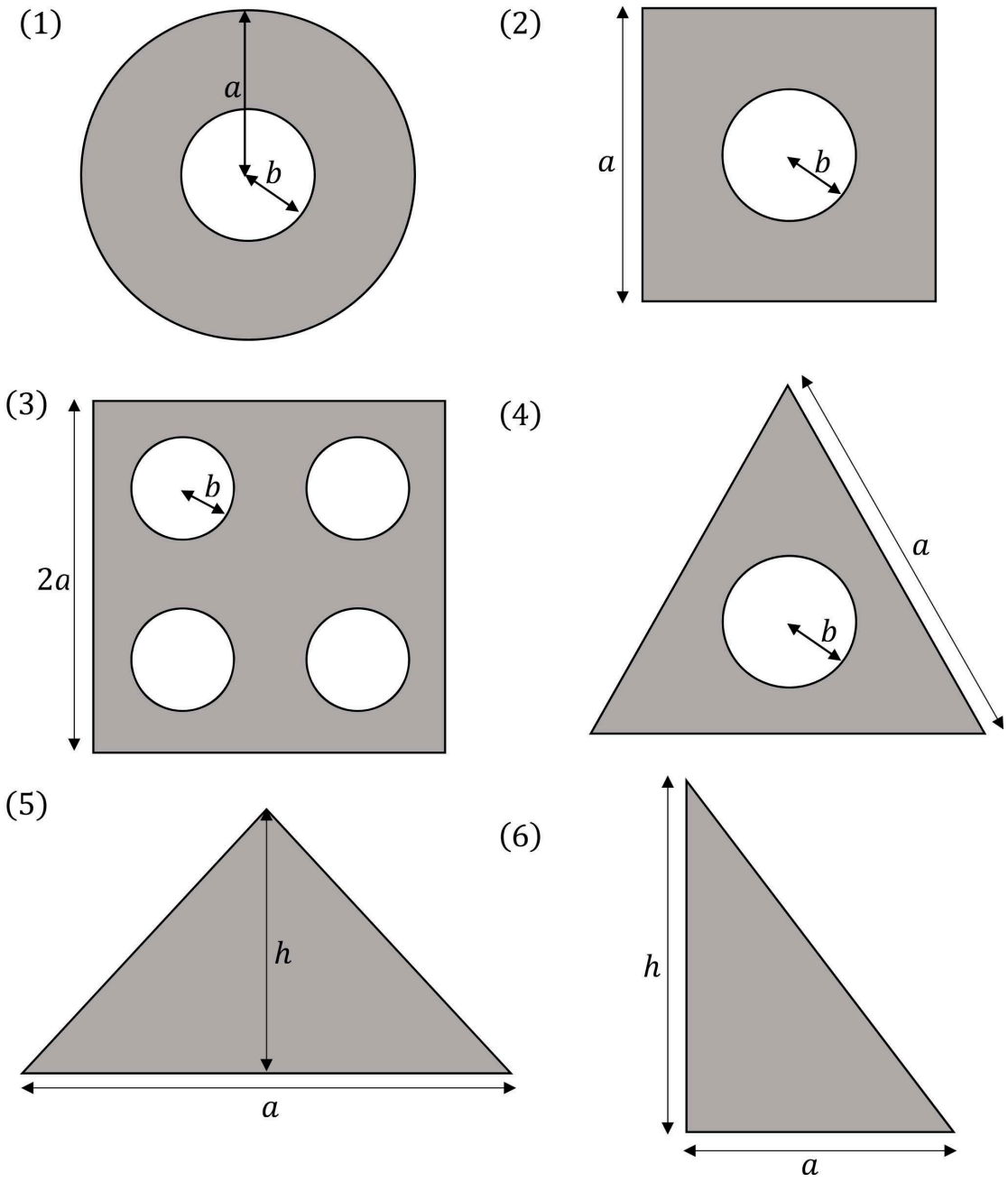

Figure 3.2: The different plate shapes considered: (1) circle with a hole, (2) square with a hole, (3) Square with 4 holes, (4) equilateral triangle with a hole, (5) isosceles triangle, (6) right triangle

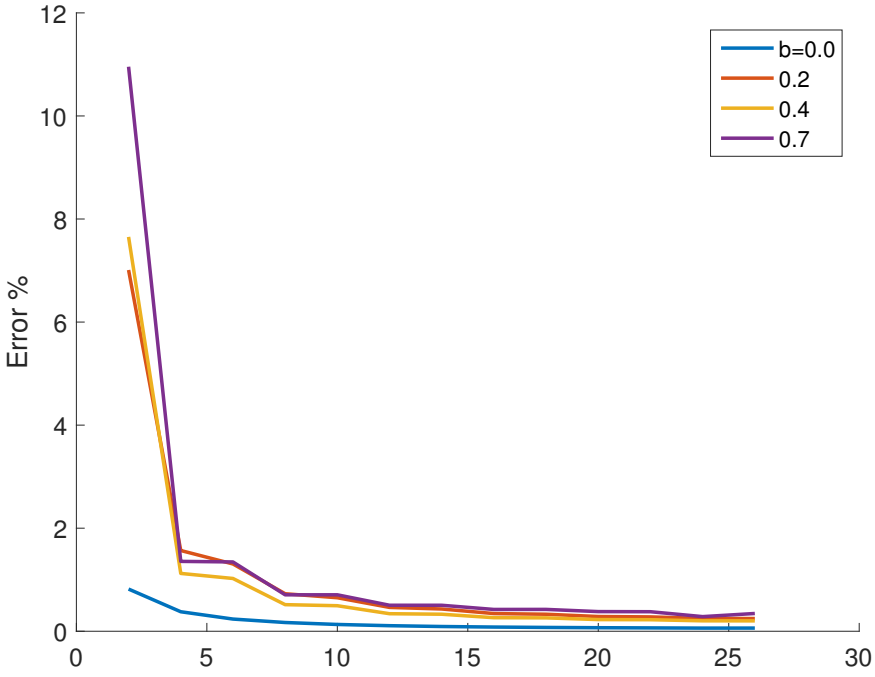

Figure 3.3: Percent error difference between coarse and fine meshes for a circle with different hole sizes as a function of max mode used ($a = 1$)

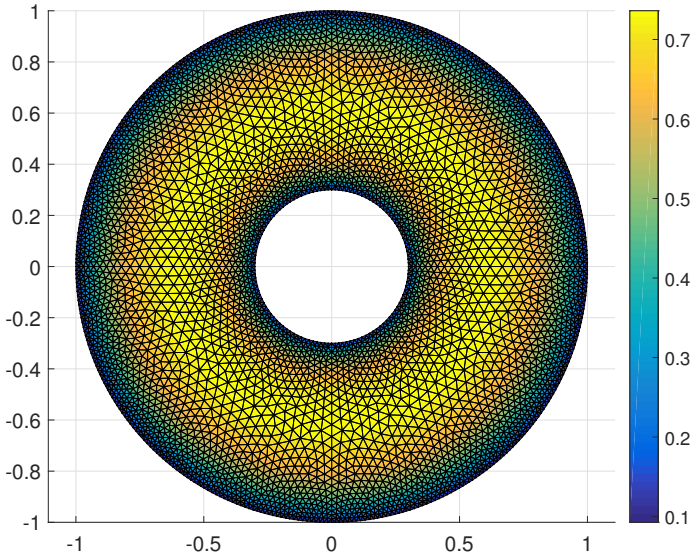

Figure 3.4: Potential drop across circular plate with a hole in heave ($b/a = 0.3$)

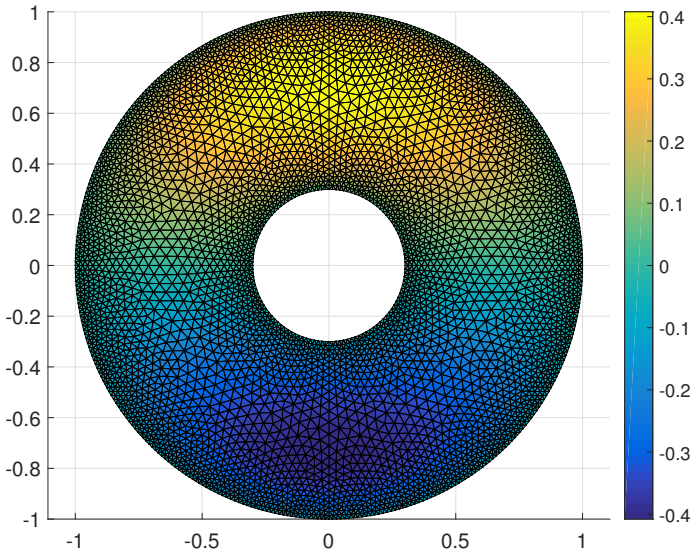

Figure 3.5: Potential drop across circular plate with a hole in roll ($b/a = 0.3$)

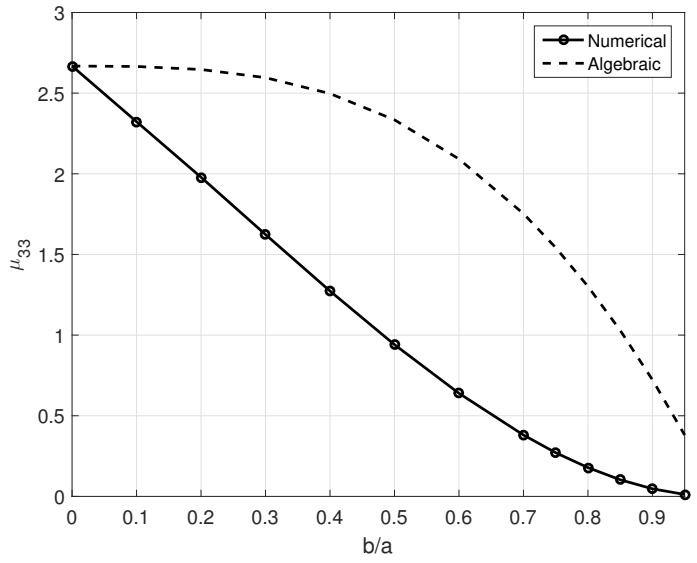

Figure 3.6: Added mass of a circular plate with a hole in heave as a function of varying hole size

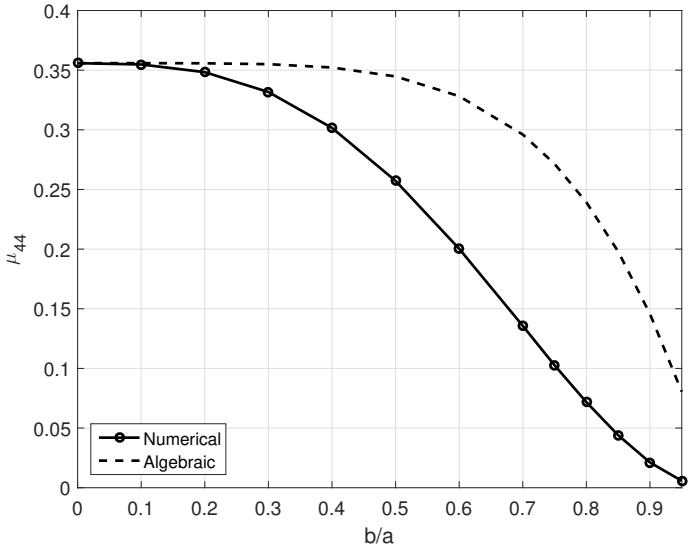

Figure 3.7: Added inertia of a circular plate with a hole in roll as a function of varying hole size

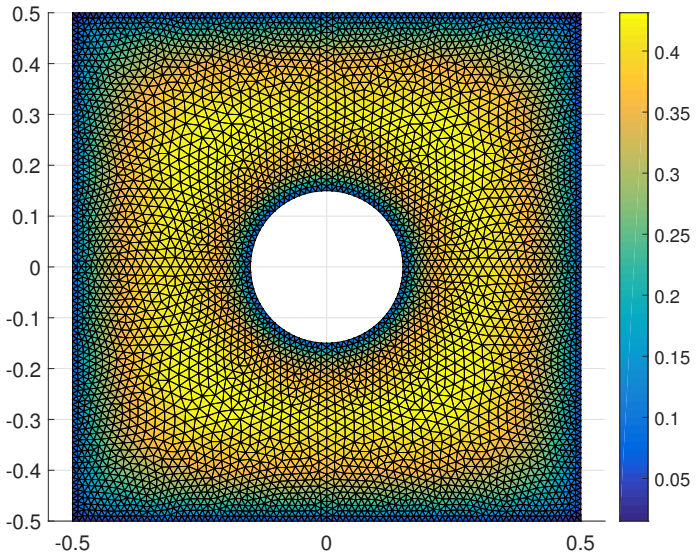

Figure 3.8: Potential drop across square plate with a hole in heave ($b/a = 0.15$)

same area compare in terms of their added mass. It turns out that the circle is slightly more efficient in moving mass than the square of the same area. This only applies when no hole is present. A completely different situation results with the holes present depending on the size of the holes.

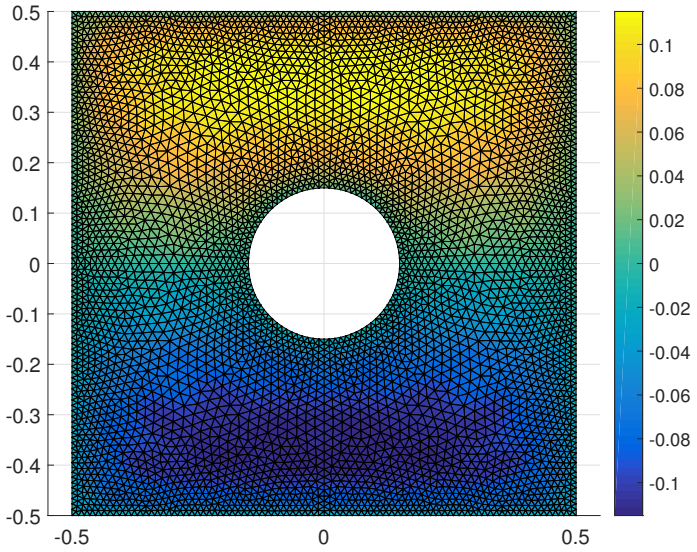

Figure 3.9: Potential drop across square plate with a hole in roll ($b/a = 0.15$)

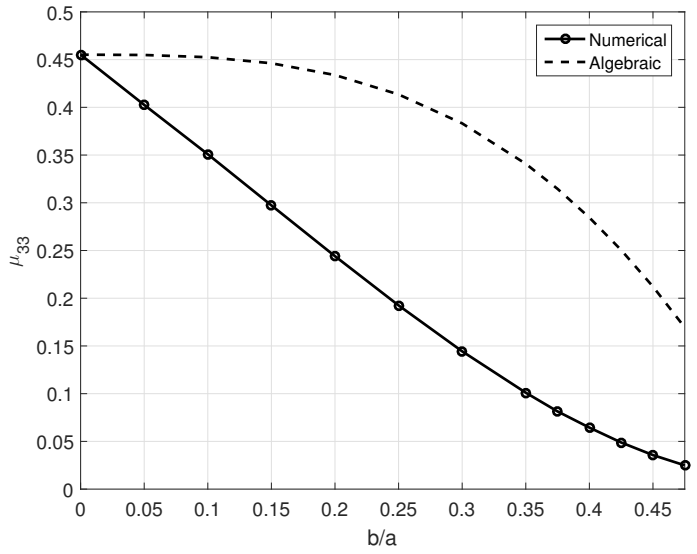

Figure 3.10: Added mass of a square plate with a hole in heave as a function of varying hole size

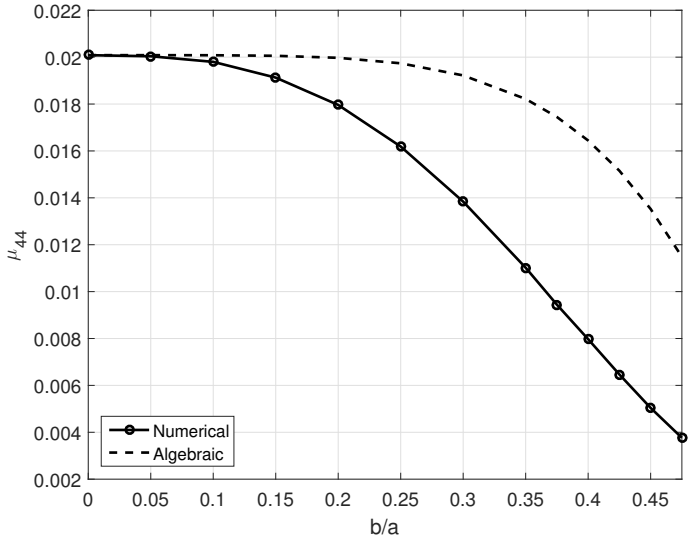

Figure 3.11: Added inertia of a square plate with a hole in roll as a function of varying hole size

3.5.3 Added Mass of a Square Plate With a 4 Holes at the Quadrant Centers

The next shape we present is a square plate with 4 equal size holes centered at the 4 quadrants of the square. Figures 3.12 and 3.13 show the potential drop across the plate in heave and roll respectively. Figures 3.14 and 3.15 show the added mass and inertia in heave and roll respectively as a function of hole radius to square side ratio. The algebraic solution is also shown for this case also showing poor results.

3.5.4 Added Mass of an Equilateral Triangle With a Hole at its Centroid

Next we present the results for an equilateral triangle with a hole centered at its centroid. Figures 3.16, 3.17 and 3.18 show the potential drop across the plate in heave, roll and pitch respectively. Figures 3.19, 3.20, 3.21 and 3.22 show the added mass and inertia across all modes that are nonzero as a function of hole radius b to triangle side length a ratio. In this case, symmetry is broken over the x-axis and this results in correlation between the heave and roll motions. The algebraic approximation is also shown as described earlier. In this case, since we only have the added inertia in roll of the circle over an axis passing through its center (Figure 3.7), it needs to be computed by shifting the axis of rotation as described in equation 3.16. The correlation terms in equation 3.16 are zero for a circle and the added mass $\mu_3 3$ was given in figure 3.6.

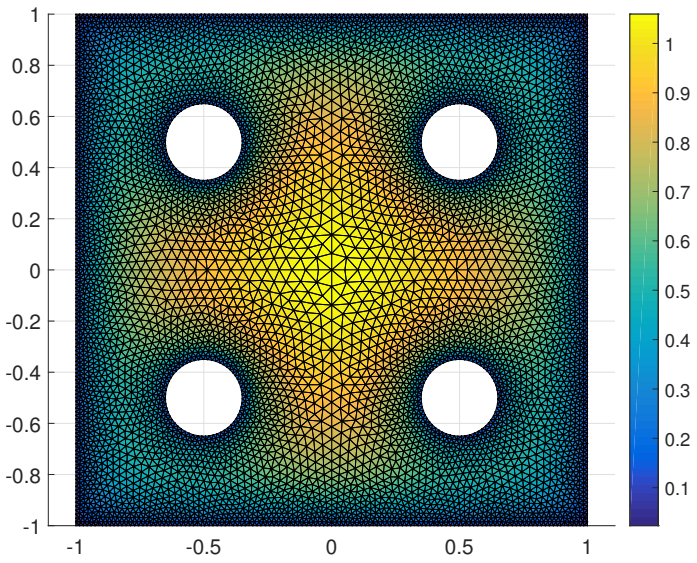

Figure 3.12: Potential drop across square plate with 4 holes in heave ($b/a = 0.15$)

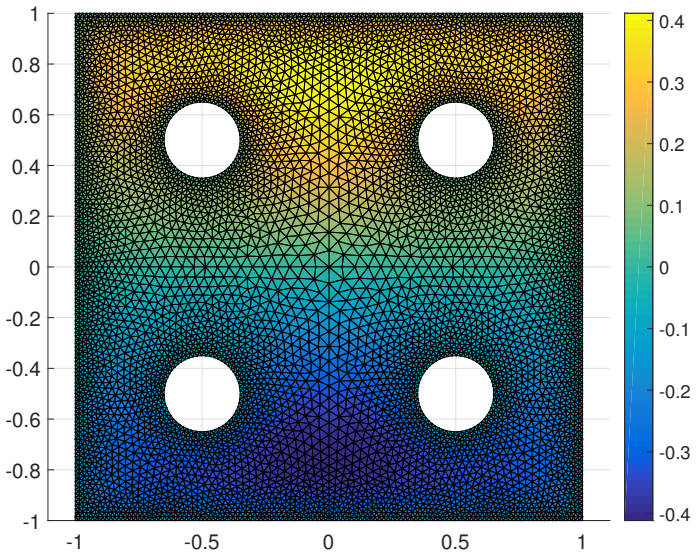

Figure 3.13: Potential drop across square plate with 4 holes in roll ($b/a = 0.15$)

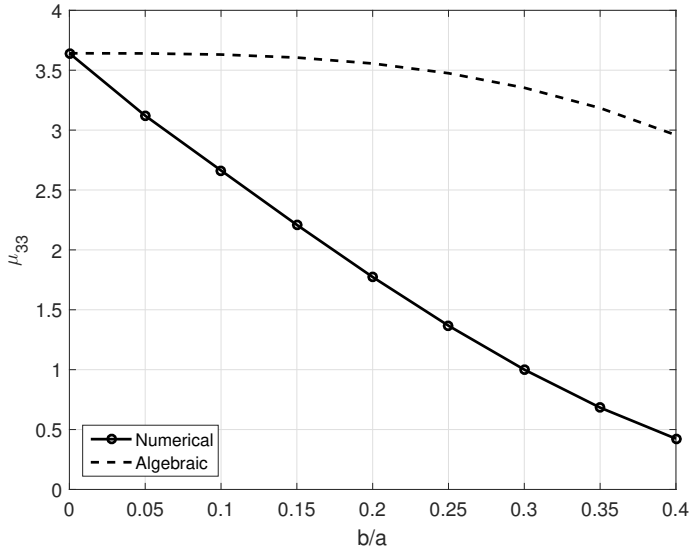

Figure 3.14: Added mass of a square plate with 4 holes in heave as a function of varying hole size

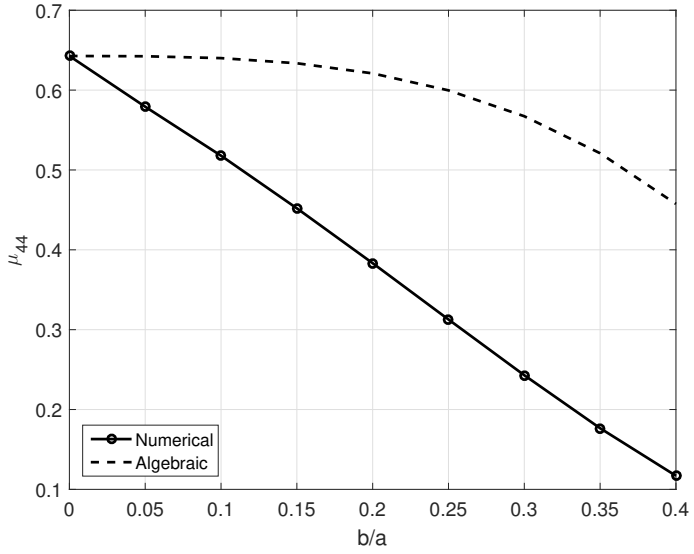

Figure 3.15: Added inertia of a square plate with 4 holes in roll as a function of varying hole size

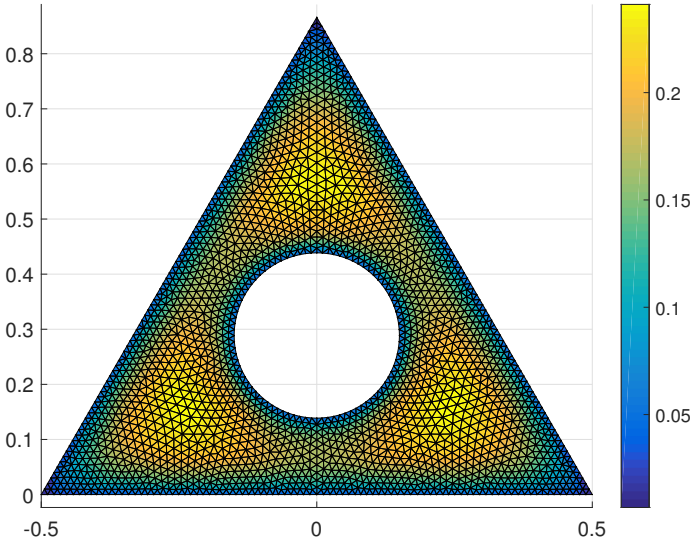

Figure 3.16: Potential drop across an equilateral triangular plate with a hole in heave ($b/a = 0.15$)

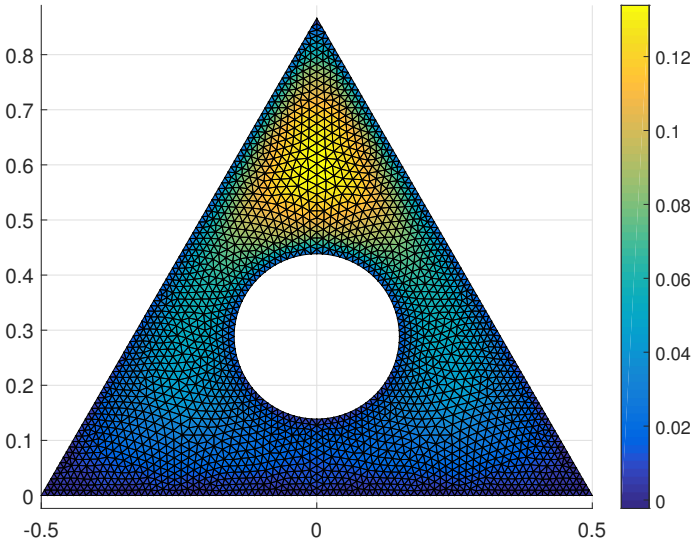

Figure 3.17: Potential drop across an equilateral triangular plate with a hole in roll ($b/a = 0.15$)

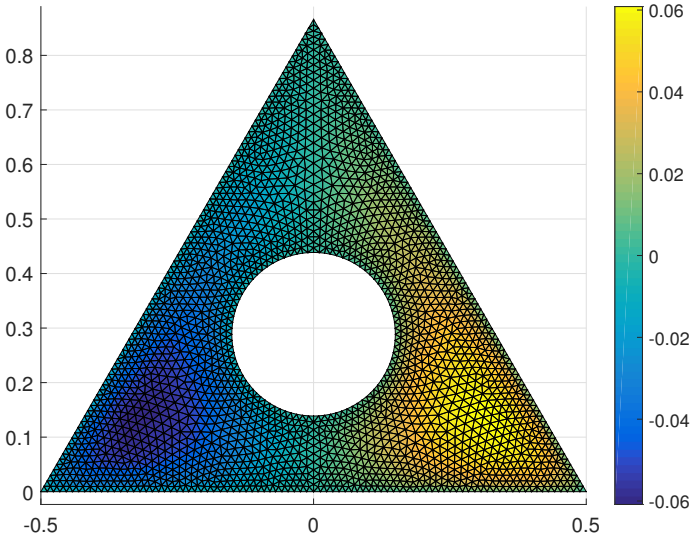

Figure 3.18: Potential drop across an equilateral triangular plate with a hole in pitch ($b/a = 0.15$)

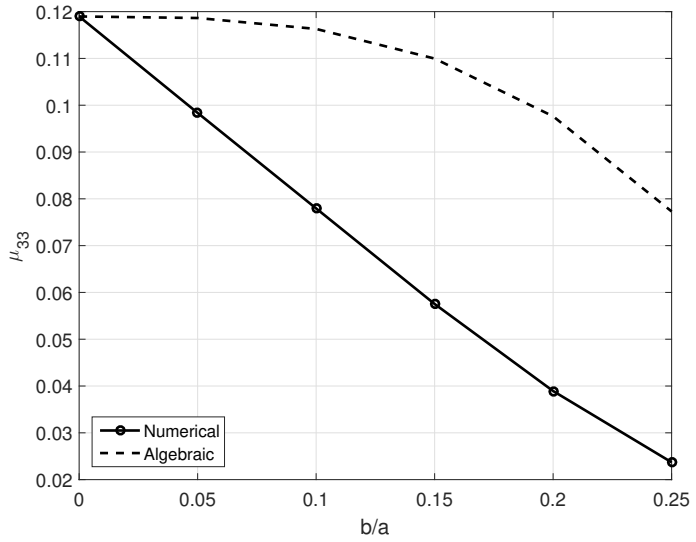

Figure 3.19: Added mass of an equilateral triangular plate with a hole in heave as a function of varying hole size

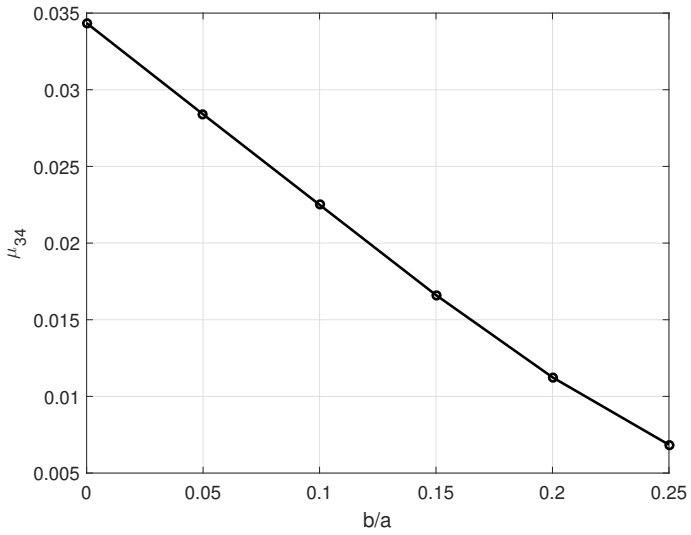

Figure 3.20: Heave-roll coupling added inertia of an equilateral triangular plate with a hole as a function of varying hole size

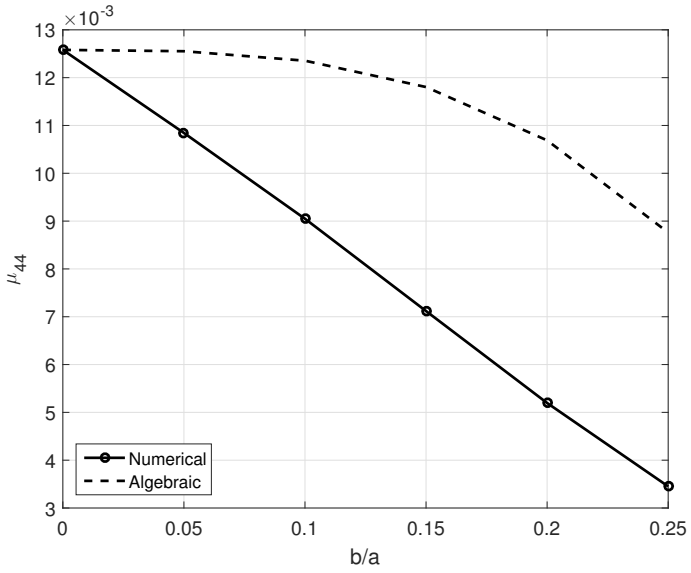

Figure 3.21: Added inertia of an equilateral triangular plate with a hole in roll as a function of varying hole size

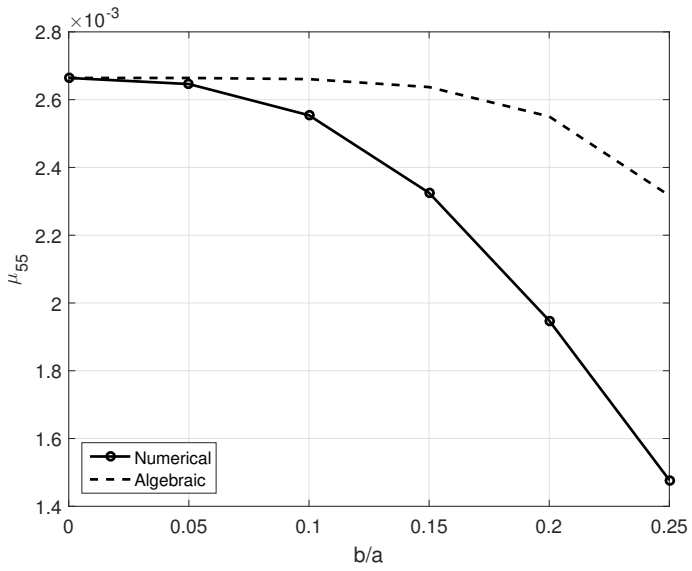

Figure 3.22: Added inertia of an equilateral tringular plate with a hole in pitch as a function of varying hole size

3.5.5 Added Mass of an Isosceles Triangle With Variable Height

Next we present the results for an isosceles triangle with a variable height. Figures 3.23, 3.24 and 3.25 show the potential drop across the plate in heave, roll and pitch respectively. Figures 3.26, 3.27 and 3.28 show the added mass and inertia across all modes that are nonzero as a function of triangle height h to triangle base length a ratio. In this case as well, symmetry is broken over the x-axis and this results in correlation between the heave and roll motions.

3.5.6 Added Mass of a Right Triangle With Variable Height

In the last part, we present the results for an isosceles triangle with a variable height. Figures 3.29, 3.30 and 3.31 show the potential drop across the plate in heave, roll and pitch respectively. Figures 3.32, 3.33 and 3.34 show the added mass and inertia across all modes that are nonzero as a function of triangle height h to triangle base length a ratio. In this case, no symmetry exists and all modes of motion need to be considered.

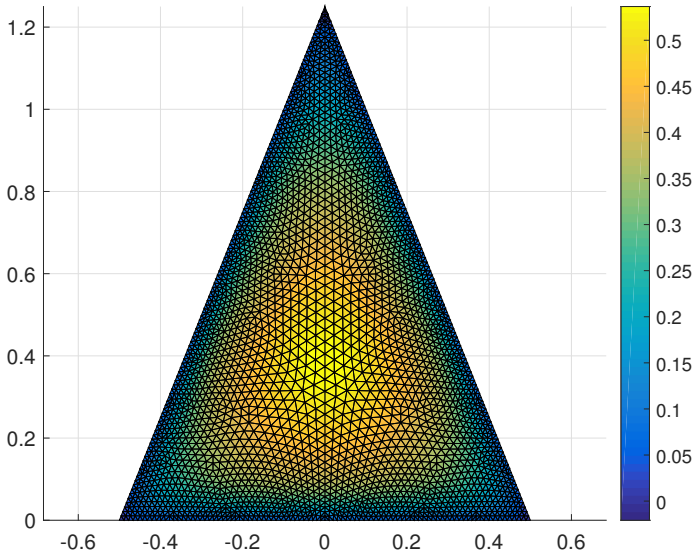

Figure 3.23: Potential drop across an isosceles triangular plate in heave ($h/a = 1.25$)

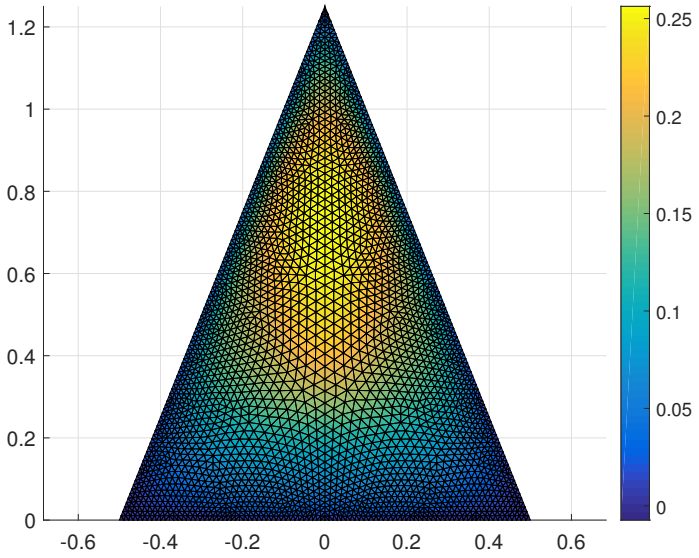

Figure 3.24: Potential drop across an isosceles triangular plate in roll ($h/a = 1.25$)

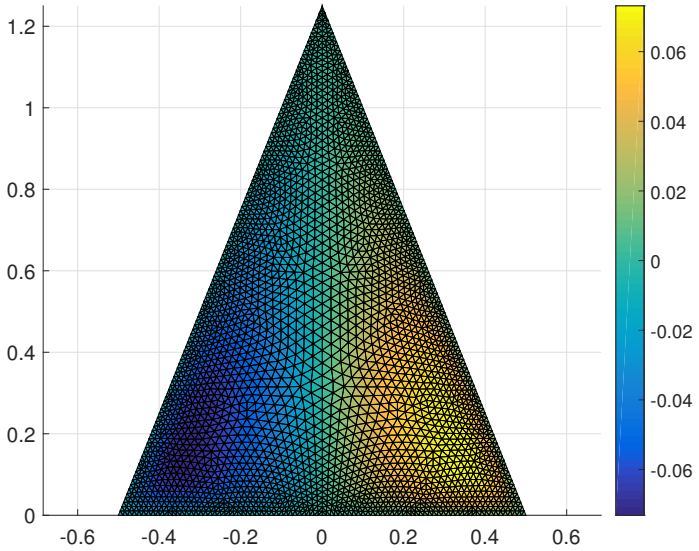

Figure 3.25: Potential drop across an isosceles triangular plate in pitch ($h/a = 1.25$)

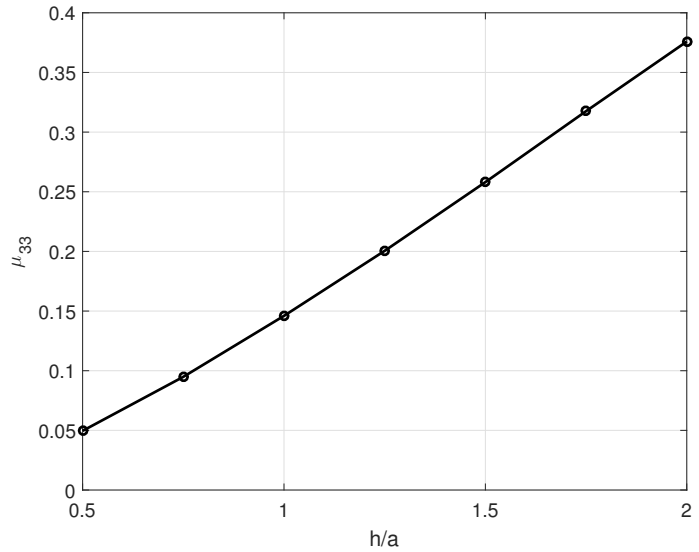

Figure 3.26: Added mass of an isosceles triangular plate in heave as a function of varying height

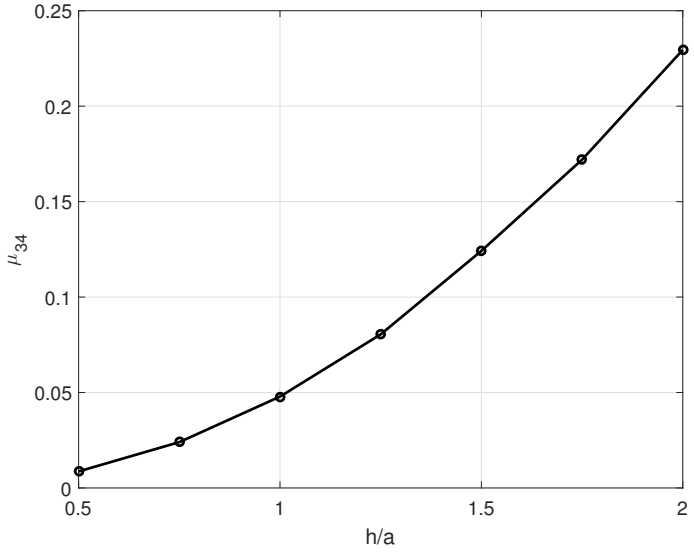

Figure 3.27: Heave-roll coupling added inertia of an isosceles triangular plate as a function of varying height

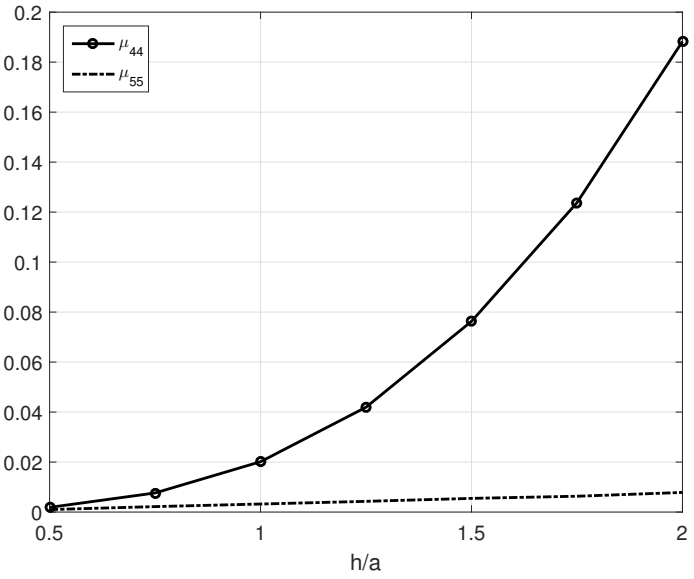

Figure 3.28: Added inertia of an isosceles triangular plate in roll and pitch as a function of varying height

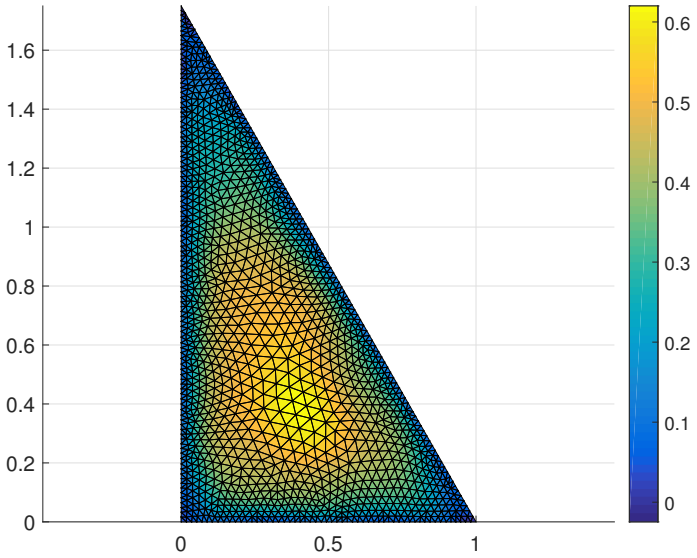

Figure 3.29: Potential drop across a right triangular plate in heave ($h/a = 0.175$)

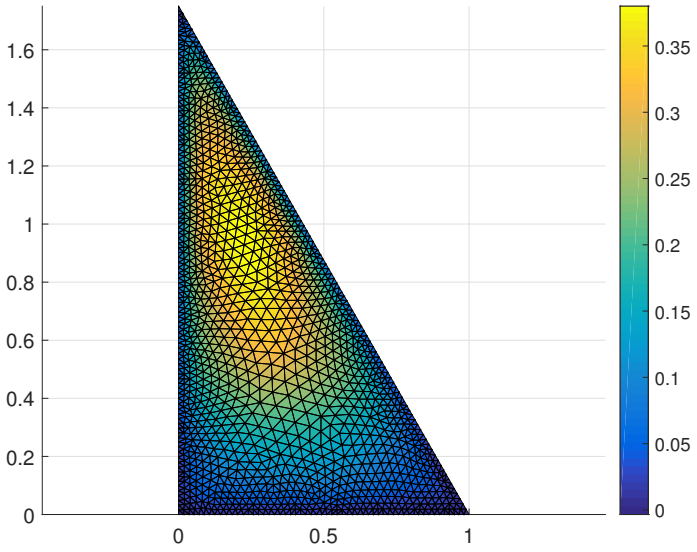

Figure 3.30: Potential drop across a right triangular plate in roll ($h/a = 0.175$)

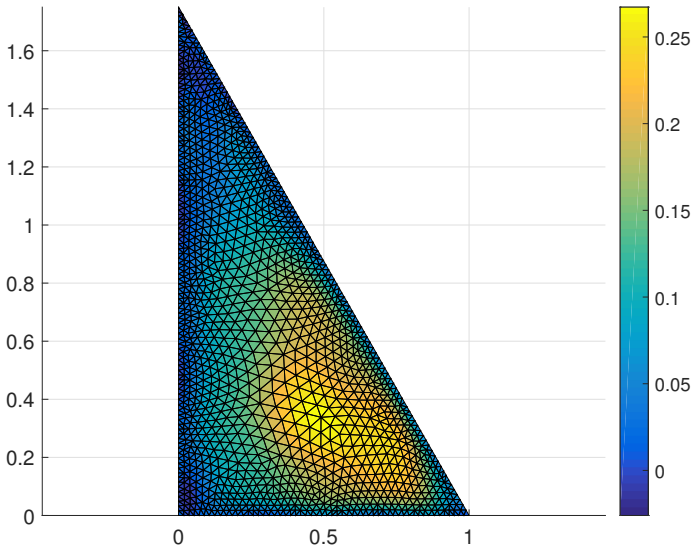

Figure 3.31: Potential drop across a right triangular plate in pitch ($h/a = 0.175$)

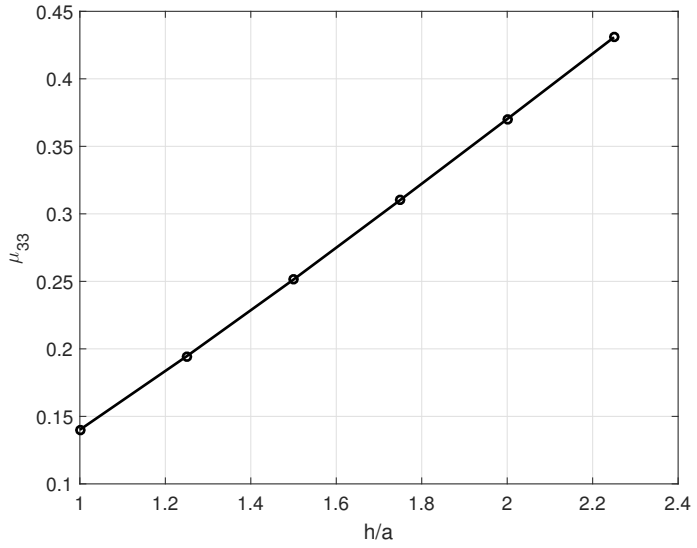

Figure 3.32: Added mass of a right triangular plate in heave as a function of varying height

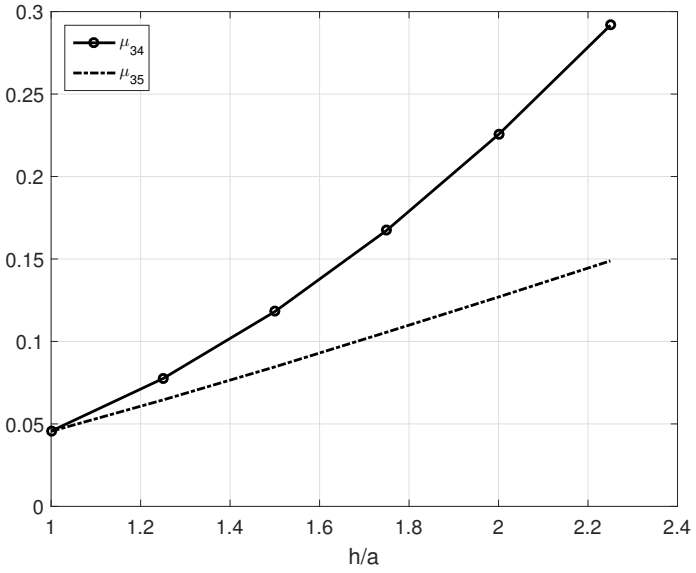

Figure 3.33: Heave-roll and heave-pitch coupling added inertia of a right triangular plate as a function of varying height

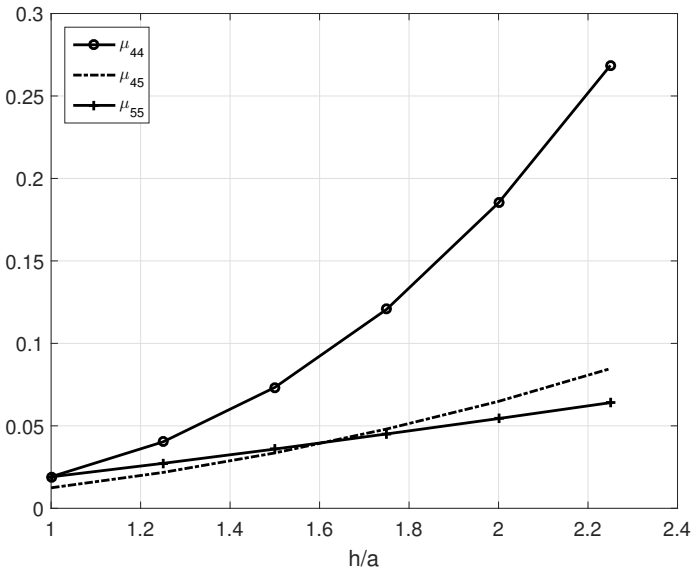

Figure 3.34: Added inertia in roll and pitch and roll-pitch coupling inertia of a right triangular plate as a function of varying height

Chapter 4

A Fast Multipole Method for the Three Dimensional Linear Water-Wave/Structure Interaction Problem with Arbitrary Bottom Topography

4.1 Introduction

The solution of the problem of linear water-wave interaction with floating structures is an important one since it is applied in all kinds of ocean related activities, ranging from the design of ships and offshore structures to shore protection and recreational activities. The ocean bottom topography can be important in the design of these structures and accordingly many researchers provided means of including its effects in the solution procedure. Most notably, the authors in [58] developed two hybrid methods to treat the problem. The first splits the computational domain into an inner region in which the solution is modeled using finite elements while matching the more simplistic outer domain in which eigenfunctions are used. The second method uses simple source free-space integral equations for the inner domain and the radiation condition is applied directly to the boundary at a finite distance from the body of interest. Both methods allow for arbitrary bottom topography in the inner region. Later, Yeung [59] introduced an updated method which matches the inner potential, governed by the simple source integral equation, to an outer potential that is represented with the natural eigenfunction solutions of the outer domain. His work was restricted to two dimensions though. Reference [60] extended the latter's work to three dimensions while in [61] a more elaborate and accurate method for the same problem was presented. In this work, we make use of this last approach as a starting point to our solution procedure which is able to handle a much larger numbers of unknowns. Additional work on these hybrid methods include that in [62] which solved for the steady state wave-resistance problem, that in [63] which presented a way to use the first-order solution presented here to obtain the second-order loads on floating structures, and the work in [64] which allowed for a water depth that varies with direction although with much more work, both of which inspire possible extensions for the work presented here. In addition, a method for matching an inviscid exterior domain to a viscous interior one was presented in [65].

Often times in practical situations, it is required to solve for a large number of unknowns. The design of Very Large Floating Structures (VLFS) is one important example and unknowns beyond the scope of capabilities of traditional methods are sometimes needed [66]. In addition, the simulation of the interaction of large numbers of bodies such as in a wave energy farm, requires significant computational effort, particularly if the bodies are in

close proximity to each other. For example, the method used in [67], which makes use of the far-field behavior cannot be used. In addition, commonly used methods such as interaction theory [68] have limitations such as the requirement of constant water depth and only apply to bodies that are not vertically overlapping. In addition, achieving satisfactory accuracy requires ever more terms as the bodies come closer to each other. The fact that these methods scale at best as $O(M^2)$ where M is the number of bodies is a further limitation for large arrays. Other methods that have been used include the preconditioned Fast Fourier Transform (pFFT) which is a hierarchical iterative method [69]. The pFFT is usually chosen because of its ability to handle the free-surface Green function which is the usual Green function used in modeling these problems. The algorithm provides an $O(Nlog(N))$ efficiency in speed and memory and has been used successfully to model large scale problems of interest [70]. The authors noted that using this method (included in FastWAMIT), up to 100,000 elements could be easily used and in fact they showed results for 87,040. The algorithm is restricted to the use of uniform grids because of its dependency on the FFT and has not been used to model variable bathymetry. For a brief review of methods used for multiple body interactions see [71].

Instead of using the pFFT, we make use of the fact that the hybrid method depends on the simple source and is, therefore, amenable to the application of the Fast Multipole Method (FMM). The FMM was first introduced in [15] for the simulation of the interaction of a large number of particles. It is a hierarchical scheme based on the idea that groups of particles farther away from a target particle can be grouped together and their effects combined into a single expression. This reduced the computational complexity of the problem from $\mathrm{O}(N^2)$ to $\mathrm{O}(N)$ and memory usage to $O(N)$ where N is the number of particles. This was indeed used in [17] for the discrete element method. For boundary element methods, the interactions between panels can be treated as interactions between sheets of particles and therefore can be simulated using the FMM. This requires that an iterative solver be used if the unknown values are to be found. The FMM can be applied to algorithms that depend on the free-surface Green function as well [72]. However, the present method is not as heavily dependent on the use of transcendental functions and can therefore be made more efficient.

In what follows, we will describe the use of the FMM for the hybrid method and present examples of its usage to treat problems that require a high number of panels or that have complicated ocean floor topography. This work is to be submitted for publication soon [73].

4.2 The Hybrid Method

In this section, we will provide a summary of the hybrid method used without acceleration. This follows closely the work in [61] with the exception that we use triangular panels rather than the quadrilateral ones used there.

Consider a coordinate system situated at some point on the free surface and the z-axis pointing upwards as shown in figure 4.1. The figure also shows the body surface S_B, the free

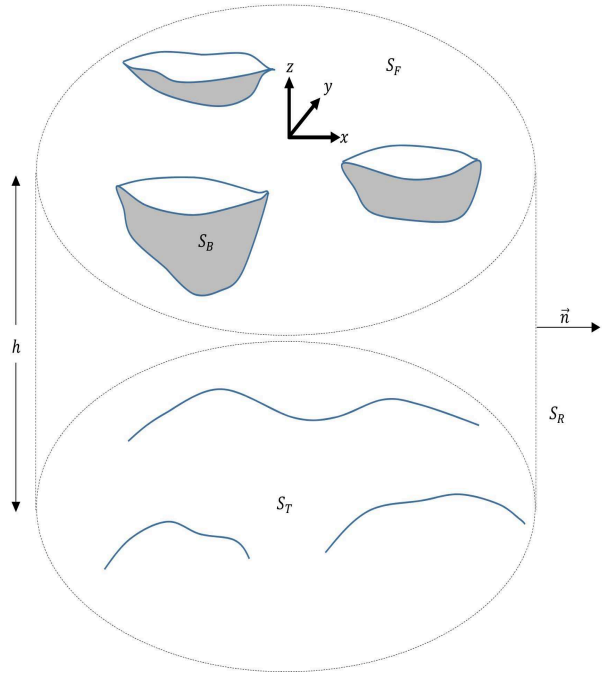

Figure 4.1: Schematic of the problem domain and parameter definitions

surface S_F, the bottom topography surface S_T, the radiation boundary S_R and the normal vector pointing out of these surfaces. Assume the flow can be represented by a time harmonic potential $\Phi_j(x, y, z, t) = Re\{\overline{\phi}_j(x, y, z)e^{-i\omega t}\}$ where ω represents the angular frequency of the harmonic motion, j is the mode of motion and $i = \sqrt{-1}$. In this work, we use the notation that an overbar represents dimensional variables.

4.2.1 The Radiation Problem Formulation

We start with the radiation problem. That is, when one of the bodies oscillates at some frequency ω in a given direction. Define the dimensionless radiation velocity potential $\phi_j = \overline{\phi}_j/a^l U_j$ where a is a problem characteristic length and U_j is the translation or angular velocity for the jth mode of motion. The integer l is 1 for the translation modes and 2 for the rotational ones. Henceforth, a is used to make all length parameters dimensionless. The

problem then is that of linear water wave theory:

$$\nabla^2\phi_j = 0, \tag{4.1}$$

$$\frac{\partial\phi_j}{\partial z} - \nu\phi_j = 0, \quad z = 0 \tag{4.2}$$

$$\frac{\partial\phi_j}{\partial n} = 0, \quad z = -h(x,y) \tag{4.3}$$

$$\frac{\partial\phi_j}{\partial n} = f_j(S_b). \quad P(x,y,z) \in S_b \tag{4.4}$$

$$\frac{\partial\phi_j}{\partial n} = 0. \quad P(x,y,z) \in (S_B - S_b) \tag{4.5}$$

Here, P is a point of interest, and ϕ_j results from the motion of the body or bodies S_b with a unit normal velocity or angular velocity of f_j and $j \in [1,6]$ for surge, sway, heave, roll, pitch and yaw respectively. In addition, $h(x,y)$ is the variable water depth which defines the bathymetry. The parameter $\nu = \omega^2 a/g$, where g is the gravitational acceleration, relates the frequency to the wavenumber k by $\nu = k\tanh(kh)$. In addition, $f_j = n_j$ for $j \in [1,3]$ and $f_j = \left[\overrightarrow{R} \times \overrightarrow{n}\right]_j$ for $j \in [4,6]$ where $\overrightarrow{R}$ is the distance from the center of rotation and $\overrightarrow{n}$ is the normal vector. A radiation condition which dictates outgoing waves at infinity is also required.

4.2.2 The Scattering Problem Formulation

The scattering (or diffraction) problem can be formulated in a similar manner. First define the dimensionless scattering velocity potential $\phi_S = \overline{\phi}_S/\eta_0\sqrt{ga}$ where η_0 is the wave amplitude of the incident wave. Consider the scattered potential governing equations:

$$\nabla^2\phi_S = 0, \tag{4.6}$$

$$\frac{\partial\phi_S}{\partial z} - \nu\phi_S = 0, \quad z = 0 \tag{4.7}$$

$$\frac{\partial\phi_S}{\partial n} = 0, \quad z = -h(x,y) \tag{4.8}$$

$$\frac{\partial\phi_S}{\partial n} = 0. \quad P(x,y,z) \in S_B \tag{4.9}$$

The driving force for this problem is the incident wave approaching from infinity. The incident wave potential for the flat bottom case is given by:

$$\overline{\phi}_0 = -\frac{ig\eta_0}{\omega}\frac{\cosh(k(z+h_0))}{\cosh(kh_0)}e^{ik(x\cos\alpha + y\sin\alpha)}. \tag{4.10}$$

Here α is the incident wave direction (see figure 4.5). The dimensionless incident potential is defined as $\phi_0 = \overline{\phi}_0/\eta_0\sqrt{ga}$. Again we use a to make all length parameters dimensionless.

Now assume that $h(x, y)$ is variable only within a restricted region $x^2 + y^2 < r_0^2$ for some given r_0 and is a constant h_0 otherwise. The idea here is to solve for each domain separately using a suitable method and then match the solution at the common boundary.

Now in the exterior domain, we can write $\phi_S = \phi_7 + \phi_0$ where ϕ_7 is the diffracted potential. This has the interpretation that the scattered potential is the sum of the incident wave and a correction term represented by the diffraction potential ϕ_7. This interpretation falls short in the interior domain since the incident potential given in (4.10) is not a valid solution for the interior region with variable topography. However, from an implementation standpoint, it is convenient to write $\phi_S = \phi_7 + \phi_0$ as that would make matching at the common boundary much simpler. This is acceptable though as, mathematically speaking, only the total potential ϕ_S needs to satisfy condition (4.8), not the individual components. Having that said, the equivalent problem for ϕ_7 can be solved instead:

$$\nabla^2 \phi_7 = 0, \tag{4.11}$$

$$\frac{\partial \phi_7}{\partial z} - \nu \phi_7 = 0, \quad z = 0 \tag{4.12}$$

$$\frac{\partial \phi_7}{\partial n} = -\frac{\partial \phi_0}{\partial n}, \quad z = -h(x, y) \tag{4.13}$$

$$\frac{\partial \phi_7}{\partial n} = -\frac{\partial \phi_0}{\partial n}. \quad P(x, y, z) \in S_B \tag{4.14}$$

These equations apply for both domains where needed. In addition, matching of the potentials and there normal derivatives resulting from the solutions of both domains is required at the common boundary S_R. ϕ_7 also has to satisfy a radiation condition dictating outgoing at infinity in the exterior domain.

4.2.3 The Solution Formulation

The solution proceeds by dividing the domain into two regions separated by a fictional cylindrical surface S_R defined by the boundary $x^2 + y^2 = r_0^2$. The solution for the external region will be represented by eigenfunction expansions relevant to that region ($j \in [1, 6] \cup [7]$):

$$\phi_j = \sum_{n=0}^{\infty} \sum_{m=0}^{\infty} (\alpha_{mn}^j \cos(n\theta) + \beta_{mn}^j \sin(n\theta)) \frac{H_n(K_m r)}{H_n(K_m r_0)} \frac{\cosh(K_m(z + h_0))}{\cosh(K_m h_0)}. \tag{4.15}$$

α_{mn}^j and β_{mn}^j are constants to be determined, H_n are the Hankel functions of the first kind and order n while r and θ are cylindrical coordinates in the horizontal plane. In addition, $K_0 = k$ and $K_m = ik_m$, where $\nu = -k_m \tan(k_m h)$.

Inside S_R, the problem is formulated into a boundary integral of the form:

$$2\pi \phi_j(P) = \int \int_S \left(\frac{\partial \phi_j}{\partial n}(Q) \left(\frac{1}{R_{PQ}} \right) - \phi_j(Q) \frac{\partial}{\partial n} \left(\frac{1}{R_{PQ}} \right) \right) dS(Q). \tag{4.16}$$

Here Q is an integration point on the full surface $S = S_B + S_F + S_T + S_R$. R_{PQ} is the distance between points P and Q. The solution of the inner region is the potential that satisfies equation (4.16). Now both the outer region solution and its normal derivative are substituted into equation (4.16) which is solved using the boundary element method.

4.3 The Numerical Procedure

In the original work of [61], the surface is discretized into quadrilateral panels and the potential is assumed constant over each panel. In this work though, we choose to use flat triangular panels as that will provide easier means of generating meshes and modeling complex geometry. The potential is still assumed constant over each panel. Now with the use of the boundary conditions (4.2), (4.3), and (4.5), discretization, and by choosing the collocation points P_p to be on the panel centroids, the problem is reduced to the solution of a system of linear equations:

$$\sum_{q=1}^{N_B} A_{pq}\phi_j(Q_q) + \sum_{q=N_B+1}^{N_B+N_F} (A_{pq} - \nu B_{pq})\,\phi_j(Q_q) + \sum_{q=N_B+N_F+1}^{N_B+N_F+N_T} A_{pq}\phi_j(Q_q) + \sum_{n=0}^{N_R}\sum_{m=0}^{M_R}(F_{pmn}\alpha_{mn}^j + G_{pmn}\beta_{mn}^j) = \sum_{q=1}^{N_B} B_{pq}f_j(Q_q). \quad (4.17)$$

Here we define

$$A_{pq} = \int_S \frac{\partial}{\partial n}\frac{1}{R_{PQ}}dS + 2\pi\delta_{pq}, \quad (4.18)$$

$$B_{pq} = \int_S \frac{1}{R_{PQ}}dS. \quad (4.19)$$

Integration is taken over the relevant triangular panel and δ_{pq} is the Kronecker delta. In addition

$$\begin{bmatrix} F_{pmn} \\ G_{pmn} \end{bmatrix} = \int_{S_R} \left[\frac{\partial}{\partial n}\frac{1}{R_{PQ}} - \frac{K_m H_n'(K_m r_0)}{H_n(K_m r_0)}\frac{1}{R_{PQ}}\right] \frac{\cosh(K_m(\zeta+h))}{\cosh(K_m h)} \begin{bmatrix} \cos(n\psi) \\ \sin(n\psi) \end{bmatrix} dS + 2\pi \frac{\cosh(K_m(z+h))}{\cosh(K_m h)} \begin{bmatrix} \cos(n\theta) \\ \sin(n\theta) \end{bmatrix} \delta_p, \quad (4.20)$$

where δ_p is 1 when p corresponds to a collocation point on S_R and 0 otherwise. The values N_B, N_F and N_T correspond to the number of panels used on S_B, S_F and S_T respectively while M_R and N_R are the truncation limits used for the infinite series in 4.15. The integration in equations 4.18 and 4.19 will only be required when computing the direct influences of panels on one another. Gaussian quadrature over a triangle could be used except when the

collocation point lies over the integration panel. In that case, and when the collocation point lies within the same plane as the panel in general, the integral in 4.19 is exactly zero while for that in 4.18, we refer the reader to appendix C for the details of the analytic method used. For (4.20), it is possible to perform the integration over the angular direction analytically as was shown in [61]. In appendix D, we present a brief description of that method also used in our work.

4.4 The Fast Multipole Method

The fact that the method just described uses the free-space Rankine source allows us to make use of the FMM to improve the efficiency of the method for larger number of unknowns. The FMM is a hierarchical scheme introduced in [15] and that makes use of the fact that the interaction between elements at large distances from each other can be adequately accounted for indirectly using multipole representations of the Rankine source. We provide a brief explanation of the method following closely the work in [74].

In the first step, the particles or panels are divided into cells in a hierarchical manner. An octree is used in three dimensions. This means that each cell is divided into eight smaller ones until the number of panels in each cell is less than a specified value. The lowest level cells are called the leaves of the tree. In this work, we adopt an adaptive scheme for the FMM. This means that cell division takes into account that different parts of the domain have different concentrations of panels and therefore will have different levels of divisions. This will make the method more efficient but will complicate the interactions between the cells. Figure 4.2 shows a mesh for a problem with four floating truncated cylinders while figure 4.3 shows the resulting octree for that mesh. Only the leaves are shown for clarity. One can clearly see from the figure that most cells are concentrated near the four cylinders where most panels are.

The second step is to calculate the moments for each cell. These are representations of the influence of all the panels in each cell without regard to the target cells. We use the fact that the Rankine source can be expanded into:

$$\frac{1}{R_{PQ}} = \sum_{a=0}^{\infty}\sum_{b=-a}^{b=a} S_{a,b}(P-Q_c)T_{a,b}(Q-Q_c), \qquad |Q-Q_c| < |P-Q_c|, \tag{4.21}$$

$$S_{a,b}(P) = (a-b)!P_a^b(\cos(\theta))e^{-ib\varphi}\frac{1}{r^{a+1}}, \tag{4.22}$$

$$T_{a,b}(P) = \frac{1}{(a+b)!}P_a^b(\cos(\theta))e^{ib\varphi}r^a, \tag{4.23}$$

where Q_c is a point chosen to be the cell center, (r,θ,φ) are spherical coordinates and P_a^b are the associated Legendre functions defined as:

$$P_a^b(x) = (1-x^2)^{b/2}\frac{d^b}{dx^b}P_a(x), \tag{4.24}$$

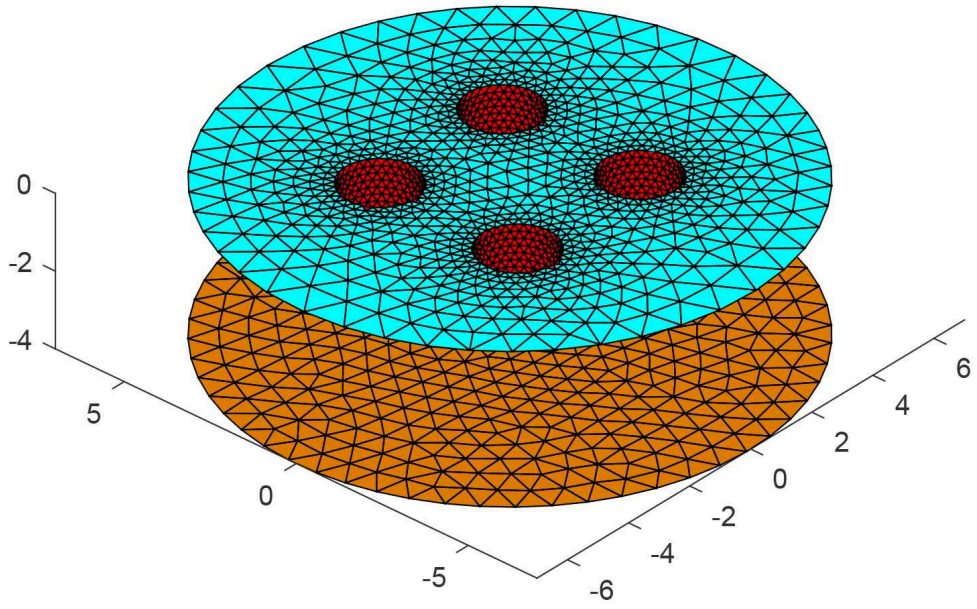

Figure 4.2: Small mesh for the four cylinder problem

and $P_a(x)$ is the Legendre polynomial of degree a. The moments are then calculated for all the leaves using the expressions:

$$M_{a,b}(Q_c) = \int_S \gamma(Q) T_{a,b}(Q - Q_c) dS(Q), \tag{4.25}$$

$$\overline{M_{a,b}} = \int_S \delta(Q) \frac{\partial T_{a,b}}{\partial n}(Q - Q_c) dS(Q). \tag{4.26}$$

Here γ and δ are the source and dipole strengths. In the final formulation of the problem, γ is the normal derivative of the potential and is known from the boundary conditions given in equations (4.2-4.5) while δ is the trial solution from the iterative solver for the potential itself on the surface (assumed constant on each panel). The total moment on each panel is a combination of $M_{a,b}$ and $\overline{M_{a,b}}$. For our problem, it is simply $\overline{M_{a,b}} - \nu M_{a,b}$ for the free surface panels (S_F) and $\overline{M_{a,b}}$ for panels on S_B and S_T.

After all the moments of the leaves are computed, the moments for the parent cells are obtained by first transferring the center of each of the child cells to their parents and then adding the contribution from each child cell. The center transformation known as the moment to moment translation (M2M) is given by:

$$M_{a,b}(Q'_c) = \sum_{a'=0}^{a} \sum_{b'=-a'}^{a'} T_{a',b'}(Q_c - Q'_c) M_{a-a',b-b'}(Q_c). \tag{4.27}$$

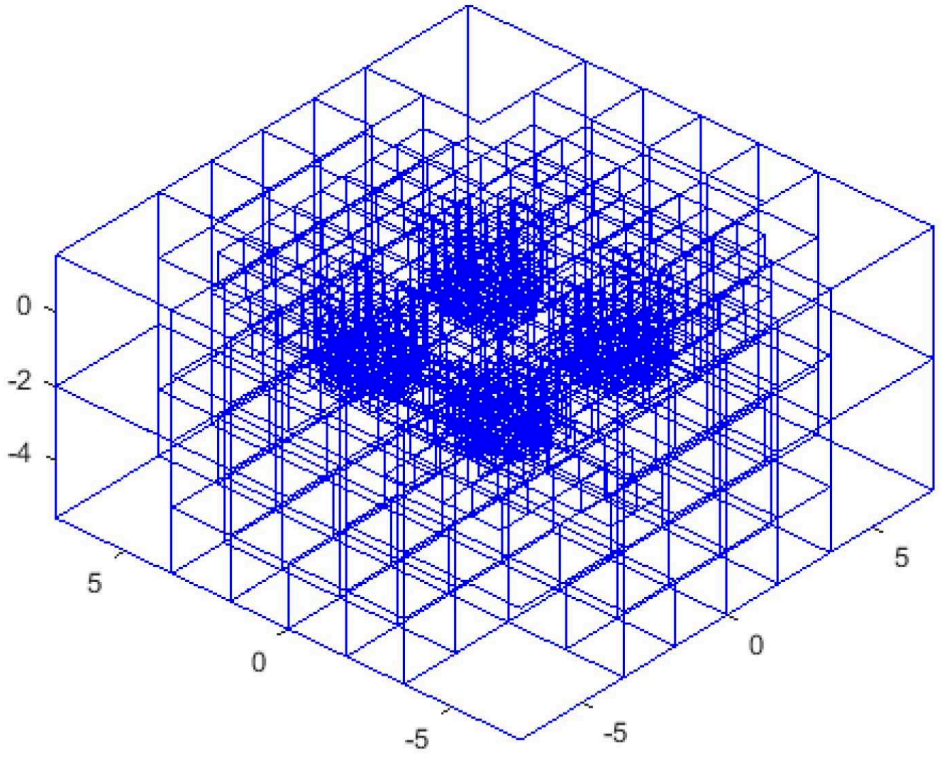

Figure 4.3: Adaptive octree for the four cylinder problem

The third step is to calculate the local coefficients $L_{a,b}$ for each cell. The local coefficients represent the effects of all the cells on one particular cell with the exception of a few adjacent ones which include the cell itself. The effects of the panels in the adjacent cells are computed using the direct method instead. The local coefficients for one cell with center Q_l due to a particular cell with center Q_c can be computed using the moment to local (M2L) translation:

$$L_{a,b}(Q_l) = (-1)^a \sum_{a'=0}^{\infty} \sum_{b'=-a'}^{a'} S_{a+a',b+b'}(Q_l - Q_c) M_{a',b'}, \qquad |P - Q_l| < |Q_c - Q_l|. \tag{4.28}$$

The advantage of the FMM is that the local coefficients can be translated from the parent cells to their children which in turn removes the requirement to account, on the child cell, for the influences of all the cells that have already influenced the parent cell. This local to local translation (L2L) is given by:

$$L_{a,b}(Q'_l) = \sum_{a'=a}^{\infty} \sum_{b'=-a'}^{a'} T_{a'-a,b'-b}(Q'_l - Q_l) L_{a',b'}(Q_l). \tag{4.29}$$

Naturally all these infinite summations have to be truncated at some point for the numerical calculation. It is possible to formally estimate the error from these assumptions (see [75]).

Central to the local expansion stage is the association to each cell, a map of cells that are adjacent (whose influence is calculated strictly using the direct method), cells in the interaction list (whose influence is computed using the M2L translation) and cells in the far list (whose influence is translated from the parent cell by the L2L translation). There are different approaches for assigning these lists but the common factor is that all the influences from all the cells must be accounted for and no influence is accounted for more than once. For the adaptive FMM, this task is not trivial. We cite the works in [75] and [76] for two possibilities. In this work, we adopt an approach that combines features from these two works. For each cell j, we assign every other cell k (starting from the top level downwards) into one of four lists. Any time a cell is assigned, all its descendants are ignored afterwards since their effect is already accounted for. Some cells do not fall into any of the lists but their descendants might. Otherwise, they would be in the far list and their is no need to account for them. Two cells are said to touch each other if any of their edges or vertices coincide. Also if cell j is at level L, then any cell at level greater than L is smaller and deeper down the tree so that the largest levels will be strictly occupied by leaves. The four lists are defined as follows:
List 1: if both cells j and k are leaves and touch each other
List 2: if both cells are at the same level of the tree, do not touch but their parent cells do
List 3: if cell j is a leaf at level L and cell k is at level $L+1$, they do not touch but j touches the parent of k
List 4: if cell j is a leaf at level L and cell k is at level greater than $L+1$, they do not touch but j touches the parent of k
In addition, cell j is added to List 4 of all cells in its List 3, and cell j is added to List 3 of all cells in its List 4. Finally, all cells in Lists 1 and 4 are considered adjacent cells while all those in Lists 2 and 3 are considered in the interaction list.

When all the local coefficients are calculated, it is then possible to find the influence of the associated panels on the target cell using the expression:

$$\int_S \delta G(P,Q)dS = \sum_{a=0}^{\infty}\sum_{b=-a}^{a} T_{a,b}(P-Q_l)L_{a,b}(Q_l). \tag{4.30}$$

4.5 Demonstration of The Method

The method described above was implemented and verified against the results in [42] for a single body as well as those in [68] for multiple bodies. The hybrid method itself was first tested in [61] and verified to return correct results. With regards to computational efficiency, we mentioned earlier that the method presented here has an $O(N)$ complexity in principle. The method consists of two parts. The first part is the influence of the inner domain panels computed using the FMM which has been proven to have the $O(N)$ behavior (see [15]). The second part is the influence of the outer domain potential represented by the factors in (4.20). Now assuming that the number of Fourier modes in (4.20) is kept constant as N

increases, then the complexity of this second part will have $O(N)$ behavior as well. This is a fair assumption given that these modes act in the frequency domain and the radiation boundary is usually far from the floating body for the latter to have significant influence on it. Put together, this will make the whole method scale as $O(N)$ as well.

To demonstrate the efficiency of the method, we ran a test case for a wide range of values of N as shown in figure 4.4. The case is that of four identical circular cylinders arranged in a circular fashion with a 90 degree angular phase between them over a constant water depth as in figure 4.2. This case could represent, for example, an ocean platform with four spars or a tension leg platform. For the case considered here, the radii of the four cylinders are assumed to be exactly 1, the distance from the origin to the cylinder centers is equal to 3.5 radii and the drafts are set to 2 radii. The water depth is 5 and the radius of the inner domain shown in the figure is 15 radii. In addition, we used a maximum of 90 panels in each leaf cell and we used 4 as an upper truncation limit for the series in equations (4.21) and (4.29) as well as $M_R = 5$ and $N_R = 9$. With these parameters, figure 4.4 shows the time required to perform one matrix vector multiplication of those required in an iterative solver to solve for the system in (4.17) as a function of the total number of unknowns N. The figure shows the expected approximately linear behavior with N.

Note that for this case, the direct influence coefficients were stored for adjacent cells to avoid having to compute them for every iteration. The same applies to the outer domain influence coefficients (equation (4.20)). This requires an $O(N)$ of memory. In addition, we used the stored direct influence coefficients to form a block diagonal matrix which was used as a preconditioner. That helped reduce the number of required iterations significantly.

4.6 Body Interactions With Variable Topography

As an example of the use of this numerical method, we study two problems:

4.6.1 Four Cylinders With a Parabolic Bottom Profile

The first case we consider here is that of four circular cylinders in proximity oscillating in water or subject to an incident wave. Figure 4.2, presented earlier, shows a small mesh of about 7600 panels for this problem. The actual simulation was performed on meshes of the order of 40000 panels. The problem solution is made unique to our method by introducing a variation in the topography of the ocean floor. The aim here is to see what is the consequence of installing the cylinders over a ground protrusion (assumed parabolic for demonstration) compared to the flat bottom case usually assumed. Figure 4.6 shows the cross section of the axisymmetric bottom profiles that we considered here. In addition and for comparison, we consider the flat bottom cases $h = 3.5, 5, 6.5$ which bound the protruded profiles. The case considered assigns a radius of $a = 1$ to each of the cylinders with a draft of 2, a distance of 1.5 in both x and y directions from the origin (see figure 4.5 where $s = 3$), and a radiation

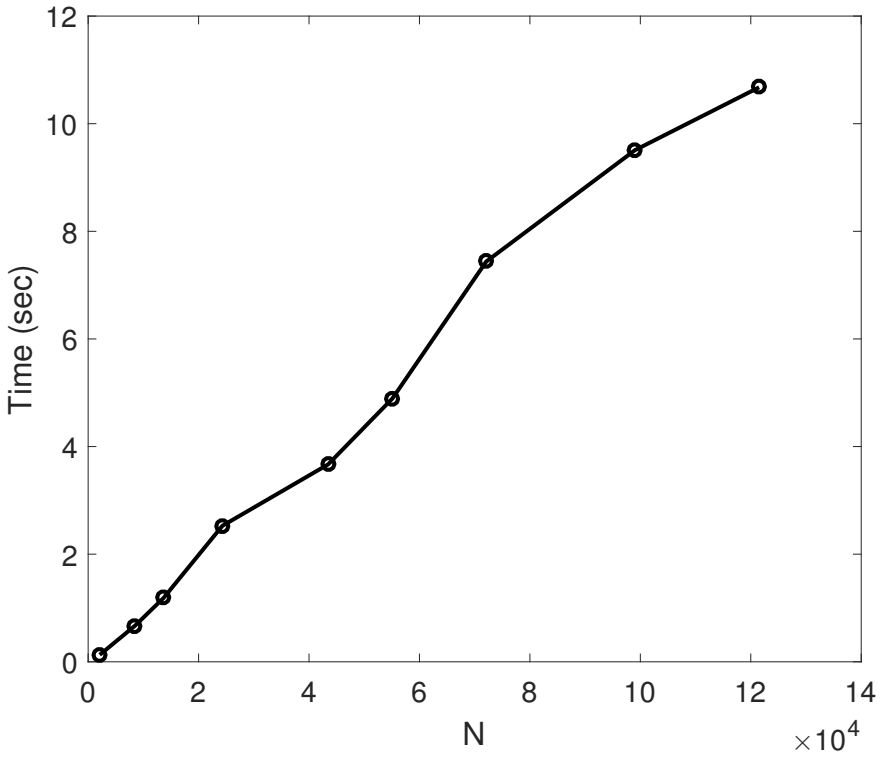

Figure 4.4: Plot of the time required for one matrix multiplication vs number of unknowns

boundary radius of 15. We also used $M_R = 5, N_R = 9$, and kept 8 terms in equations (4.21) and (4.29).

With the potential for a particular problem solved for, the loads on the bodies are obtained by an integration of the pressure over the surface area of each body. Since the problem is symmetric along both horizontal axes, it suffices to find the radiation loads due to the motion of one of the cylinders on all others. The radiation loads are traditionally separated into added mass $\mu_{jk} = \overline{\mu}_{jk}/\pi\rho a^c$ and damping coefficients $\lambda_{jk} = \overline{\lambda}_{jk}/\pi\rho\omega a^c$ for a forced motion with velocity U_j. Here, c is chosen to make the terms dimensionless depending on the mode of motion. These coefficients are given by:

$$\mu_{jk} + i\lambda_{jk} = \frac{1}{\pi}\int_{S_b} \phi_j n_k dS, \tag{4.31}$$

where integration is taken over the body of interest S_b only. This represents the load (force or moment) in the direction of motion k due to the motion of the body S_b in the direction j. For multiple bodies, the integration is taken over the surface of the body of interest using the potential caused by the motion of any of the other bodies. The diffraction loads are

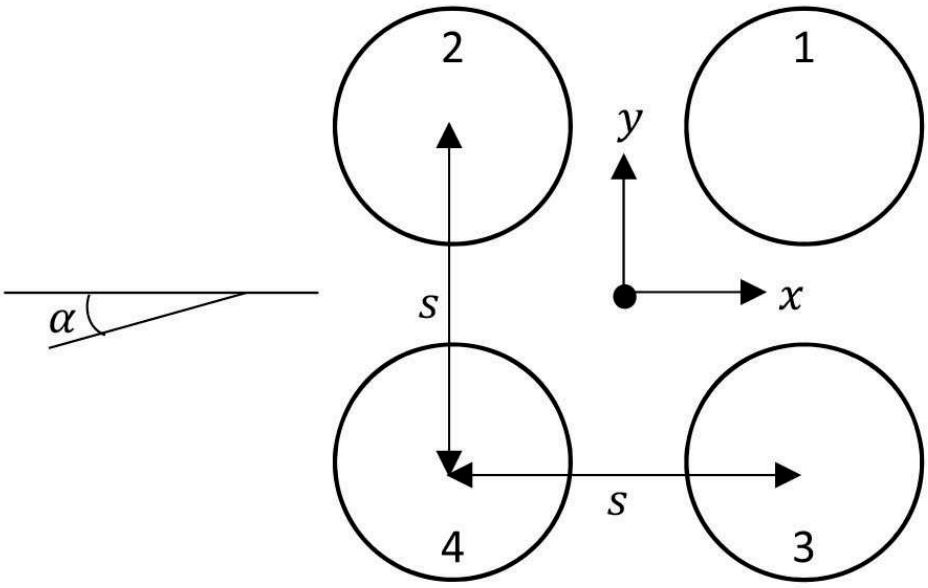

Figure 4.5: Schematic for the four cylinder problem

obtained in the same manner:

$$F_k = \frac{\overline{F}_k}{\pi\rho g\eta_0 a^d} = \frac{i\nu}{\pi}\int_{S_b}(\phi_7+\phi_0)n_k dS, \tag{4.32}$$

where d is chosen to make the expression dimensionless as needed (2 for forces and 3 for moments). More conveniently, F_k can be obtained by the use of the Haskind relation if ϕ_k from the radiation problem is available. The Haskind relation can be derived as follows. Consider Green's second identity for harmonic potentials ϕ_7 and ϕ_k:

$$\int_{S_B+S_F+S_T+S_R}\left(\phi_7\frac{\partial\phi_k}{\partial n}-\phi_k\frac{\partial\phi_7}{\partial n}\right)dS = 0. \tag{4.33}$$

Now upon using the known boundary conditions on ϕ_7 and ϕ_k, this simplifies to:

$$\int_{S_b}\phi_7 n_k dS = \int_{S_B+S_T}\phi_k\frac{\partial\phi_7}{\partial n}dS. \tag{4.34}$$

Since $\frac{\partial\phi_7}{\partial n} = -\frac{\partial\phi_0}{\partial n}$ on S_B and S_T then:

$$\int_{S_b}\phi_7 n_k dS = -\int_{S_B+S_T}\phi_k\frac{\partial\phi_0}{\partial n}dS. \tag{4.35}$$

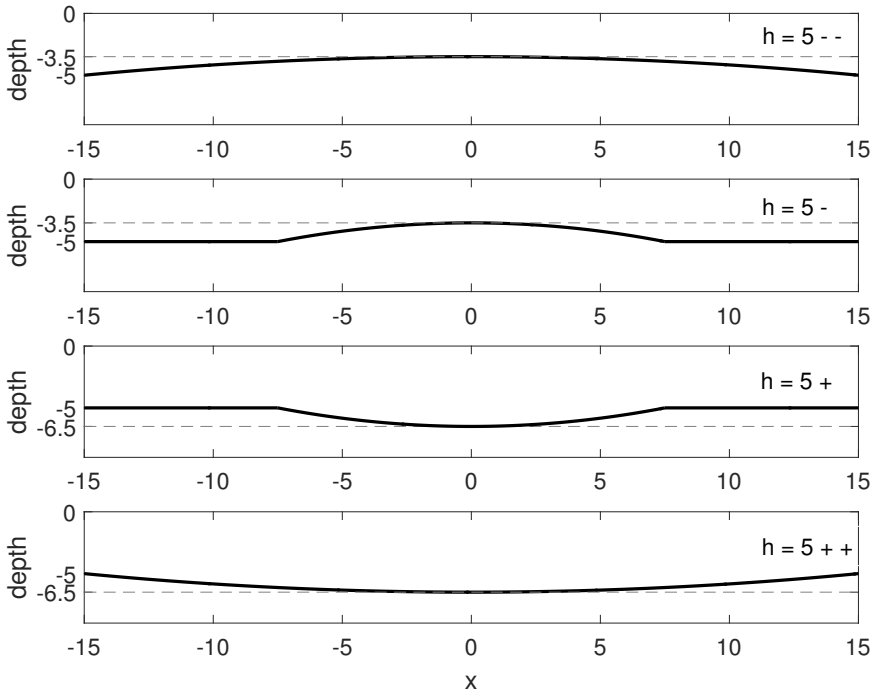

Figure 4.6: Cross-sections of the bottom profiles considered

Finally, the diffraction load is given by:

$$F_k = \frac{i\nu}{\pi}\int_{S_b}\phi_0 n_k dS - \frac{i\nu}{\pi}\int_{S_B+S_T}\phi_k\frac{\partial\phi_0}{\partial n}dS. \tag{4.36}$$

This way, the load can be obtained without having to solve the diffraction problem separately.

In figures 4.7-4.10, the notation used is that the superscripts mn indicate the effect of motion of body m on body n while the subscripts jk are as defined in 4.31. Figures 4.7 and 4.8 show the heave added mass and damping coefficients on body 4 (as labeled in figure 4.5) as it heaves with the other 3 bodies static. The effects of the variable topography appear to be more prominent in the damping results. It is interesting to note how the loads with the protruded cases change as a function of frequency. Since all protrusion topographies ($h = 5--, 5-, 5+, 5++$) have a limiting depth of $h = 5$ as we move outwards in the radial direction, the loads tend to that of the case $h = 5$ as the frequency approaches 0. However, as the wavelength approaches the size of the protrusion, the protrusion depth becomes the deciding factor and the results approach those of the corresponding flat-bottom depths. This is seen to occur at larger wavelengths for the cases $h = 5--$ and $h = 5++$ compared to those where $h = 5-$ or $h = 5+$ because the protrusion size is larger. It is also clear that the

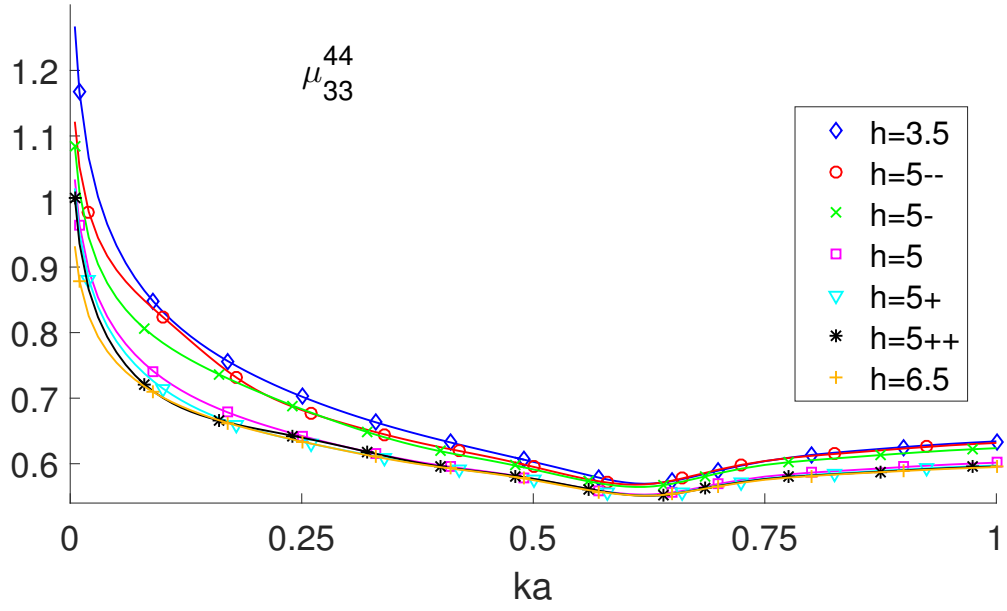

Figure 4.7: Added mass coefficients on body 4 in the z-direction due to heave of body 4

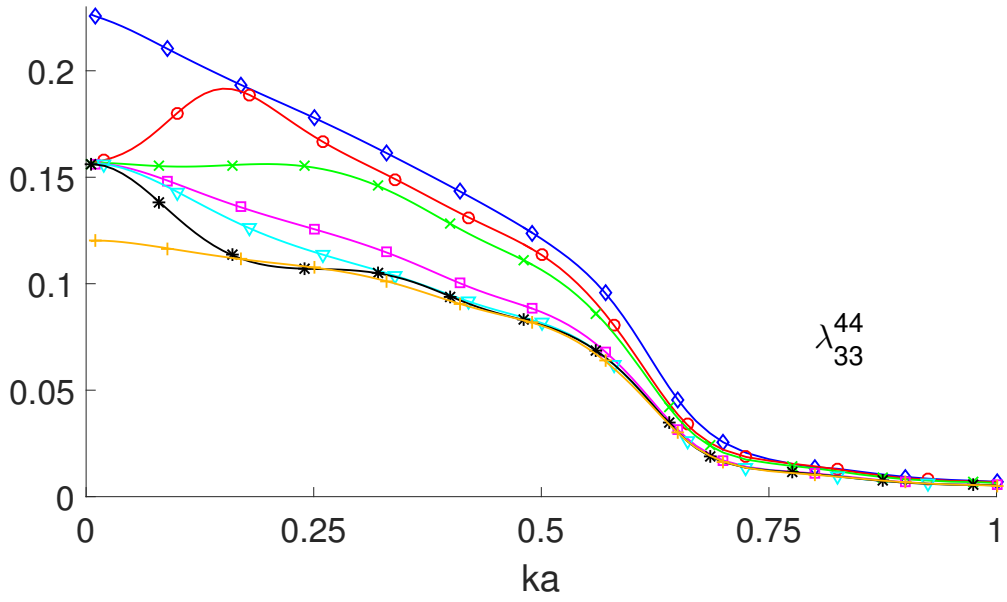

Figure 4.8: Damping coefficients on body 4 in the z-direction due to heave of body 4

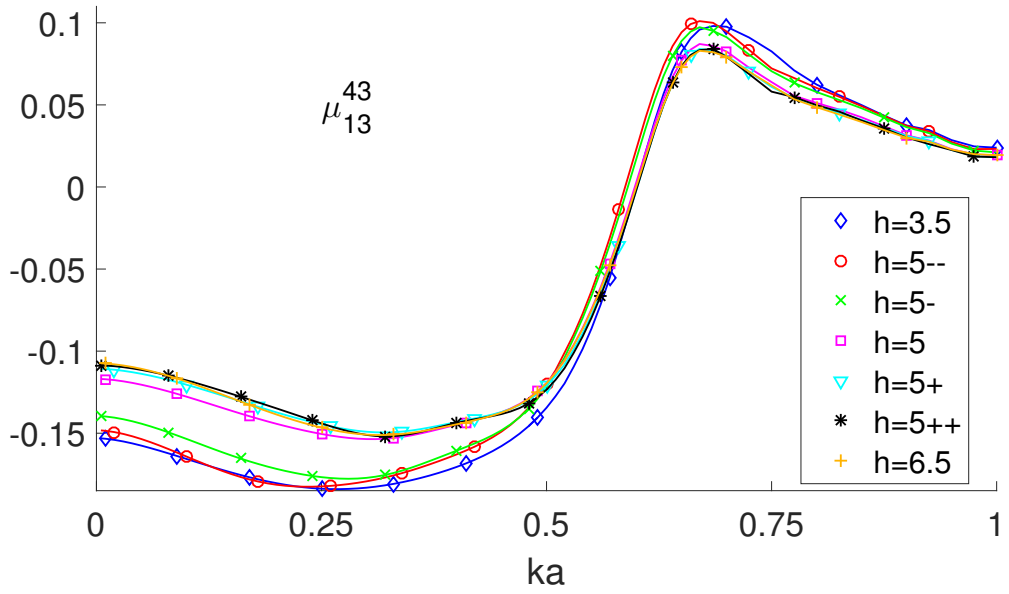

Figure 4.9: Added mass coefficients on body 3 in the z-direction due to surge of body 4

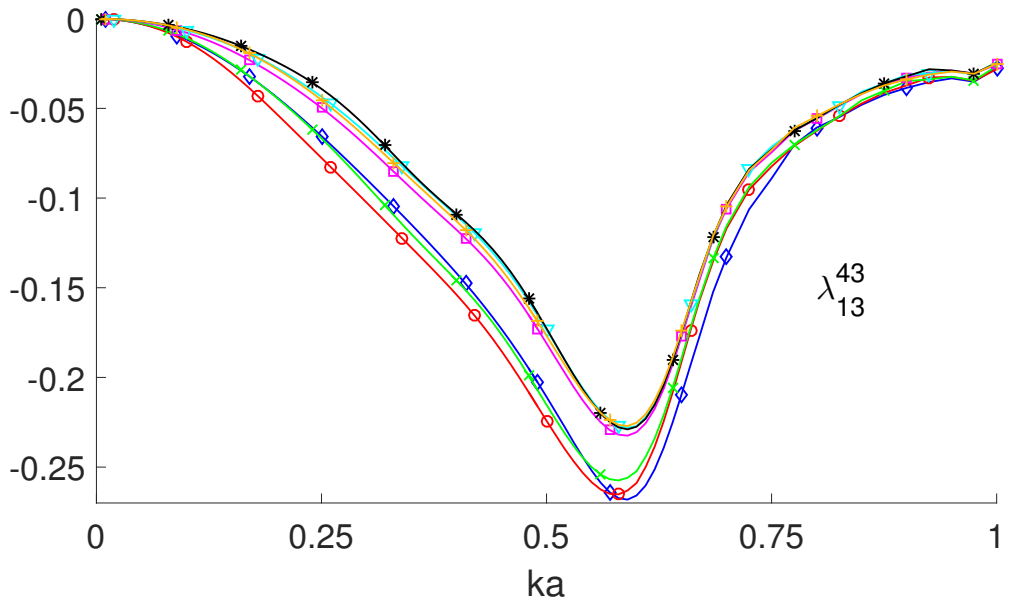

Figure 4.10: Damping coefficients on body 3 in the z-direction due to surge of body 4

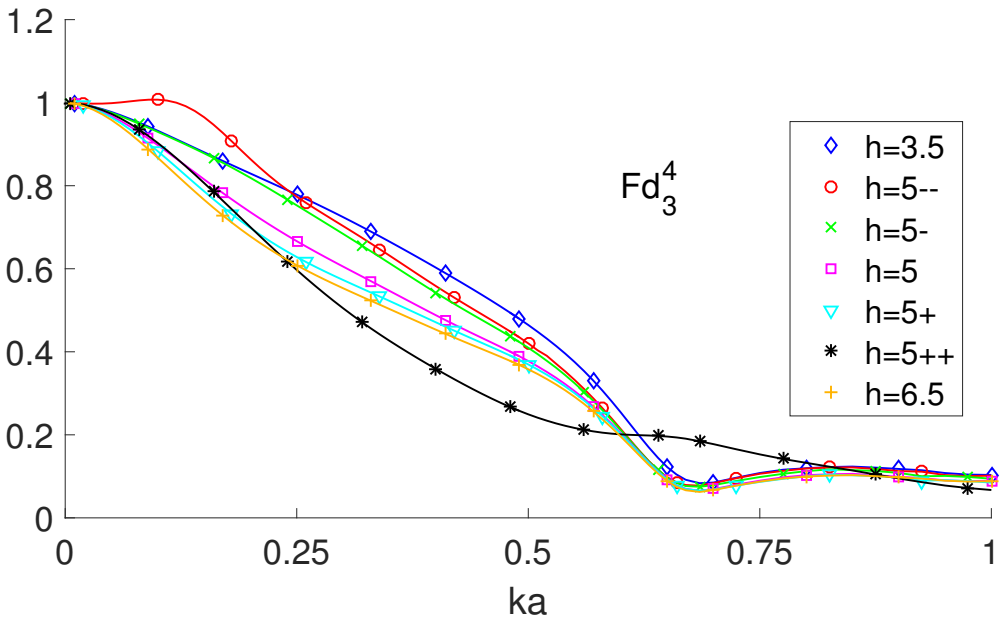

Figure 4.11: Diffraction on body 4 in the z-direction

results for the limiting depths of $h = 6.5$ and $h = 3.5$ envelope the rest of the other cases in between. A similar behavior is observed for the forces on the other bodies due to the heave motion of body 4.

An interesting observation is shown in figures 4.9 and 4.10 where the surge motion of body 4 causes a vertical load on body 3 that is affected by the protrusion size (with the water depth playing a more significant role). This is not observed for the horizontal load on the same body where it seems that the bulk of the interference between the two bodies is mostly transferred horizontally away from the bottom protrusion.

Finally, in figure 4.11, we show the vertical excitation force on body 4 as a wave approaches in the direction $\alpha = 0$. The interesting observation here is that a higher load is experienced at lower frequencies for the case $h = 5 - -$ while a higher load is experienced in the case $h = 5 + +$ at higher frequencies.

4.6.2 Sixteen Cylinders with Sinusoidal Bottom Profile

The second problem we will show here demonstrates the ability of the current method to deal with a problem with high number of unknowns. The problem is that of diffraction of incident waves hitting an array of 16 truncated cylinders arranged as in figure 4.12. In this figure, the cylinders are arranged onto three concentric circles having 10, 5 and 1 cylinders respectively. The coordinate system is at the center of cylinder 16. The center of cylinder 11 lies on the x-axis and the angle between different cylinders is $2\pi/5$ for the middle circle.

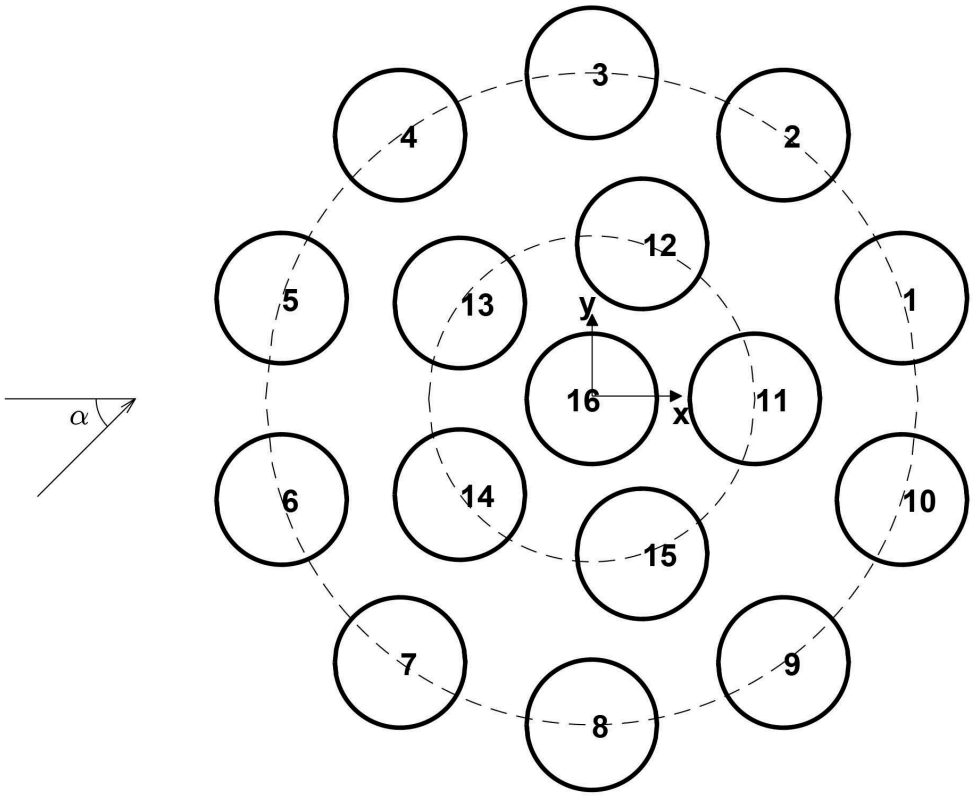

Figure 4.12: Schematic of the 16-cylinder problem

The center of cylinder 1 forms an angle of $\pi/10$ with the x-axis and the angle between the different cylinders on the outer circle is $\pi/5$. The radius of the middle circle is 2.5 and that of the outer circle is 5. Again, $a = 1$ is the radius of one cylindrical body. We compare the two cases when the bottom is flat and when it has a sinusoidal variation as shown in figures 4.13 and 4.14. The sinusoidal profile has the form $z_T = -h + 1.5 \times \sin(5\pi r/r_0)$ where r is the radial distance. We used about 150,000 triangular panels for this problem which is way beyond the capabilities of traditional boundary element solvers. Most panels are concentrated on the floating bodies.

Numerically, we also used $M_R = 10, N_R = 19$, and kept 8 terms in equations (4.21) and (4.29) for higher accuracy. Note that these number are significantly larger than those used to generate figure 4.4 and therefore required about 140 seconds per iteration on a 3 GHz single processor which is higher than suggested in that figure. The number of panels per leaf cell, which can be chosen arbitrarily as a hyper-parameter, also affects the processing time.

We will only consider results when the incident angle $\alpha = 0$. Figures 4.15 and 4.16 show what the amplitude of the potential function looks like as an incident wave approaches the group of cylinders. The matching of the potentials between the exterior and interior domains

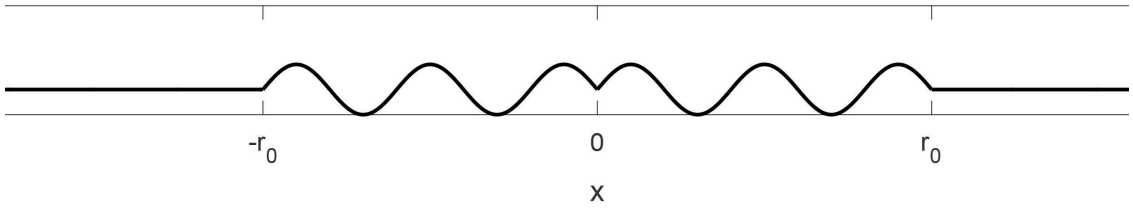

Figure 4.13: Cross-section of the sinusoidal bottom profile considered

Figure 4.14: Mesh of the sinusoidal bottom profile considered

is visible in figure 4.15. It is interesting that for this case, the maximum wave elevations actually happen just before the center of the group rather than at the first contact point as one might expect. Figure 4.17 shows the vertical force on the three bodies 6, 16 and 1 due to the incident wave. Each plot in the figure represents the load on a cylinder at a different position in the group and includes the case when the ocean floor is flat and when the sinusoidal variation is present. The results seem to indicate that higher loads are to be expected when the sinusoidal floor is present in all three cases. The results also predict higher loads on cylinder 6 (which is facing the incident wave) compared to 16 which also has a higher load than 1 but only at the lower frequencies. In the mid range frequencies ($ka \sim 0.35$), it seems that there is a constructive interference effect on body 16 in the center leading to higher loads.

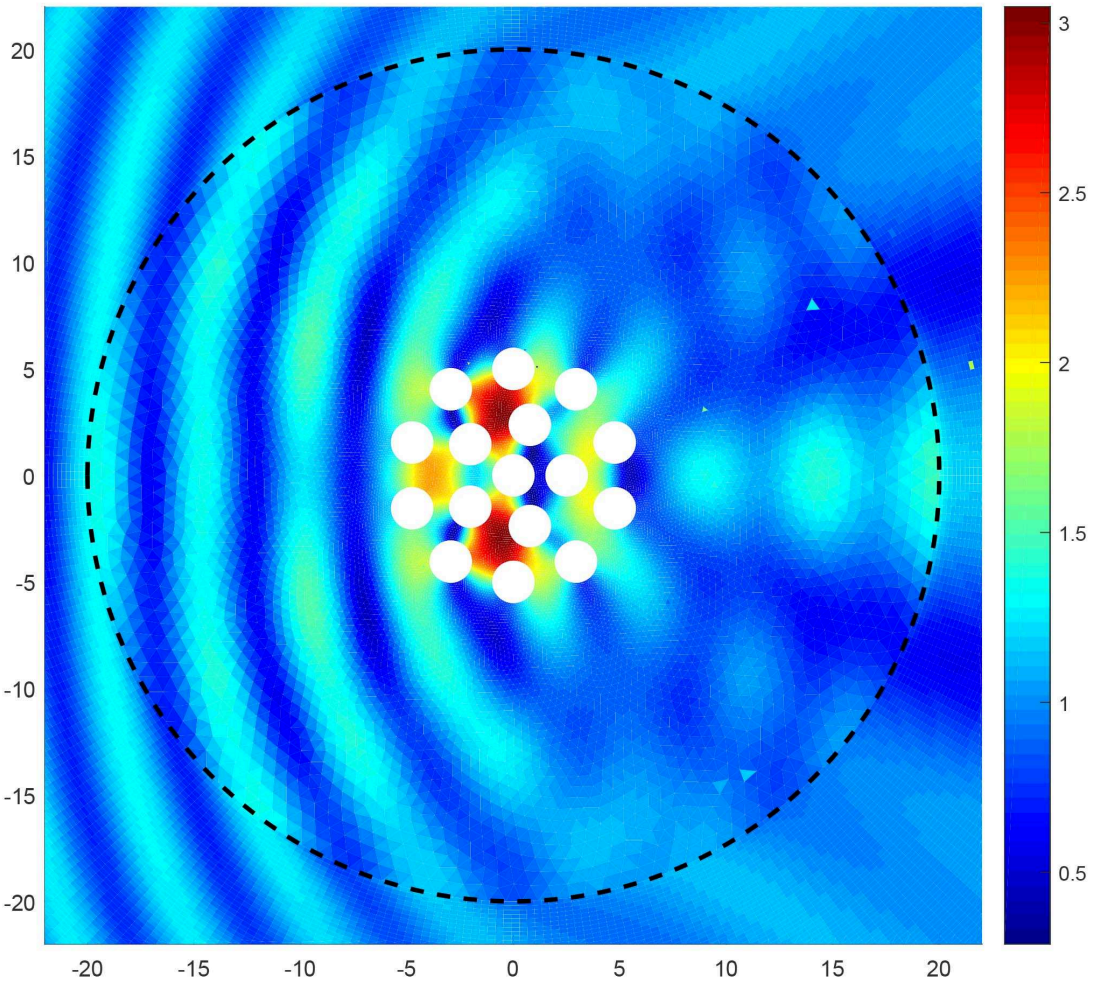

Figure 4.15: Plot of the free-surface potential amplitude $|\phi|$ (wave elevation amplitude) as a wave of $ka = 0.65$ approaches the 16-cylinder group from left to right over a flat bottom

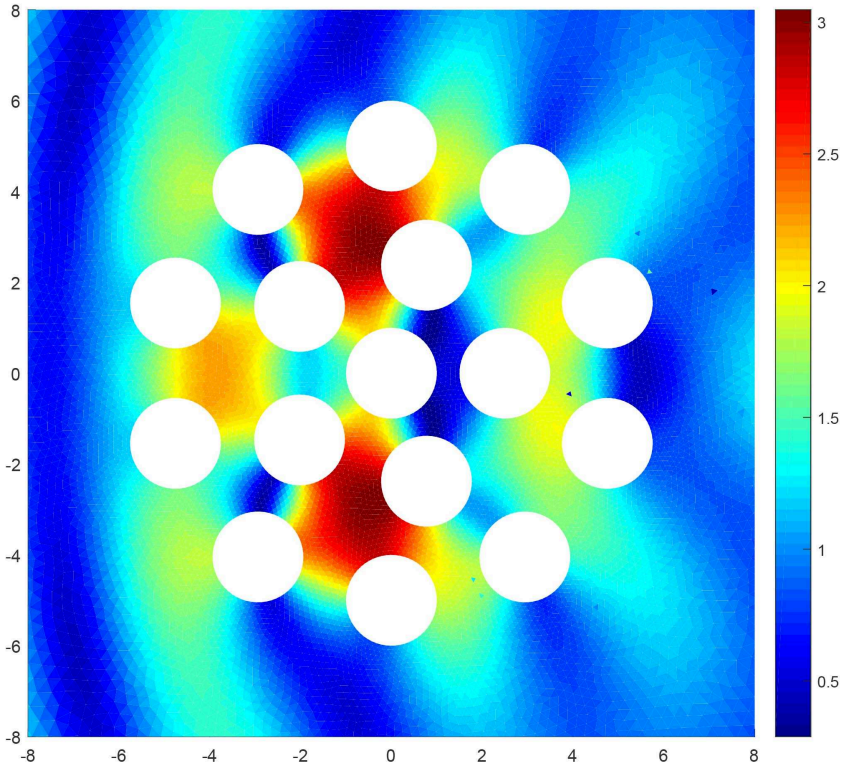

Figure 4.16: Close-up view of figure 4.15

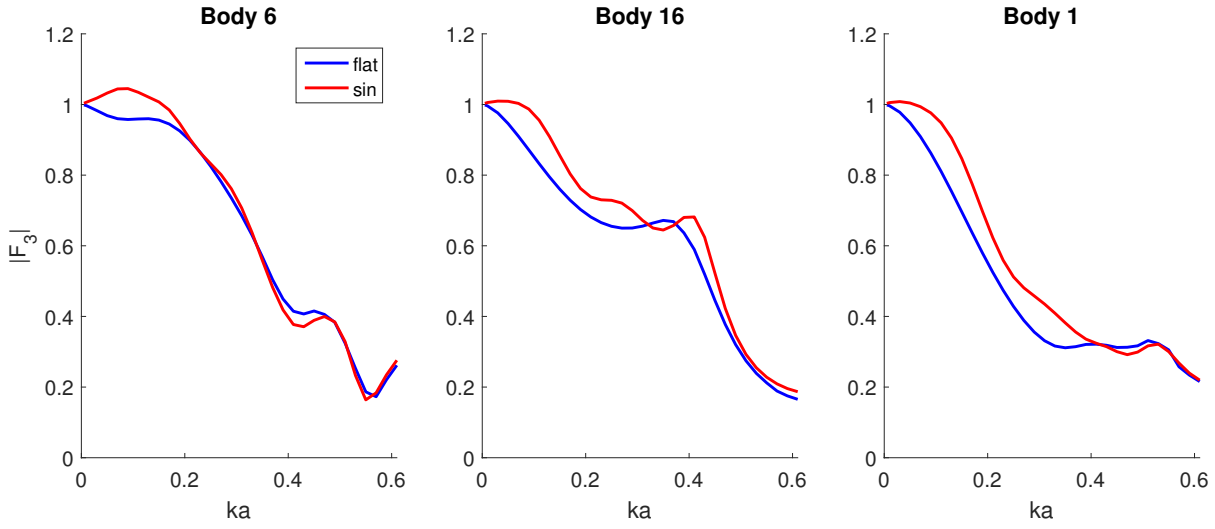

Figure 4.17: Vertical loads on three different bodies at the positions 6, 16 and 1 as indicated over flat and sinusoidal (sin) ocean floor due to incident wave along the x-axis

Chapter 5

Conclusions and Future Work

In this thesis, we explored new ways to advance the computational methods that are used to solve the linear water-wave problem. Our interest was mainly focused on floating bodies and the loads that are exerted by the waves on these bodies. Two new techniques for the numerical solution of the water wave problem were introduced. The first dealt with the computation of the wave field around thin bodies in the water while the second introduced a new method to reduce the computational effort required to solve the general linear problem with arbitrary body shape and arbitrary ocean floor topography. Both techniques were used to solve for particular problems of interest in order to demonstrate these methods and to gain insight into these types of problems. In addition, we developed a method to solve for the added mass of flat plates of arbitrary shapes and possibly with holes. These difficult to obtain results are missing from the literature and we decided to fill this gap by presenting many of those values of interest.

In chapter 2, we studied the effects of having open arbitrary cylindrical shells in a wave field. Both radiation and diffraction of waves from the body were considered and analyzed. This work also presented a simple way to treat problems that can be modeled using a hyper-singular integral equation. This last method is better conditioned and faster than a standard boundary integral formulation used to model bodies approaching zero thickness. The results are also more reliable. The same concepts presented here can be extended to more complicated problems. We presented several new results for loads acting on open cylinders that are circular, elliptical and squared in planform shape with a special emphasis on the effect of the increasing opening size. We also presented plots for the free surface elevation amplitude for wave radiation and diffraction from the bodies considered. The results are also extended to multiple bodies and the one case of an open circular harbor with a frontal breakwater is considered.

Results indicate that a significant change in the load profile occurs when the body is opened. Specifically, very large loads appear at lower frequencies along the direction of the opening especially when the shell is not opened widely. Smaller loads appear as the frequency increases when compared to the case of a closed shell except when the frequency approaches the resonant frequency of the internal region of the shell. Then the inside resonates partially, which causes higher loads. The loads in the direction perpendicular to the opening act differently. Surprisingly, the increasing opening size leads to smaller loads except at resonance. Zero loads were found possible for certain combinations of wave frequencies and opening size when the opening lies upstream. Zero loads are always possible for open structures in beam seas relative to the opening. In general, the opening has the possible advantage of decreasing the loads on the body.

With regards to wave radiation, it was found that the added mass decreases when the body is opened because the fluid in the direction of motion could escape from the shell. Remarkably, open bodies were also found to radiate more waves when the frequency is close to resonance as compared to the closed ones. Free surface plots also indicate regions of large oscillations and regions shielded from the incoming waves. These discoveries should be useful for marine operations.

The problem of an open harbor with a protective breakwater (tongue) was also considered. Results indicate that the breakwater might actually cause higher loads because of the inflicted resonance. The breakwater is effective though at high frequencies.

Possible future work on this subject may include a quantitative study of the effects exerted by nonlinear waves on the structures. It is expected that nonlinearity will move some of the energy from near resonance frequencies to higher and lower frequencies resulting in lower loads on the body. This will require solving the second order or higher wave problem using the formulations available in the literature or the full nonlinear problem, both cases requiring the use of a hypersingular formulation. The effects of viscosity and vortex shedding are also important for these types of structures. These constitute an even more daunting task as they require the solution of the full Navier Stokes equations or some reasonable approximation.

In chapter 3, we dealt with the problem of finding the added loads on thin plates of arbitrary shapes. The formulation of this problem again required handling hypersingular boundary integral equations albeit in a three dimensional setting. We neglected the presence of a free surface and approached the problem in a new way using a Galerkin formulation. We particularly were interested in holes present in these plates and their influence on the added load terms. The results presented for a circle, square and equilateral triangle shaped plates, all with a central hole, as well as those for an isosceles and right triangles make these results available for use as they are missing from the literature. A quick comparison with an algebraic method, which simply subtracts the added mass of the hole plate from the full plate, showed a significant difference with our numerical results indicating the need for their computation. Finally, a possible extension here is to include the effects of the free surface although a new approach might be required if the computational effort becomes unwieldy.

In chapter 4, we presented a new method to solve the linear water-wave problem when the number of unknowns is very large. The method is based on applying the Fast Multipole Method to a hybrid matching scheme. It has the advantage of being able to model variable ocean floor topography as well as handling multiple floating structures of arbitrary shapes all while scaling linearly with the number of unknowns. This allows for modeling more complex problems than is possible with other methods in the literature.

We demonstrated the linear complexity of the method and as an example, we presented two case studies. The first looked at the effects of different parabolic profiles of the ocean floor on a group of 4 truncated vertical cylinders arranged in a circular fashion. Our results indicate the importance of modeling the variable shape of the ocean floor, especially for the heave radiation problem. At very low frequencies, the profile shape is insignificant and the asymptotic depth is the only one that matters. As the frequency increases to the point when

the wavelength is about the same as the profile size, the bottom effects become important up to the point when the wave essentially sees the peak (or minimum) depth as the dominant water height rather than the asymptotic depth. The second case study was for the diffraction of incident waves over a group of 16 cylinders arranged over three concentric circles. This case was meant to show the ability of the current method to return accurate results when a large number of unknowns is required. Having an uneven ocean floor in this case seems to cause higher loads on the bodies.

A possible extension of this work is studying the effects of sea shores on wave energy farms designed to be placed close to shorelines. In addition, it is possible to develop similar methods for other types of marine problems such as the linear sea keeping problem.

Bibliography

[1] J. V. Wehausen and E. Laitone, "Surface waves," *Encyclopedia of Physics*, vol. 9, pp. 446–778, 1960.

[2] C. C. Mei, M. Stiassnie, and D. K.-P. Yue, *Theory and Applications of Ocean Surface Waves: Linear aspects*. World Scientific, 2005.

[3] J. Wackers, B. Koren, H. C. Raven, A. v. d. Ploeg, A. R. Starke, G. B. Deng, P. Queutey, M. Visonneau, T. Hino, and K. Ohashi, "Free-Surface Viscous Flow Solution Methods for Ship Hydrodynamics," *Arch Computat Methods Eng*, vol. 18, pp. 1–41, Mar. 2011.

[4] R. Scardovelli and S. Zaleski, "Direct Numerical Simulation of Free-Surface and Interfacial Flow," *Annual Review of Fluid Mechanics*, vol. 31, no. 1, pp. 567–603, 1999.

[5] A. Iafrati and E. F. Campana, "A domain decomposition approach to compute wave breaking (wave-breaking flows)," *Int. J. Numer. Meth. Fluids*, vol. 41, pp. 419–445, Feb. 2003.

[6] P. K. Kundu, I. M. Cohen, and D. R. Dowling, *Fluid Mechanics, Fifth Edition*. Waltham, MA: Academic Press, 5 edition ed., Sept. 2011.

[7] W. Tsai and a. D. K. P. Yue, "Computation of Nonlinear Free-Surface Flows," *Annual Review of Fluid Mechanics*, vol. 28, no. 1, pp. 249–278, 1996.

[8] J. V. Wehausen, "The Motion of Floating Bodies," *Annual Review of Fluid Mechanics*, vol. 3, no. 1, pp. 237–268, 1971.

[9] R. W. Yeung, "Numerical methods in free-surface flows," *Annual Review of Fluid Mechanics*, vol. 14, no. 1, pp. 395–442, 1982.

[10] J. N. Newman, "Algorithms for the free-surface Green function," *J Eng Math*, vol. 19, pp. 57–67, Mar. 1985.

[11] F. John, "On the motion of floating bodies II. Simple harmonic motions," *Comm. Pure Appl. Math.*, vol. 3, pp. 45–101, Mar. 1950.

[12] N. F. Parsons and P. A. Martin, "Scattering of water waves by submerged plates using hypersingular integral equations," *Applied Ocean Research*, vol. 14, no. 5, pp. 313–321, 1992.

[13] P. A. Martin and F. J. Rizzo, "On boundary integral equations for crack problems," *Proceedings of the Royal Society of London. Series A, Mathematical and Physical Sciences*, vol. 421, pp. 341–355, Feb. 1989.

[14] V. Rokhlin, "Rapid Solution of Integral Equations of Classical Potential Theory," *Journal of Computational Physics*, vol. 60, pp. 187–207, Sept. 1985.

[15] L. Greengard and V. Rokhlin, "A Fast Algorithm for Particle Simulations," *J. Comput. Phys.*, vol. 73, pp. 325–348, Dec. 1987.

[16] N. Nishimura, "Fast multipole accelerated boundary integral equation methods," *Appl. Mech. Rev*, vol. 55, pp. 299–324, July 2002.

[17] M. Vaidhyanathan and R. W. Yeung, "Wave Effects on Separated Flow about Bodies in a Free Surface," in *Symposium on Vorticity and Free-Surface Interactions, 12th U.S. National Congress of Applied Mechanics*, (Seattle, Washington), June 1994.

[18] R. Seah and R. W. Yeung, "Vortical-Flow Modeling for Ship Hulls in Forward and Lateral Motion," in *Proceedings of the 27th Symposium on Naval Hydrodynamics*, (Seoul, S. Korea), p. 21, Sept. 2008.

[19] Y. Jiang and R. W. Yeung, "Effects of Bilge Keels and Forward Speed on Roll Decay of Three Dimensional Hull," in *Proceedings of the 30th Symposium on Naval Hydrodynamics*, (Hobart, Tasmania, Australia), p. 20, Nov. 2014.

[20] L. Wang and R. W. Yeung, "Investigation of full and partial ground effects on a flapping foil hovering above a finite-sized platform," *Physics of Fluids*, vol. 28, July 2016.

[21] M. Hariri Nokob and R. W. Yeung, "Diffraction and radiation loads on open cylinders of thin and arbitrary shapes," *Journal of Fluid Mechanics*, vol. 772, pp. 649–677, June 2015.

[22] M. Hariri Nokob and R. Yeung, "Computation of arbitrary thin-shell vertical cylinders in a wave field by a hyper-singular integral-equation method," in *Proceedings of the ASME 33rd International Conference on Ocean, Offshore and Arctic Engineering*, (San Francisco), June 2014.

[23] C. J. R. Garrett, "Bottomless harbours," *Journal of Fluid Mechanics*, vol. 43, no. 03, pp. 433–449, 1970.

[24] M. Moreira, S. Sphaier, and M. Ferreira, "Monocolumn hull with internal dock: an alternative for offshore transport of people.," in *Proceedings of ASME 31st International Conference on Ocean, Offshore and Arctic Engineering (OMAE) 2012*, (Rio de Janeiro, Brazil), July 2012.

[25] S. Wampler, "Plan floated to ship cargo inspection offshore (newsline.llnl.gov)," July 2010.

[26] G. Krishnasamy, L. W. Schmerr, T. J. Rudolphi, and F. J. Rizzo, "Hypersingular boundary integral equations: Some applications in acoustic and elastic wave scattering," *J. Appl. Mech.*, vol. 57, pp. 404–414, June 1990.

[27] S. A. Mavrakos, "Hydrodynamic coefficients for a thick-walled bottomless cylindrical body floating in water of finite depth," *Ocean Engineering*, vol. 15, no. 3, pp. 213–229, 1988.

[28] N. F. Parsons and P. A. Martin, "Scattering of water waves by submerged curved plates and by surface-piercing flat plates," *Applied Ocean Research*, vol. 16, no. 3, pp. 129–139, 1994.

[29] P. A. Martin and L. Farina, "Radiation of water waves by a heaving submerged horizontal disc," *Journal of Fluid Mechanics*, vol. 337, pp. 365–379, 1997.

[30] L. Farina and P. A. Martin, "Scattering of water waves by a submerged disc using a hypersingular integral equation," *Applied Ocean Research*, vol. 20, pp. 121–134, June 1998.

[31] E. Renzi and F. Dias, "Resonant behavior of an oscillating wave energy converter in a channel," *Journal of Fluid Mechanics*, vol. 701, pp. 482–510, 2012.

[32] R. Yeung and M. Hariri Nokob, "Hypersingular integral-equation solution for a finite-draft surface-piercing cylindrical shell at high- and low-frequency," in *The 28th International Workshop on Water Waves and Floating Bodies*, (L'Isle sur la Sorgue, France), Apr. 2013.

[33] M. Hariri Nokob and R. W. Yeung, "Hypersingular integral-equation method for wave diffraction about arbitrary, shell-like vertical cylinders in finite-depth waters," in *The 29th International Workshop on Water Waves and Floating Bodies*, (Osaka, Japan), Mar. 2014.

[34] A. J. Burton and G. F. Miller, "The application of integral equation methods to the numerical solution of some exterior boundary-value problems," *Proceedings of the Royal Society of London. Series A, Mathematical and Physical Sciences*, vol. 323, pp. 201–210, June 1971.

[35] C.-H. Lee and P. D. Sclavounos, "Removing the irregular frequencies from integral equations in wave-body interactions," *Journal of Fluid Mechanics*, vol. 207, pp. 393–418, 1989.

[36] M. Guiggiani, "Hypersingular boundary integral equations have an additional free term," *Computational Mechanics*, vol. 16, July 1995.

[37] G. D. Manolis and P. K. Banerjee, "Conforming versus non-conforming boundary elements in three-dimensional elastostatics," *Int. J. Numer. Meth. Engng.*, vol. 23, pp. 1885–1904, Oct. 1986.

[38] P. A. Martin and F. J. Rizzo, "Hypersingular integrals: How smooth must the density be?," *International Journal for Numerical Methods in Engineering*, vol. 39, no. 4, pp. 687–704, 1996.

[39] V. Sladek and J. Sladek, *Singular Integrals in Boundary Element Methods*. Southampton, UK ; Boston: WIT Press / Computational Mechanics, Sept. 1998.

[40] H. Hadavinia, R. P. Travis, and R. T. Fenner, "C1-continuous generalised parabolic blending elements in the boundary element method," *Mathematical and Computer Modelling*, vol. 31, pp. 17–34, Apr. 2000.

[41] P. A. Martin, "End-point behaviour of solutions to hypersingular integral equations," *Proceedings: Mathematical and Physical Sciences*, vol. 432, pp. 301–320, Feb. 1991.

[42] R. W. Yeung, "Added mass and damping of a vertical cylinder in finite-depth waters," *Applied Ocean Research*, vol. 3, pp. 119–133, July 1981.

[43] J. N. Newman, *Marine hydrodynamics*. Cambridge, MA, USA: The Mit Press, 1977.

[44] C. C. Mei, M. Stiassnie, and D. K.-P. Yue, *Theory and Applications of Ocean Surface Waves: Nonlinear aspects*. World Scientific, 2005.

[45] J. W. Miles and Y. K. Lee, "Helmholtz resonance of harbours," *Journal of Fluid Mechanics*, vol. 67, no. 03, pp. 445–464, 1975.

[46] R. W. Yeung and R. K. M. Seah, "On helmholtz and higher-order resonance of twin floating bodies," *J Eng Math*, vol. 58, pp. 251–265, Aug. 2007.

[47] L. E. Kinsler, A. Frey, A. Coppens, and J. Sanders, *Fundamentals of Acoustics*. New York: Wiley, 2000.

[48] R. W. Yeung and S. H. Sphaier, "Wave-interference effects on a truncated cylinder in a channel," *J Eng Math*, vol. 23, pp. 95–117, June 1989.

[49] C. M. Linton and D. V. Evans, "Hydrodynamic characteristics of bodies in channels," *Journal of Fluid Mechanics*, vol. 252, pp. 647–666, July 1993.

[50] D. Sarkar, E. Renzi, and F. Dias, "Wave farm modelling of oscillating wave surge converters," *Proc. R. Soc. A*, vol. 470, p. 20140118, July 2014.

[51] M. Hariri Nokob and R. W. Yeung, "Added mass of thin plates of arbitrary shapes with possible openings," *Applied Ocean Research, (submitted, under review)*, 2018.

[52] E. H. Kennard, *Irrotational flow of frictionless fluids : mostly of invariable density*. Washington : U.S. Govt. Print. Off., 1967.

[53] R. G. Dong, "Effective Mass and Damping of Submerged Structures," Tech. Rep. UCRL-52342, California Univ., Livermore (USA). Lawrence Livermore Lab., Apr. 1978.

[54] N. I. Ioakimidis, "Exact expression for a two-dimensional finite-part integral appearing during the numerical solution of crack problems in three-dimensional elasticity," *Commun. appl. numer. methods*, vol. 1, pp. 183–189, July 1985.

[55] L. Gray, J. Glaeser, and T. Kaplan, "Direct Evaluation of Hypersingular Galerkin Surface Integrals," *SIAM J. Sci. Comput.*, vol. 25, pp. 1534–1556, Jan. 2004.

[56] P. Persson and G. Strang, "A Simple Mesh Generator in MATLAB," *SIAM Rev.*, vol. 46, pp. 329–345, Jan. 2004.

[57] W. Meyerhoff, "Added masses of thin rectangular plates calculated from potential theory," *J Ship Res*, vol. 14, pp. 100–111, 1970.

[58] K. Bai and R. W. Yeung, "Numerical Solutions to Free-Surface Flow Problems," in *Proceedings of the 10th Symposium of Naval Hydrodynamics*, (Cambridge, MA, USA), pp. 609–647, June 1974.

[59] R. Yeung, "A Hybrid Integral-Equation Method for Time-Harmonic Free-Surface Flow," in *First International Conference on Numerical Ship Hydrodynamics*, (Gaithersburg, Md, USA), pp. 581–607, Oct. 1975.

[60] M. M. F. Yuen and F. P. Chau, "A Hybrid Integral Equation Method for Wave Forces on Three-Dimensional Offshore Structures," *J. Offshore Mech. Arct. Eng*, vol. 109, no. 3, pp. 229–236, 1986.

[61] T. Matsui, K. Kato, and T. Shirai, "A hybrid integral equation method for diffraction and radiation of water waves by three-dimensional bodies," *Computational Mechanics*, vol. 2, no. 2, pp. 119–135, 1987.

[62] R. W. Yeung and Y. C. Bouger, "A hybrid integral-equation method for steady two-dimensional ship waves," *Int. J. Numer. Meth. Engng.*, vol. 14, pp. 317–336, Jan. 1979.

[63] T. Matsui, T. Suzuki, and Y. Sakoh, "Second-Order Diffraction Forces On Floating Three-Dimensional Bodies In Regular Waves," *International Journal of Offshore and Polar Engineering*, vol. 2, Sept. 1992.

[64] K. A. Belibassakis, "A boundary element method for the hydrodynamic analysis of floating bodies in variable bathymetry regions," *Engineering Analysis with Boundary Elements*, vol. 32, pp. 796–810, Oct. 2008.

[65] J. A. Hamilton and R. W. Yeung, "Viscous and inviscid matching of three-dimensional free-surface flows utilizing shell functions," *J Eng Math*, vol. 70, pp. 43–66, July 2011.

[66] J. N. Newman, "Efficient hydrodynamic analysis of very large floating structures," *Marine Structures*, vol. 18, pp. 169–180, Mar. 2005.

[67] Q. Zhong and R. W. Yeung, "Wave-body Interactions among an array of truncated vertical cylinders," in *Proceedings of the ASME 35th International Conference on Offshore Mechanics and Arctic Engineering*, vol. OMAE2016-55055, (Busan, S. Korea), June 2016.

[68] H. Kagemoto and D. K. P. Yue, "Interactions among multiple three-dimensional bodies in water waves: an exact algebraic method," *Journal of Fluid Mechanics*, vol. 166, pp. 189–209, May 1986.

[69] J. R. Phillips and J. K. White, "A precorrected-FFT method for electrostatic analysis of complicated 3-D structures," *IEEE Transactions on Computer-Aided Design of Integrated Circuits and Systems*, vol. 16, pp. 1059–1072, Oct. 1997.

[70] D. Kring, T. Korsmeyer, J. Singer, and J. White, "Analyzing mobile offshore bases using accelerated boundary-element methods," *Marine Structures*, vol. 13, pp. 301–313, July 2000.

[71] J. N. Newman, "Wave Effects on Multiple Bodies," in *Hydrodynamics in Ship and Ocean Engineering*, (RIAM, Kyushu University), pp. 3–26, Apr. 2001.

[72] T. Utsunomiya, E. Watanabe, and N. Nishimura, "Fast multipole method for hydrodynamic analysis of very large floating structures," in *Proc. 16th Intl. Workshop on Water Waves and Floating Bodies*, (Hiroshima, Japan), 2001.

[73] M. Hariri Nokob and R. W. Yeung, "A fast multipole method for the three dimensional linear water- wave/structure interaction problem with arbitrary bottom topography," *to be submitted to Journal of Computational Mechanics*, 2018.

[74] Y. Liu, *Fast Multipole Boundary Element Method: Theory and Applications in Engineering*. Cambridge ; New York: Cambridge University Press, 1 edition ed., Aug. 2009.

[75] H. Cheng, L. Greengard, and V. Rokhlin, "A Fast Adaptive Multipole Algorithm in Three Dimensions," *Journal of Computational Physics*, vol. 155, pp. 468–498, Nov. 1999.

[76] L. Shen and Y. J. Liu, "An Adaptive Fast Multipole Boundary Element Method for Three-dimensional Potential Problems," *Comput Mech*, vol. 39, no. 6, pp. 681–691, 2007.

[77] M. Abramowitz and I. A. Stegun, *Handbook of Mathematical Functions with Formulas, Graphs, and Mathematical Tables*. New York: Dover, ninth dover printing, tenth gpo printing ed., 1964.

Appendix A

Treatment of the Hypersingular Integrals

We left the details of the treatment the hypersingular integral to this appendix because they require some explanation. The integrals in (2.18) span the range of $[0, 1]$ in the parameter t and are only singular when the collocation point lies on one of the ends of that interval. The idea here is to approximate the kernel by its Taylor series close to the singular edge and integrate analytically while performing numerical integration over the rest of the panel length. We will only consider the range of integration $[0, T]$ or $[1 - T, 1]$ for a collocation point placed on $t = 0$ or $t = 1$ respectively and for some suitable T.

The kernels that are to be integrated here have different forms. They will include both hypersingular terms ($O(t^{-2})$) and singular terms ($O(t^{-1})$). The singular terms cancel out with those from the integral over the adjacent panel (Principle Values) provided the normal vector is continuous. The hypersingular ones do not though. However, as explained in [13], if the density belongs to $C^{1,\alpha}$, it is possible to consider the finite part (in the sense of Hadamard) of these integrals. It follows then that all we have to do is analytically remove the singular and hypersingular parts.

One point to note here is that while the density function is chosen to have enough continuity, our choice for straight panels to approximate the surface of the body will lead to a discontinuous normal vector at the panel edge and therefore a discontinuous kernel. That can be remedied by choosing a higher order approximation for the shell. However, as pointed out in [38], a discontinuous density is allowed if the definition of the integral is changed to remove any unbounded terms. In fact, we can justify doing that in this case because as we remove the singular terms, we effectively assume that we are using the same normal vector for the singular parts of the kernel but not for the regular parts. The following integrals (definitions) will be used:

$$\int_0^{R_0} \frac{1}{s^2} ds = \lim_{\epsilon \to 0} \int_\epsilon^{R_0} \frac{1}{s^2} ds - \frac{1}{\epsilon} = -\frac{1}{R_0}, \tag{A.1}$$

$$\int_0^{R_0} \frac{1}{s} ds = \lim_{\epsilon \to 0} \int_\epsilon^{R_0} \frac{1}{s} ds + \ln(\epsilon) = \ln(R_0), \tag{A.2}$$

$$\int_{S-R_0}^{S} \frac{1}{(s-S)^2} ds = \lim_{\epsilon \to 0} \int_{S-R_0}^{S-\epsilon} \frac{1}{(s-S)^2} ds - \frac{1}{\epsilon} = -\frac{1}{R_0}, \tag{A.3}$$

$$\int_{S-R_0}^{S} \frac{s}{(s-S)^2} ds = \lim_{\epsilon \to 0} \int_{S-R_0}^{S-\epsilon} \frac{s}{(s-S)^2} ds - \ln(\epsilon) - \frac{S}{\epsilon} = -\ln(R_0) - \frac{S}{R_0}, \tag{A.4}$$

$$\begin{aligned} \int_{S-R_0}^{S} \frac{s^2}{(s-S)^2} ds &= \lim_{\epsilon \to 0} \int_{S-R_0}^{S-\epsilon} \frac{s^2}{(s-S)^2} ds - 2S\ln(\epsilon) - \frac{S^2}{\epsilon} \\ &= -2S\ln(R_0) + R_0 - \frac{S^2}{R_0}, \end{aligned} \tag{A.5}$$

$$\begin{aligned} \int_{S-R_0}^{S} \frac{s^3}{(s-S)^2} ds &= \lim_{\epsilon \to 0} \int_{S-R_0}^{S-\epsilon} \frac{s^3}{(s-S)^2} ds - 3S^2\ln(\epsilon) - \frac{S^3}{\epsilon} \\ &= -3S^2\ln(R_0) + 3R_0 S - \frac{R_0^2}{2} - \frac{S^3}{R_0}. \end{aligned} \tag{A.6}$$

The parameter $R_0 < S$, with S a shorthand for S_j, is a number chosen small enough to provide the required accuracy in the Taylor expansion in what follows. We note here, as was pointed out in [13], that the integrals with strong singularities are not independent of scaling the variable of integration. Here we integrate using the original variables to avoid that problem.

Using the fact that when the singular point is at $t = 0$ or 1, then $R = St$ and $S(1-t)$ respectively, we can Taylor-expand the kernel of (2.12) as:

$$\begin{aligned} \frac{\partial^2 G_n}{\partial n_P \partial n_Q} &= A_1 \left(\frac{4}{\kappa_n^2 S_j^2 (t-t_s)^2} + 1 \right) \\ &\quad - A_2 \left(1 + \frac{2i}{\pi} \left(\ln\left(\frac{\kappa_n S_j |t-t_s|}{2} \right) + \gamma - \frac{2}{\kappa_n^2 S_j^2 (t-t_s)^2} - \frac{1}{2} \right) \right) \\ &\quad + O(R^2 \ln(R)), \end{aligned} \tag{A.7}$$

$$A_1 = \frac{\kappa_n^2}{4\pi S_j^2} \left(a_1^2 \sin(\alpha_j)\sin(\theta_j) + a_2^2 \cos(\alpha_j)\cos(\theta_j) - a_1 a_2 \sin(\theta_j + \alpha_j) \right),$$

$$A_2 = -\frac{i\kappa_n^2 \cos(\theta - \alpha)}{8}.$$

Here, γ is Euler's constant, $a_1 = \xi_{j+1} - \xi j$ and $a_2 = \zeta_{j+1} - \zeta_j$. Clearly a hypersingular point of order R^{-2} exists. This expression will be integrated analytically in the neighborhood of the singular point in (2.18). The required integrals when the collocation point lies on the

starting edge of the panel are then are evaluated as:

$$I_0 = \int_0^{R_0} \frac{\partial^2 G_n}{\partial n_P \partial n_Q} ds = A_1 R_0 \left(1 - \frac{4}{\kappa_n^2 R_0^2}\right) - A_2 R_0 \left[1 + \frac{i}{\pi}\left(2\ln(\frac{\kappa_n R_0}{2}) + 2\gamma + \frac{4}{\kappa_n^2 R_0^2} - 3\right)\right], \tag{A.8}$$

$$I_1 = \int_0^{R_0} s \frac{\partial^2 G_n}{\partial n_P \partial n_Q} ds = A_1 R_0^2 \left(\frac{1}{2} + \frac{4\ln(R_0)}{\kappa_n^2 R_0^2}\right) - A_2 R_0^2 \left[\frac{1}{2} + \frac{i}{\pi}\left(\ln(\frac{\kappa_n R_0}{2}) + \gamma - \frac{4\ln(R_0)}{\kappa_n^2 R_0^2} - 1\right)\right], \tag{A.9}$$

$$I_2 = \int_0^{R_0} s^2 \frac{\partial^2 G_n}{\partial n_P \partial n_Q} ds = A_1 R_0^3 \left(\frac{1}{3} + \frac{4}{\kappa_n^2 R_0^2}\right) - A_2 R_0^3 \left[\frac{1}{3} + \frac{i}{\pi}\left(\frac{2}{3}\ln(\frac{\kappa_n R_0}{2}) + \frac{2}{3}\gamma - \frac{4}{\kappa_n^2 R_0^2} - \frac{5}{3}\right)\right], \tag{A.10}$$

$$I_3 = \int_0^{R_0} s^3 \frac{\partial^2 G_n}{\partial n_P \partial n_Q} ds = A_1 R_0^4 \left(\frac{1}{4} + \frac{2}{\kappa_n^2 R_0^2}\right) - A_2 R_0^4 \left[\frac{1}{4} + \frac{i}{\pi}\left(\frac{1}{2}\ln(\frac{\kappa_n R_0}{2}) + \frac{1}{2}\gamma - \frac{2}{\kappa_n^2 R_0^2} - \frac{3}{8}\right)\right], \tag{A.11}$$

while the integrals required when the collocation point lies on the ending edge are:

$$J_0 = \int_{S-R_0}^{S} \frac{\partial^2 G_n}{\partial n_P \partial n_Q} ds = I_0, \tag{A.12}$$

$$J_1 = \int_{S-R_0}^{S} s \frac{\partial^2 G_n}{\partial n_P \partial n_Q} ds = A_1 R_0^2 \left(\frac{1}{T} - \frac{1}{2} - \frac{4}{\kappa_n^2 R_0^2}\left(\ln(R_0) + \frac{1}{T}\right)\right) - A_2 R_0^2 \Bigg[\frac{1}{T} - \frac{1}{2} + \frac{i}{\pi}\Bigg((\frac{2}{T} - 1)\left(\ln(\frac{\kappa_n R_0}{2}) + \gamma\right) + \frac{4}{\kappa_n^2 R_0^2}\left(\ln(R_0) + \frac{1}{T}\right) + 1 - \frac{3}{T}\Bigg)\Bigg], \tag{A.13}$$

$$J_2 = \int_{S-R_0}^{S} s^2 \frac{\partial^2 G_n}{\partial n_P \partial n_Q} ds = A_1 R_0^3 \left(\frac{1}{3} - \frac{1}{T} + \frac{1}{T^2} - \frac{4}{\kappa_n^2 R_0^2}\left(\frac{2}{T}\ln(R_0) - 1 + \frac{1}{T^2}\right)\right) - A_2 R_0^3 \Bigg[\frac{1}{3} - \frac{1}{T} + \frac{1}{T^2} + \frac{i}{\pi}\Bigg(2\left(\frac{1}{3} - \frac{1}{T} + \frac{1}{T^2}\right)\left(\ln(\frac{\kappa_n R_0}{2}) + \gamma\right) + \frac{4}{\kappa_n^2 R_0^2}\left(\frac{2}{T}\ln(R_0) - 1 + \frac{1}{T^2}\right) - \frac{5}{9} + \frac{2}{T} - \frac{3}{T^2}\Bigg)\Bigg], \tag{A.14}$$

$$
\begin{aligned}
J_3 &= \int_{S-R_0}^{S} s^3 \frac{\partial^2 G_n}{\partial n_P \partial n_Q} ds \\
&= A_1 R_0^4 \left(-\frac{1}{4} + \frac{1}{T} - \frac{3}{2T^2} + \frac{1}{T^3} - \frac{4}{\kappa_n^2 R_0^2} \left(\frac{3}{T^2} \ln(R_0) + \frac{1}{2} - \frac{3}{T} + \frac{1}{T^3} \right) \right) \\
&- A_2 R_0^4 \Bigg[-\frac{1}{4} + \frac{1}{T} - \frac{3}{2T^2} + \frac{1}{T^3} + \frac{i}{\pi} \Bigg(2 \Bigg(-\frac{1}{4} + \frac{1}{T} - \frac{3}{2T^2} + \frac{1}{T^3} \Bigg) \Bigg(\ln(\frac{\kappa_n R_0}{2}) + \gamma \Bigg) \\
&+ \frac{4}{\kappa_n^2 R_0^2} \left(\frac{3}{T^2} \ln(R_0) + \frac{1}{2} - \frac{3}{T} + \frac{1}{T^3} \right) + \frac{3}{8} - \frac{5}{3T} + \frac{3}{T^2} - \frac{3}{T^3} \Bigg) \Bigg].
\end{aligned} \tag{A.15}
$$

Here, $T = R_0/S$. The integral of the whole Overhauser element could then be obtained by superposing the integrals above weighted by the values in (2.15, 2.16 and 2.17).

Appendix B

Force Integrals Evaluations

We evaluate the integrals needed for the forces in (2.19) and (2.20). From (2.19) for $p = 1, 2, 4, 5, 6$:

$$\mu_{kp} + i\lambda_{kp} = \frac{1}{Ah} \sum_{n=0}^{\infty} \frac{\sinh(\kappa_n h)}{\kappa_n M_n} \sum_{j=0}^{N} (n_k)_j S_j \times \sum_{q=j-1}^{j+2} [\varphi_n^p]_q \left(b_{m1} + \frac{1}{2} b_{m2} + \frac{1}{3} b_{m3} + \frac{1}{4} b_{m4} \right), (k = 1, 2), \tag{B.1}$$

$$\mu_{kp} + i\lambda_{kp} = \frac{1}{Ah} \sum_{n=0}^{\infty} \frac{\kappa_n h \sinh(\kappa_n h) - \cosh(\kappa_n h) + 1}{\kappa_n^2 M_n} \sum_{j=0}^{N} (n_{k-3})_j S_j \times \sum_{q=j-1}^{j+2} [\varphi_n^p]_q \left(b_{m1} + \frac{1}{2} b_{m2} + \frac{1}{3} b_{m3} + \frac{1}{4} b_{m4} \right), (k = 4, 5), \tag{B.2}$$

$$\mu_{kp} + i\lambda_{kp} = \frac{1}{Ah} \sum_{n=0}^{\infty} \frac{\sinh(\kappa_n h)}{\kappa_n M_n} \sum_{j=0}^{N} S_j \times \sum_{q=j-1}^{j+2} [\varphi_n^p]_q \left[(z_j n_1 - x_j n_2) \left(\frac{1}{2} b_{m1} + \frac{1}{6} b_{m2} + \frac{1}{12} b_{m3} + \frac{1}{20} b_{m4}) \right) + (z_{j+1} n_1 - x_{j+1} n_2) \left(\frac{1}{2} b_{m1} + \frac{1}{3} b_{m2} + \frac{1}{4} b_{m3} + \frac{1}{5} b_{m4}) \right) \right] . (k = 6). \tag{B.3}$$

Again, it is understood that for a panel on the left edge of the shell, $q \in [j, j+2]$ and for one on the right edge, $q \in [j-1, j+1]$. $(n_k)_j$ is the normal component of the panel j in direction k. We also used $m = q - j + 2$ so that $m \in [1, 4]$. Again m should be modified at the outermost panels to $m = q - j + 1$ and $m = q - j + 3$ for the left and right panels respectively. The points x_j and z_j are the starting points of panel j.

From (2.20):

$$f_k = \frac{i\sqrt{\nu}}{A}\frac{\sinh(\kappa_0 h)}{\kappa_0 M_0}\sum_{j=0}^{N}(n_k)_j S_j$$
$$\times \sum_{q=j-1}^{j+2}[\varphi_0^7]_q\left(b_{m1}+\frac{1}{2}b_{m2}+\frac{1}{3}b_{m3}+\frac{1}{4}b_{m4}\right),(k=1,2), \tag{B.4}$$

$$f_k = \frac{i\sqrt{\nu}}{A}\frac{\kappa_0 h\sinh(\kappa_0 h)-\cosh(\kappa_0 h)+1}{\kappa_0^2 M_0}\sum_{j=0}^{N}(n_{k-3})_j S_j$$
$$\times \sum_{q=j-1}^{j+2}[\varphi_0^7]_q\left(b_{m1}+\frac{1}{2}b_{m2}+\frac{1}{3}b_{m3}+\frac{1}{4}b_{m4}\right),(k=4,5), \tag{B.5}$$

$$f_k = \frac{i\sqrt{\nu}}{A}\frac{\sinh(\kappa_0 h)}{\kappa_0 M_0}\sum_{j=0}^{N}S_j$$
$$\times \sum_{q=j-1}^{j+2}[\varphi_0^7]_q\left[(z_j n_1 - x_j n_2)\left(\frac{1}{2}b_{m1}+\frac{1}{6}b_{m2}+\frac{1}{12}b_{m3}+\frac{1}{20}b_{m4}\right)\right.$$
$$\left.+(z_{j+1}n_1 - x_{j+1}n_2)\left(\frac{1}{2}b_{m1}+\frac{1}{3}b_{m2}+\frac{1}{4}b_{m3}+\frac{1}{5}b_{m4}\right)\right].(k=6). \tag{B.6}$$

The interval for q at the edges is the same as that used in treating the radiation coefficients.

Appendix C

Analytical Evaluation of the Source Integrals over a Right Triangle

While Gaussian quadrature is used in general to evaluate the integrals in equations 4.18 and 4.19, analytic integration is required for 4.18 when the collocation point lies within the panel of integration. The integral in 4.19 is exactly zero in that case as well as when the collocation point lies within the same plane as the integration panel. In that case, integration is carried over in the plane of the integration panel (a two dimensional integral). Now, the panel shape is triangular and any triangle can be divided into two right triangles separated by one of the vertex heights. It is therefore necessary to only derive analytic solutions for integration over a right triangle. The value of the integrals will also remain unchanged if we perform the integration over a system whose origin is placed at the point of right angle of the triangle and whose axes are along its two right sides (see figure C.1).

In that case, the required integral is of the form:

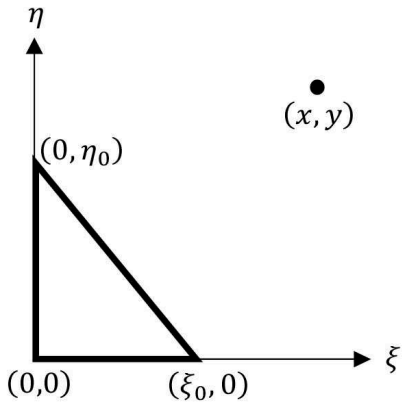

Figure C.1: Schematic diagram of a triangular element

$$
\begin{aligned}
I &= \int_0^{\xi_0} \int_{\delta(\xi-\xi_0)}^{0} \frac{1}{\sqrt{(\xi-x)^2+(\eta-y)^2}} d\eta d\xi \\
&= -y \sinh^{-1}\left(\frac{x}{|y|}\right) - x \sinh^{-1}\left(\frac{y}{|x|}\right) - y \sinh^{-1}\left(\frac{\xi_0 - x}{|y|}\right) + x \sinh^{-1}\left(\frac{\delta\xi_0 + y}{|x|}\right) \\
&+ \frac{\delta(\xi_0 - x) + y}{\sqrt{\delta^2+1}} \sinh^{-1}\left(\frac{-\delta y + (\xi_0 - x)}{|y + \delta(\xi_0 - x)|}\right) + \frac{\delta(\xi_0 - x) + y}{\sqrt{\delta^2+1}} \sinh^{-1}\left(\frac{\delta(\delta\xi_0 + y) + x}{|y + \delta(\xi_0 - x)|}\right),
\end{aligned} \tag{C.1}
$$

and $\delta = -\eta_0/\xi_0$ where ξ_0 and η_0 are defined in figure C.1. There are some special cases to consider. When $y = 0$:

$$
I = x \sinh^{-1}\left(\frac{\delta\xi_0}{|x|}\right) + \frac{\delta|\xi_0 - x|}{\sqrt{\delta^2+1}} \sinh^{-1}\left(\frac{1}{|\delta|}\right) + \frac{\delta(\xi_0 - x)}{\sqrt{\delta^2+1}} \sinh^{-1}\left(\frac{\delta^2\xi_0 + x}{|\delta(\xi_0 - x)|}\right). \tag{C.2}
$$

When $x = 0$:

$$
\begin{aligned}
I = -y \sinh^{-1}\left(\frac{\xi_0 - x}{|y|}\right) + \frac{\delta\xi_0 + y}{\sqrt{\delta^2+1}} \sinh^{-1}\left(\frac{-\delta y + \xi_0}{|y + \delta\xi_0|}\right) \\
+ \frac{\delta\xi_0 + y}{\sqrt{\delta^2+1}} \sinh^{-1}\left(\frac{\delta(\delta\xi_0 + y)}{|y + \delta\xi_0)|}\right).
\end{aligned} \tag{C.3}
$$

When $y + \delta(\xi_0 - x) = 0$:

$$
\begin{aligned}
I = -y \sinh^{-1}\left(\frac{x}{|y|}\right) - x \sinh^{-1}\left(\frac{y}{|x|}\right) \\
- y \sinh^{-1}\left(\frac{\xi_0 - x}{|y|}\right) + x \sinh^{-1}\left(\frac{\delta\xi_0 + y}{|x|}\right).
\end{aligned} \tag{C.4}
$$

Note that these special cases are not required when the collocation point is on the integration panel.

Appendix D

Details for Evaluating the Outer Domain Infuence Coefficients Using the Fourier Expansion of the Rankine Source

In the work in [61], the Rankine source in 4.20 is expanded into a Fourier series:

$$\frac{1}{R_{PQ}} = \frac{1}{2\pi}\varrho^0 + \frac{1}{\pi}\sum_{n=1}^{\infty}\varrho^n \cos(\theta - \psi), \tag{D.1}$$

$$\varrho^n = \frac{2}{\sqrt{rr_0}} Q_{n-\frac{1}{2}}\left(\frac{r^2 + r_0^2 + (z-\zeta)^2}{2rr_0}\right), \tag{D.2}$$

where Q_n is the Legendre function of the second kind and order n while (r, θ, z) and (r_0, ψ, ζ) are the cylindrical coordinates of the points P and Q respectively. This expansion is then used to perform the integration over ψ in 4.20 directly so that:

$$\begin{bmatrix} F_{pmn} \\ G_{pmn} \end{bmatrix} = P_{pmn} \begin{bmatrix} \cos(n\theta) \\ \sin(n\theta) \end{bmatrix} \tag{D.3}$$

$$P_{pmn} = \int_{-h}^{0} \left[\frac{\partial \varrho^n}{\partial n} - \frac{K_m H_n'(K_m r_0)}{H_n(K_m r_0)}\varrho^n\right] \times \frac{\cosh(K_m(\zeta + h))}{\cosh(K_m h)} r_0 d\zeta + 2\pi \frac{\cosh(K_m(z+h))}{\cosh(K_m h)}\delta_p. \tag{D.4}$$

In this final expression, the integral is evaluated numerically except in the region $\zeta \in [z - \Delta, z + \Delta]$ for some small enough Δ. In that region, the expansions:

$$\varrho^n = \frac{2}{r_0}\log\left(\frac{2r_0}{|z-\zeta|}\right) + \varrho^{n(R)}, \tag{D.5}$$

$$\frac{\partial \varrho^n}{\partial n} = -\frac{1}{r_0^2}\log\left(\frac{2r_0}{|z-\zeta|}\right) + \frac{\partial \varrho^{n(R)}}{\partial n}, \tag{D.6}$$

are used. Here $\varrho^{n(R)}$ and $\frac{\partial \varrho^{n(R)}}{\partial n}$ are the remainders left after extracting the singular parts. The integral over these remainders is carried over numerically as well while the integral over the singular parts is given by:

$$P_{pmn}^{(S)} = -\left(\frac{1}{r_0} + 2\frac{K_m H_n'(K_m r_0)}{H_n(K_m r_0)}\right) S_m(\Delta)\frac{\cosh(K_m(z+h))}{\cosh(K_m h)}, \tag{D.7}$$

where S_m is defined as:

$$S_m(\Delta) = \frac{2}{K_m}\left(\mathrm{Shi}(K_m\Delta) - \sinh(K_m\Delta)\log\left(\frac{\Delta}{2r_0}\right)\right), \tag{D.8}$$

and Shi is the hyperbolic sine integral function [77].

Appendix E

Integration of the Chebychev Type Potential With a Hypersingular Kernel

The equation to solve here is that in (3.13):

$$4\pi \int_S \frac{\partial \phi_i}{\partial n} F_{mn}(x,y) = -\sum_{p=0,q=0}^{\infty} A_{mn}^i \int_S \int_S \left(F_{mn}(x,y) F_{pq}(\xi,\eta) \frac{1}{R_{PQ}^3} \right) dS_Q dS_P. \tag{E.1}$$

The idea here is to approximate the representation $F_{pq}(\xi,\eta)$ in the first integral using a few terms of its Taylor series (expanded at the center of each triangular element of the mesh) and then using that to perform the first integration in an analytical fashion. This requires the derivatives of Chebychev polynomials which are readily available in closed form. The integration is then simplified to finding analytical forms for the integrals of low order monomials multiplied by the hypersingular kernel which is much more weildy than the original form. The second integral can be performed using Gaussian quadrature over triangular elements.

To start with, we use the ideas of appendix C to simplify the problem to an integration over a right triangle in the system whose axes are along the right sides of that triangle (figure C.1). This is a shifted and rotated system. In that case, the required integrals will be of the form:

$$I_{mn} = \int_0^{\xi_0} \int_{\delta(\xi-\xi_0)}^0 \frac{\xi^m \eta^n}{\left((\xi-x)^2 + (\eta-y)^2\right)^{3/2}} d\eta d\xi. \tag{E.2}$$

These integrals can then be grouped together in the Taylor series integral to obtain the desired original integral. It is important to point here that the values for ξ and η in these integrals are defined in the new rotated system and can be related to the original variable using the transformations:

$$\xi^{old} = \cos\theta \xi^{new} - \sin\theta \eta^{new} + X_0, \tag{E.3}$$

$$\eta^{old} = \sin\theta \xi^{new} - \cos\theta \eta^{new} + Y_0, \tag{E.4}$$

where θ is the angle of rotation of the new system and X_0, Y_0 are the shift values in the x and y directions respectively. If x and y are also shifted and rotated, then the denominator of the integral is only a function of the distance between two points and is invariant under translation and rotation. This means that only the numerator needs to be shifted back to the old system. The monomial integrals in the old system (needed for our problem) are a linear combination of the monomial integrals in the new system.

Now getting back to the integral set E.2, we notice that the higher order integrals can

be written in a simpler manner. To do that, it is useful to define the set:

$$J_{mn} = \int_0^{\xi_0} \int_{\delta(\xi-\xi_0)}^{0} \frac{(\xi - x)^m (\eta - y)^n}{\left((\xi - x)^2 + (\eta - y)^2\right)^{3/2}} d\eta d\xi. \tag{E.5}$$

These integrals are slightly easier to evaluate. Accordingly, we can write:

$$I_{00} = J_{00}, \tag{E.6}$$
$$I_{10} = J_{10} + xI_{00}, \tag{E.7}$$
$$I_{01} = J_{01} + yI_{00}, \tag{E.8}$$
$$I_{11} = J_{11} + xI_{01} + yI_{10} - xyI_{00}, \tag{E.9}$$
$$I_{20} = J_{20} + 2xI_{10} - x^2 I_{00}, \tag{E.10}$$
$$I_{02} = J_{02} + 2yI_{01} - y^2 I_{00}, \tag{E.11}$$

and so forth. Therefore, it is only necessary to evaluate the integrals J_{mn}. Those could be obtained using any symbolic computation package and are not shown here for brevity. Note that we noticed that going to higher order is worth the effort.